

DISS. ETH No. 15990

# **Towards Monolithic CMOS Cell-based Biosensors**

A dissertation submitted to the  
SWISS FEDERAL INSTITUTE OF TECHNOLOGY ZURICH  
for the degree of  
DOCTOR OF NATURAL SCIENCES  
presented by

Wendy A. Franks  
M. Sc., University of Waterloo  
Born September 4<sup>th</sup>, 1974  
Citizen of Canada

accepted on the recommendation of

Prof. Dr. A. Hierlemann, examiner  
Prof. Dr. M. Textor, co-examiner  
Prof. Dr. H. Baltes, co-examiner

2005

Copyright © 2004 by Wendy Franks, Physical Electronics Laboratory

All rights reserved. No parts of this book may be reproduced, stored in a retrieval system, or transmitted, in any form or by any means, electronic, mechanical, photocopying, recording or otherwise, without prior written permission of the copyright holder.

**Franks, Wendy A.:**

Towards Monolithic CMOS Cell-based Biosensors

Published by:

*Physical Electronics Laboratory, PEL*

Swiss Federal Institute of Technology (ETH) Zürich

ETH-Hönggerberg, HPT

CH-8093 Zürich

Switzerland

---

# TABLE OF CONTENTS

<b>ABSTRACT</b>	<b>1</b>
<b>ZUSAMMENFASSUNG</b>	<b>3</b>
<b>1 INTRODUCTION</b>	<b>5</b>
1.1 Applications	5
1.2 Scope of This Thesis	8
1.3 Summary of Major Results	9
1.4 References	11
<b>2 THEORY OF CELL-BASED BIOSENSORS</b>	<b>13</b>
2.1 Extracellular Recording Principle	14
2.1.1 Action Potential Biophysics	14
2.1.2 Extracellularly Recorded Field Potentials	23
2.1.3 Field Potential Waveform Analysis	25
2.1.4 Interface Impedance	28
2.2 Cell Adhesion	29
2.3 Summary	33
2.4 References	34
<b>3 EXPERIMENTAL METHODS</b>	<b>37</b>
3.1 CMOS Post-Processing	38
3.1.1 Electrode Material	38
3.1.2 Shifted Electrode Design	42
3.1.3 Stability Under Culturing Conditions	43
3.2 Packaging	45
3.3 Impedance Measurements	47
3.4 Cardiomyocyte Cell Culturing	52
3.5 Summary and Conclusions	53
3.6 References	54
<b>4 PATTERNED CELL ADHESION</b>	<b>57</b>
4.1 Patterned Cell Adhesion	58
4.1.1 Review of Controlled Cell Adhesion Strategies	58
4.2 Patterned Cell Adhesion	66
4.2.1 Process Characterization	68
4.2.2 Protein Adhesion	68
4.2.3 Patterned Cardiomyocytes	71

---

4.2.4 Patterned Neural Networks	73
4.3 Summary and conclusions	75
4.4 References	76
<b>5 ELECTROPHYSIOLOGICAL RECORDINGS</b>	<b>81</b>
5.1 Recording System	83
5.1.1 CMOS Chip	85
5.1.2 Platinization	86
5.2 Electrophysiological Recordings with 1st Generation CMOS Chip	87
5.3 Electrophysiological Recordings with 2nd Generation CMOS Chip	88
5.3.1 Cardiomyocyte Recordings	88
5.3.2 Neural Recordings	90
5.4 Summary and Conclusions	92
5.5 References	93
<b>6 CONCLUSIONS AND OUTLOOK</b>	<b>95</b>
6.1 Conclusions	95
6.1.1 The CMOS Advantage	95
6.1.2 In vitro versus in vivo	96
6.2 Outlook	96
6.2.1 Commercial Potential	97
<b>APPENDIX A</b>	<b>99</b>
Impedance Characterization and Modeling of Electrodes for Biomedical Applications	
<b>APPENDIX B</b>	<b>109</b>
CMOS microelectrode array for the monitoring of electrogenic cells	
<b>APPENDIX C</b>	<b>119</b>
Self- Assembled Structures for Patterned Cell Adhesion on a CMOS Cell-Based Biosensor	
<b>APPENDIX D</b>	<b>121</b>
Hippocampal Neuron Preparation and Culture Protocol	
<b>APPENDIX E</b>	<b>123</b>
Staining Protocol	
<b>PUBLICATION LIST</b>	<b>125</b>
<b>CURRICULUM VITAE</b>	<b>127</b>

---

# ABSTRACT

This thesis reports on the design, characterization and integration of a cell-based biosensor system. At the heart of the system is a CMOS chip capable of stimulating and recording activity from electrogenic cells, such as heart muscle cells and neurons. The CMOS chip comprises an array of metal microelectrodes, as well as analog and digital circuitry. Cells are cultured on top of the CMOS-chip in direct contact with the array. The chip is packaged to protect the electrical connections from the liquid cell-culture environment and to form the cell-culture bath. This system finds a multitude of applications in not only chemical- and biological-toxin biosensing, but also in the fields of cardiology, drug development/pharmacology, and neuroscience.

Signal transduction is based upon an array of metal microelectrodes. Critical to the transducer design is a low electrode-electrolyte impedance. A model describing the physical processes contributing to the electrode-electrolyte interface impedance has been validated. This model was extended to: (1) quantify the effect of adhesion mediators typically used in such a system; (2) quantify the effect of incubation time; and (3) to evaluate a new nanostructured gold electrode material.

Post-processing is required for biocompatibility and chip stability. The electrodes of the CMOS chip, as received from the foundry, are aluminum, a neurotoxicant that easily corrodes in the presence of the electrolytic culture medium. A shifted-electrode design was therefore used to define the material, size and shape of the transducing electrodes, and to protect the underlying aluminum. Using this configuration, the chip circuitry was found to be stable for 200 days in vitro (DIV). Where necessary, the dendritically structured black platinum was electrochemically deposited on the bright platinum transducers to reduce the electrode impedance.

As an extension to the system, a technique for patterned cell adhesion, based on the selective molecular assembly patterning (SMAP) process was developed. In comparison to other patterning techniques, the SMAP process has several advantages: it is self-aligning according to the chip's heterogeneous surface composition, it is based on a simple dip-and-rinse process and it results in high-contrast

---

cell adhesion. Cell cultures of neonatal rat cardiomyocytes (NRC) and neural/glia cells were guided for up to 5 and 21 DIV respectively, at which point the experiments were terminated. Immunofluorescence staining of the NRCs showed that the engineered surfaces did not disrupt myofibrillogenesis, the formation of the muscle microstructure.

Finally, electrophysiological recordings were performed with organ (heart) and cell (cardiomyocyte and neural) cultures. Recordings from neonatal rat cardiomyocytes at 5 DIV had an amplitude of 1.8 mV and a duration of approximately 2.5 ms. Recordings from chicken neurons, made at 56 DIV, had an amplitude of 0.5 - 0.6 mV and a spike duration of 3 - 4 ms. This demonstrates system's biocompatibility and its ability to withstand the harsh culture environment.

---

# ZUSAMMENFASSUNG

Die vorliegende Dissertation befasst sich mit der Entwicklung, Charakterisierung und Integration von zellbasierten Biosensorsystemen. Das Herzstück des Systems ist ein CMOS-Chip, der elektrogene Zellen wie z.B. Herzmuskelzellen und Neuronen stimuliert und ihre Aktivität aufzeichnet. Der CMOS-Chip besteht aus einer Anordnung von mehreren, nahe beieinander liegenden Metallmikroelektroden so wie analogen und digitalen Schaltungskomponenten. Die Zellen werden auf dem CMOS-Chip im direkten Kontakt mit den Elektroden kultiviert. Der Chip wird verkapselt, um einerseits die elektrischen Verbindungen vor der flüssigen Nährlösung zu schützen und andererseits ein Bad für die Zellkultur zur Verfügung zu stellen. Das System hat ein breites Anwendungsfeld nicht nur für chemisch-, biologisch-toxikologische Biosensormessungen, sondern auch im Bereich der Kardiologie, Medikamentenentwicklung/Pharmakologie und Neurowissenschaften.

Die elektrischen Signale der Zellen werden durch Metallelektroden aufgenommen, wobei unter Berücksichtigung, dass der Kontakt zwischen den Elektroden und der Elektrolytlösung eine möglichst niedrige Impedanz aufweist. Diese Impedanz ist kritisch für die Transducer-Ausführung. Ein Modell, welches die physikalischen Prozesse der Grenzflächenimpedanz beschreibt wurde aufgestellt und mit durchgeführten Messungen verglichen. Dieses Modell wurde erweitert auf: (1) eine quantitative Beschreibung des Einflusses von Adhäsionsvermittlern wie sie typischerweise in solchen Systemen benutzt werden, (2) eine quantitative Beschreibung des Einflusses der Inkubationszeit, und (3) die Einwirkung eines neuen, nanostrukturierten Goldelektroden-Materials.

Die Nachprozessierung der CMOS-Chips ist notwendig, um Biokompatibilität und Stabilität des Chips zu gewährleisten. Die ursprünglichen CMOS-Elektroden bestanden aus Aluminium und sind somit für die direkte Anwendung ungeeignet. Aluminium korodiert schnell in der Elektrolytlösung und wirkt ausserdem neurotoxisch. Deshalb wurde eine Prozess entwickelt, der es ermöglicht, auf die CMOS-Elektroden neue Elektroden aufzubringen und deren Material, Form und Grösse zu variieren. Durch das Prinzip des versetzten Aufbringens dieser Elektroden ('shifted-electrode design') wird zudem die darunterliegende Aluminium Elektrode geschützt. In dieser Konfiguration funktionierten die integrierten

---

Schaltkreise noch nach 200 Tagen in vitro (DIV). Wenn nötig, wurde mittels elektrochemisch abgeschiedenem, dendritischem, schwarzem Platin die Grenzflächenimpedanz der Elektroden verringert.

Zur Erweiterung des Systems wurde eine Technik zur strukturierten Zelladhäsion basierend auf dem "selective molecular assembly patterning" (SMAP) Prozess entwickelt. Im Vergleich zu anderen, aufwendigeren Strukturierungstechniken hat der SMAP Prozess mehrere Vorteile: Er ist ein selbstausrichtender Prozess und basiert auf einem einfachen "Eintauch-und-Abspül" Prozess. Mit dieser Methode wurde eine gute Strukturierung des Zellwachstums von neonatalen Ratten-Kardiomyozyten (NRC) und Neural/Glia Zellen auf der Chipoberfläche über einen Zeitraum von mehr als 5, bzw. 21, Tagen in vitro erreicht. Immunofluoreszenz der NCR zeigte, dass die Oberflächenbehandlung nicht die Myofibrillogenese (Formation der Muskelmikrostrukturen) stört.

Abschließend wurden elektrophysiologische Aufnahmen von Organ- (Herz) und Zellkulturen (Kardiomyozyten) durchgeführt. Die Messungen der elektronischen Signale an neonatalen Ratten-Kardiomyozyten am fünften Tag in vitro zeigten eine Amplitude von 1.8 mV und eine Dauer von circa 3 bis 4 ms. Dies demonstriert, dass dieses zellbasierte Biosensorsystem biokompatibel ist und den harten Bedingungen der Zellkultivierung standhält.



# 1 INTRODUCTION

Biosensing implies the use of a biological entity to gain insight into the environment around us. Arguably the best known example is the canary in the coal mine that would warn miners of dangerous methane leaks. In more recent times, animals continue to be used as sentinel species. In the 1995 police raid of the Aum Shinrikyo compound, canaries were used to detect sarin, a lethal nerve gas agent [Stenger *et al.*, 2001]. Fish have been used to monitor water quality [van der Schalie *et al.*, 1999], and scientists often point to changes in organism populations as indicators of global environmental changes. For example, declining amphibian populations is potentially linked to a thinned ozone layer [Blaustein and Belden, 2003]. In a sense, a biosensor harnesses the exquisitely designed sensitivities of biological entities to environmental factors that have resulted from millions of years of evolutionary biological engineering.

In a cell-based biosensor (CBB), a cell rather than an entire organism is used as the sensing element. This involves the combination of two transducers: the cell, as the primary transducer, and a secondary transducer that converts cellular activity (or response) into a signal conducive to processing. An array of microelectrodes<sup>1</sup>, referred to as a microelectrode array (MEA), is most commonly used as the secondary transducer. In one manifestation, the beating of a heart cell is converted into an electrical signal by an underlying microelectrode. CBBs exhibit two intriguing characteristics: Firstly, the biological entity has a naturally evolved analyte selectivity, and secondly, they respond in a physiologically relevant way [Pancrazio *et al.*, 1999].

## 1.1 APPLICATIONS

This type of system finds a myriad of applications in both applied and pure science. In applied science, it is a promising tool for the detection of chemical and biological toxins. No prior knowledge of the investigated compound is required,

---

1. Microelectrode means that the electrode size is in the range of tens of micrometers, typically circular with a 30- $\mu\text{m}$  diameter.

as is the case for sensors dependent on antibody binding, and CBB's provide a net physiological response to a mixture of compounds.

For these very reasons, CBB's are emerging as a useful tool in pharmaceutical research. In recent years, increasing attention has been paid to the pharmacological effect of drugs on the QT-interval prolongation, the time interval on the electrocardiogram (EKG) representative of ventricular repolarization. A prolongation of the QT interval may lead to *torsade de pointes*, a condition of rapid, arrhythmic heart beating that is potentially fatal. Many agents that lengthen the QT interval are known to delay cell repolarization through the inhibition of the rapidly activating delayed rectifier potassium current ( $I_{kr}$ ) [Redfern *et al.*, 2003]. This is a transmembrane ion-channel current, controlled by the hERG potassium ion channel (known as the human ether-à-go-go-related, gene-encoded, voltage-dependent potassium channel, in parlance of biologists).

In 2002 the American Food and Drug Administration (FDA) issued a document for QT interval safety pharmacology (ICH S7B). In this document the guidelines for nonclinical assessment of potential hazard and risk of QT-interval prolongation are given. Such an assessment is required of all new drug candidates submitted to the FDA. The gold standard for assessing the pharmacological effect on  $I_{kr}$  is the patch-clamp method. Because this technique is technically complex and time-consuming, it is not cost effective to test the effect on the hERG channel until late in the pre-clinical stage of drug development. By this stage, a considerable amount of resources has been invested in each drug candidate.

A disruptive technology, enabling fast, accurate, high-volume analysis capabilities of the pharmacological effect of a candidate drug on the hERG channel would be a very useful tool for the pharmaceutical industry. A potential solution would be to use an MEA. Indeed, Multichannel Systems GmbH, Germany, launched its QT-Screen product for cardiac electrophysiological drug profiling in the fall of 2004. QT-Screen is based on a 96-well plate, each well having two microelectrodes for extracellular electrophysiology measurements.

Although an MEA does not provide quantitative information about individual ion-channel currents, it does provide a physiologically relevant, net cellular response to a given compound. Automated patch-clamp systems<sup>1</sup> for drug testing are centered around genetically mutated cells that over-express the gene for one

---

1. High-throughput systems are available for ion-channel screening from Molecular Devices Inc., Australia – IonWorks Quatro, IonWorks HT and PatchXpress 7000.

type of ion channel, such as the hERG potassium channel. Testing one type of ion channel may not give complete information of potential QT-interval prolongation because interactions with many cardiac ion channels may mitigate or exacerbate prolongation leading to false positives and false negatives. In short, the MEA has the potential to yield richer information, because the whole-cell response is more representative of the *in vivo* situation than the ion channel current for a single channel type.

A second application field is found in neuroscience. In this case, the device is not used as a biosensor *per se*, but rather as a platform to study network theory. It is believed that a better understanding of neural networks will help elucidate the mysteries of learning and memory. However, it is well documented that neural networks behave much differently *in vitro* as opposed to *in vivo* [Holt *et al.*, 1996]. *In vitro* studies usually involve the competing patch clamp technology capable of providing high-resolution information about neural activity. What, then, is the merit of *in vitro* analysis based on extracellular recordings? The short answer is it's the best scheme currently available, yet more work is required to determine exactly what can be learned about the brain from *in vitro* experimentation. Notwithstanding this ambiguity, a compelling argument can be made for *in vitro* recordings with an MEA. Consider first that *in vivo* experiments are technically complex — it is difficult to safely access the brain. Moreover, intracellular *in vivo* recordings are challenging because the pulsating movement inside the brain disrupts electrode micropositioning. Indeed, the greatest advances in understanding neural activity, Hodgkin and Huxley's experiments in the early 1950's [Hodgkin and Huxley, 1952], are based on *in vitro* experimentation. However, these experiments were performed using the intracellular voltage clamp<sup>1</sup> technique. In contrast to patch clamp experimentation, MEA's facilitate long-term, high spatiotemporal-resolution information, while patch clamping is limited to a few measurement points for a relatively short period of time. Increasingly, research groups are using the MEA systems to probe information processing and storage [Marom and Shahaf, 2002, Beggs and Plenz, 2004]. A strong argument can be made for the use of the MEA in computational neuroscience since it is not prerequisite that the neural cultures retain their *in vivo* network dynamics. In this case, what is required is high spatiotemporal interfacing [Ruaro *et al.*, 2005].

- 
1. The patch-clamp technique is a refinement of the voltage-clamp technique originally developed by Kenneth Cole in 1949 and used by Hodgkin and Huxley in the 1950's. Patch-clamping allows properties of individual ion channels to be analyzed, although whole-cell patch-clamping, similar to voltage-clamping, is also used.

The MEA used in this thesis is unique in that it comprises both the array of microelectrodes and on-chip circuitry for signal processing and conditioning on a single chip. The circuitry was realized using standard complementary-metal-oxide-semiconductor (CMOS) technology. The general advantage of CMOS technology is that it is a standard industrial process; in theory designs can be sent to any foundry for manufacturing. Furthermore, on-chip circuitry leads to simplified system design and higher resolution signals. To complete the biosensor, an electrically active cell, such as a neuron or heart muscle cell, is used as the biological transducing element.

### **1.2 SCOPE OF THIS THESIS**

The objective of this thesis is to contribute to the development of CMOS cell-based biosensor systems. This work can be classified as bioelectronics or bioelectronic system design. The term ‘system design’ is used to reflect the many different components drawn together to form a functioning, well-defined CMOS cell-based biosensor: starting with the characterization of the electrode-electrolyte interface; to the CMOS post-processing required to prepare the chip for cell culturing; to the development of a patterned surface to selectively engineer sites of cell adhesion and analysis of the cellular microstructure; to the electrophysiological recordings from electrogenic cells.

Three journal articles were prepared during the course of this research. Rather than repeating findings and results, the articles are referred to throughout the text and are given in Appendices A, B and C.

An introduction to the theory pertaining to cell-based biosensors is presented in Chapter 2. The chapter is divided into two sections: the extracellular recording principle and the basic theory of cell adhesion. The discussion on the extracellular recording principle includes: a discussion of the neural and cardiac myocyte action potential; the physics of the extracellular recording principle; and a brief section on waveform analysis. The validation of a model based on electrochemical impedance spectroscopy to electrically characterize the electrode-electrolyte interface is presented. Since cell-substrate coupling is a necessary precondition to record electrogenic activity, a section on cell adhesion is presented.

The third chapter covers the experimental methods necessary to realize the device. Post-processing and packaging of the CMOS chip was necessary to pre-

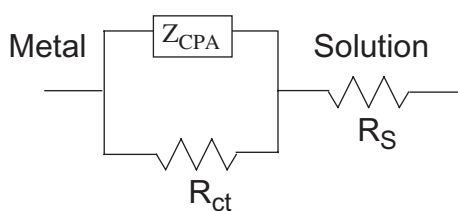
pare the chip for the harsh culture environment. As a new electrode material, a nanostructured gold material was evaluated using the impedance model developed in Chapter 2. Finally, culture preparation for cardiomyocytes is presented.

Chapter 4 is dedicated to the topic of patterned cell adhesion. The first half contains a review of the various strategies used to define the location of cell adhesion, including microcontact stamping, ink-jet printing, photolithographic techniques, microfluidics, physical immobilization and structuring, and selective molecular assembly patterning (SMAP). In the second half, the development of the SMAP processed used in this work is described. This includes the functionalization process, surface characterization, patterning of various proteinaceous and polymeric adhesion mediators, immunofluorescence testing of cell differentiation and pattern validation with various cell types.

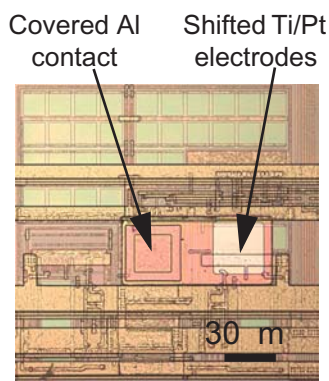
In the final chapter, the recording system architecture, including the CMOS, is presented. The circuitry architecture includes signal conditioning as close to the recording site as possible for potentially improved signal-to-noise ratio, and both stimulation and recording capabilities. Electrophysiological recordings from both organ (heart) and cell (neural and cardiac myocyte) culture demonstrate that the system: a) withstands the harsh culture environment; b) is biocompatible; and c) can be used with various cell and culture types.

## 1.3 SUMMARY OF MAJOR RESULTS

### IMPEDANCE MODEL OF THE ELECTRODE-ELECTROLYTE INTERFACE



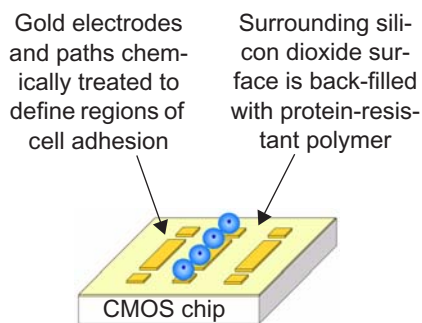
A model of the electrode-electrolyte interface was validated and extended to: (1) quantify the effect of adhesion mediating coatings; (2) quantify the effect of incubation time; and (3) to evaluate new electrode materials. For the most basic system (platinum/physiological saline), the equilibrium exchange current was found to be  $8.5(10)^{-8}$  A/cm<sup>2</sup>, and the charge-transfer resistance 450 k $\Omega$ . The model was used to compare four different materials: platinum black, bright platinum, nanostructured gold and bright gold. Platinum black has the lowest impedance over the relevant frequency range of 10 Hz - 5 kHz. Furthermore, the electrode interface is predominantly capacitive over this measurement frequency range.



Post-processing is required for biocompatibility and chip stability. The electrodes of the CMOS chip, as received from the foundry, are made of aluminum, a neurotoxicant that easily corrodes in the presence of the electrolytic culture medium. A shifted-electrode design was therefore used to define the material and dimensions of the transducing electrodes, and to protect the underlying aluminum. It was found that an alternating stack of  $\text{SiO}_2$  and  $\text{SiN}_3$ , total thickness  $1.6 \mu\text{m}$ , was required to adequately seal the aluminum.

Using this configuration, the chip circuitry was found to be stable for 200 days *in vitro* (DIV).

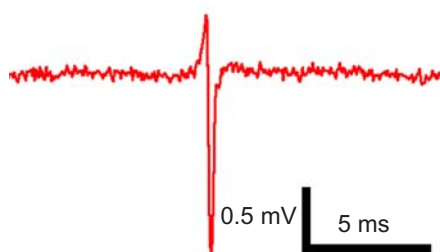
### PATTERNED CELL ADHESION



A strategy for patterned cell adhesion, based on the selective molecular assembly patterning (SMAP) process was developed for the CMOS chip used in this work. The advantages of the SMAP process are: it is self-aligning to the heterogeneous chip surface, it is based on a simple dip-and-rinse process, and it results in high-contrast cell adhesion. Cell cultures of neonatal rat cardiomyocytes (NRC)

and neural/glia cells were guided for up to 5 and 21 DIV, respectively (at which point the experiments were terminated). Immunofluorescence staining of the NRC shows that they develop the appropriate muscle structure, indicating that the engineered surface does not disrupt the formation of this microstructure.

### ELECTROPHYSIOLOGICAL RECORDINGS



Electrophysiological recordings were performed with two generations of the CMOS chip using organ (heart) and cell (cardiac myocyte and neural) cultures. The recorded signals are similar to those reported in literature. This demonstrates the system's biocompatibility and its ability to withstand the harsh culture environment. Furthermore,

measurements with two distinct electrogenic cell types is indicative of the system's flexibility with respect to cell culture, signal range and frequency.

## 1.4 REFERENCES

Beggs, J. M., and Plenz, D. (2004). "Neuronal avalanches are diverse and precise activity patterns that are stable for many hours in cortical slice cultures" *J. Neurosci.*, 24(22), 5216-29.

Blaustein, A. R., and Belden, L. K. (2003). "Amphibian defenses against ultraviolet-B radiation." *Evol. Dev.*, 5(1), 89-97.

Hodgkin, A. L., and Huxley, A. F. (1952). "A quantitative description of membrane current and its application to conduction and excitation in nerve." *J. of Phys.*, 117, 500-544.

Holt, G. R., Softky, W. R., Koch, C., and Douglas, R. J. (1996). "Comparison of discharge variability in vitro and in vivo in cat visual cortex neurons." *J. Neurophysiol.*, 75(5), 1806-14.

Marom, S., and Shahaf, G. (2002). "Development, learning and memory in large random networks of cortical neurons: lessons beyond anatomy." *Quarterly Reviews of Biophysics*, 35(1), 63-87.

Pancrazio, J. J., Whelan, J. P., Borkholder, D. A., Ma, W., and Stenger, D. A. (1999). "Development and application of cell-based biosensors." *Annals of Biomedical Engineering*, 27, 687-711.

Redfern, W. S., Carlsson, L., Davis, A. S., Lynch, W. G., MacKenzie, I., Palethorpe, S., Siegl, P. K., Strang, I., Sullivan, A. T., Wallis, R., Camm, A. J., and Hammond, T. G. (2003). "Relationships between preclinical cardiac electrophysiology, clinical QT interval prolongation and torsade de pointes for a broad range of drugs: evidence for a provisional safety margin in drug development." *Cardiovasc. Res.*, 58(1), 32-45.

Ruaro, M. E., Bonifazi, P., Torre, V. (2005). "Towards the neurocomputer: image processing and pattern recognition with neuronal cultures." *IEEE Transactions on Biomedical Engineering*.

Stenger, D. A., Gross, G. W., Keefer, E. W., Shaffer, K. M., Andreadis, J. D., Ma, W., and Pancrazio, J. J. (2001). "Detection of physiologically active compounds using cell-based biosensors." *Trends in Biotechnology*, 19(8), 304-309.

van der Schalie, W. H., Gardner, H. S., Bantle, J. A., de Rosa, C. T., Finch, R. A., Reif, J. S., Reuter, R. H., Backer, L. C., Burger, J., Folmar, L. C., Stokes, W. S.

(1999). "Animals as sentinels of human health hazards of environmental chemicals." *Environmental Health Perspectives*, 107(4), 309-315.



---

## 2 THEORY OF CELL-BASED BIOSENSORS

The complete theory describing the principles underlying a cell-based biosensor spans many disciplines: from cell biology, to surface and materials science to electrical engineering and signal analysis. For each of these contributing fields the significance and complexity is not to be underestimated, yet a treatise of each is beyond the scope of this work. The focus of this work is the cell-electrode interface with the aim of creating a flexible device useful for either pharmacological applications, or basic and applied neuroscience studies. As such, a treatment of the basic theory of the electrogenic cell and the cell-transducer interface, with an emphasis on the interface impedance and cell adhesion, is presented in this chapter (Fig. 2.1).

This chapter opens with a review of the principles underlying the extracellular recording principle. A description of the relevant biophysical processes occurring in the cardiomyocyte and neuron are introduced. The second section of the chapter deals with the physical biochemistry of cell adhesion as a critical factor affecting patterned cell adhesion and proper functioning of the cell.

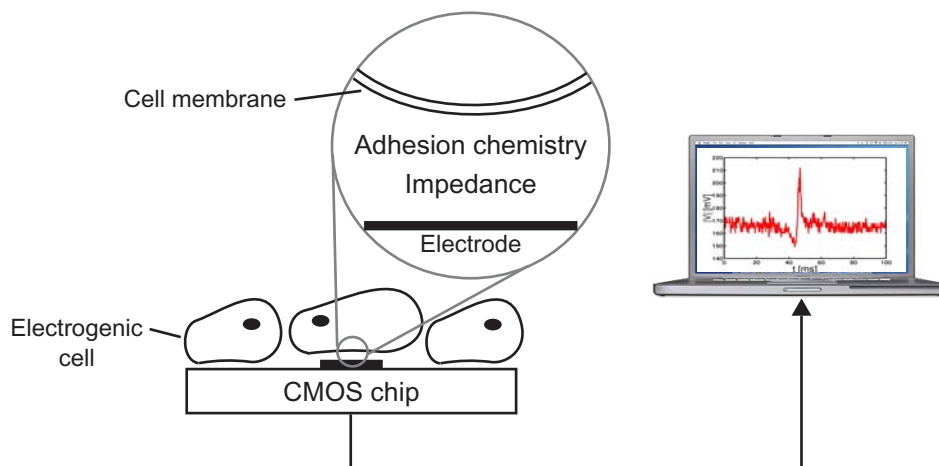


*Fig. 2.1: The focus of this work is the cell-electrode interface, with special attention paid to the interface impedance and patterned cell adhesion.*

### 2.1 EXTRACELLULAR RECORDING PRINCIPLE

Critical to identifying the value and application breadth of a cell-based biosensor is the answer to the following question: *What is measured when activity from an electrogenic cell is recorded extracellularly?* In comparison to intracellularly recorded signals, which yield quantitative values for specific ion-channel currents [Alberts *et al.*, 1994], it is not yet clear how much information can be derived from extracellularly recorded signals. Indeed, this is the focus of many research groups. Studies involving simultaneous patch clamp and extracellular recordings [Ingebrandt *et al.*, 2004] significantly contribute to our understanding of *what* is being recorded. Similarly, pharmacological experiments demonstrating the effect of blocking specific ion channels on the shape of the extracellular waveform [Halbach *et al.*, 2003], open the field to more diverse applications. In this section, the mechanisms involved in such a recording, from the origin of the action potential to the extracellularly recorded waveform, as understood at this juncture, are described.

#### 2.1.1 ACTION POTENTIAL BIOPHYSICS

The biophysical processes occurring when an action potential event occurs are complex, involving the interplay of many unique ion channels and ion exchangers (for example, see Fig. 2.2). An attempt to explain these processes for the case of dissociated cultures of cardiac myocytes and neurons is presented. A detailed discussion of the cardiac myocyte excitation-contraction mechanism follows, while only a brief account of the neural action potential, with an equivalent circuit model, is presented. The biophysics of the neuron action potential is extensively covered in literature [see, for example, Kandel *et al.*, 2000].

In general, an action potential event is largely the result of voltage-gated ion-channel conductances that cause a depolarization and repolarization of the plasma membrane. The resting potential across the membrane is maintained by large transmembrane proteins that pump ions, against their electrochemical gradient, in and out of the cell. Driving this pumping action is energy that is stored in the phosphate bonds of adenosine triphosphate (ATP). The event itself is triggered when the membrane is depolarized to a threshold value causing voltage-gated ion channels to open. Ions flow down their electrochemical gradient across the cell membrane, further depolarizing the membrane. Depolarization causes other ion channels to open, causing a current flow in the opposite direction

that repolarizes the membrane. Finally, exchange pumps generate a current that returns the membrane to its resting potential. Note that, the convention in electrophysiology is that the movement of negative species into the cell is defined as a positive current.

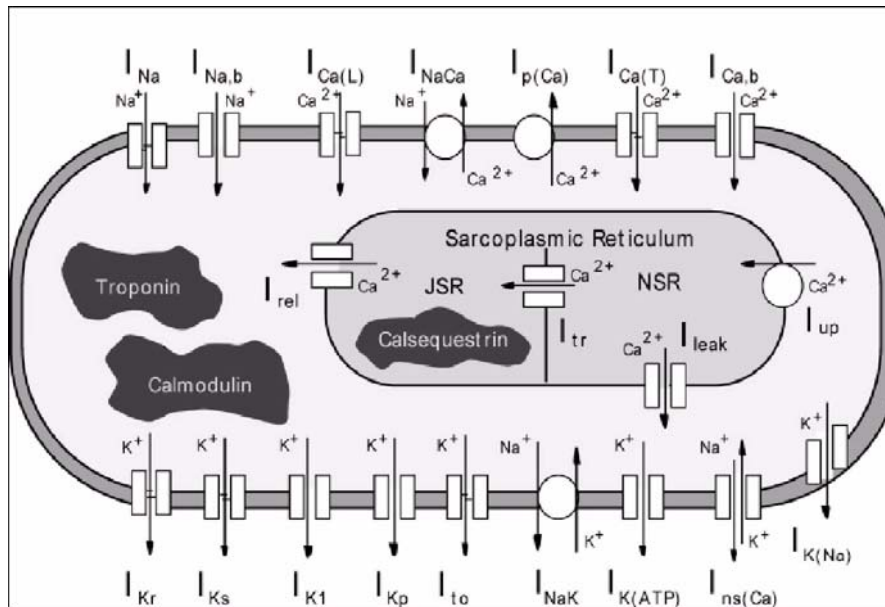


Fig. 2.2: Schematic of the ventricular cardiac myocyte showing the many electrophysiological components that contribute to the action potential (reproduced with author's permission, Kléber and Rudy, 2004). See Tab. 2.1 for descriptions of the variables and terms used.

Tab. 2.1: Description of variables used in Figs.2.2 and 2.4.

Variable	Description
$I_{Na}$	fast sodium current
$I_{Ca(L)}$	calcium current through L-type calcium channels
$I_{Ca(T)}$	calcium current through T-type calcium channels
$I_{Kr}$	rapid delayed rectifier potassium current
$I_{Ks}$	slow delayed rectifier potassium current
$I_{to}$	transient potassium outward current
$I_{K1}$	inward rectifier potassium current
$I_{K(ATP)}$	ATP-sensitive potassium current

*Tab. 2.1: Description of variables used in Figs.2.2 and 2.4.*

<b>Variable</b>	<b>Description</b>
$I_{Kp}$	plateau potassium current
$I_{K(Na)}$	sodium-activated potassium current
$I_{ns(Ca)}$	nonspecific calcium-background current
$I_{NaK}$	sodium-potassium pump current
$I_{NaCa}$	sodium-calcium exchange current
$I_{P(Ca)}$	sarcolemmal calcium pump
$I_{up}$	calcium uptake from the myoplasm <sup>a</sup> to the network sarcoplasmic reticulum (NSR)
$I_{rel}$	calcium release from junctional sarcoplasmic reticulum (JSR)
$I_{leak}$	calcium leakage from NSR to the myoplasm
$I_{tr}$	calcium translocation from NSR to JSR
<b>Calmodulin</b>	calcium buffer in myoplasm
<b>Troponin</b>	calcium buffer in myoplasm
<b>Calsequestrin</b>	calcium buffer in the JSR

a. The myoplasm refers to the contractile portion of the muscle cell.

## CARDIOMYOCYTE ACTION POTENTIAL

As mentioned above, the cardiomyocyte action potential is initiated when the membrane potential,  $V_m$ , reaches a threshold, triggering the opening of sodium ion channels and a rapid depolarization of the membrane potential (phase 0, Fig. 2.3). Within 1 ms, the inward flowing  $I_{Na}$  reaches its maximum and inactivates (phase 1, Fig. 2.3, and Fig. 2.4). Membrane depolarization opens the calcium ion channels when  $V_m$  reaches  $\sim -25$  mV, initiating the inward L-type  $Ca^{2+}$  current,  $I_{Ca(L)}$ . In departure from the general explanation given above,  $I_{Ca(L)}$  provides a depolarizing current against the repolarizing currents, that supports a plateau phase of the action potential (phase 2, Fig. 2.3). During the plateau phase, the two repolarizing potassium currents,  $I_{Kr}$  and  $I_{Ks}$ , slowly increase. Throughout this process, the sodium/calcium exchanger pumps ions across the membrane at a stoichiometry of 3  $Na^+$  to 1  $Ca^{2+}$ . Initially, the exchanger serves to extrude  $Na^+$  from the cell, although toward the end of the event it changes directions and pumps  $Ca^{2+}$  ion out of the cell, providing an inward current additionally prolonging the plateau phase. Eventually, the membrane potential causes the  $Ca^{2+}$  chan-

nels to close and a delayed rectifying  $K^+$  ion current,  $I_{K1}$ , restores the resting membrane potential [Kléber and Rudy, 2004, Alberts *et al.*, 1994].

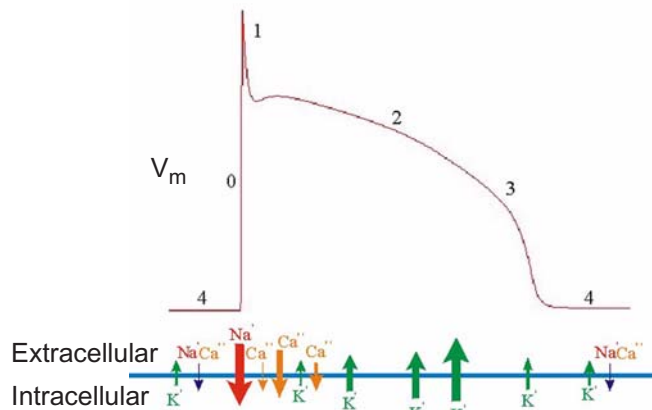


Fig. 2.3: Phases of the normal ventricular action potential (intracellular recording). The transmembrane ion currents are in the bottom of the figure.

One application area for the CMOS cell-based biosensor is the study of the pharmacological effect of candidate compounds on cardiomyocytes. This involves the classification of arrhythmia-causing drugs, as well as the establishment of safety regions. An arrhythmia occurs when the head of a propagating wave interacts with the repolarization phase of a preceding wave. That is, if the cell is stimulated while the membrane is still in the plateau phase, a rapid succession of action potentials may ensue. In an organism, this condition manifests itself as rapid, uncorrelated heart beats, termed fibrillation, which can be fatal. Therefore, any hindrance to the repolarization of the cell membrane, such as a blocking of the hERG potassium channel (encoded by the human ether-à-go-go-related gene), responsible for the rapidly activating delayed rectifier potassium current ( $I_{Kr}$ ), may lead to fatal arrhythmic trains of action potentials [Redfern *et al.*, 2003].

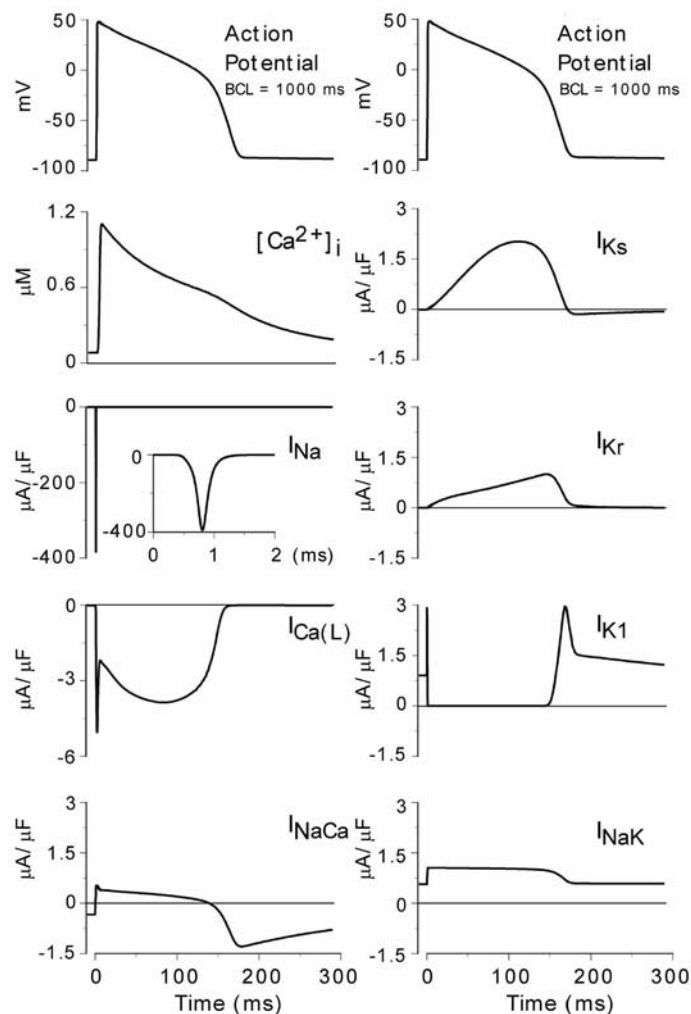
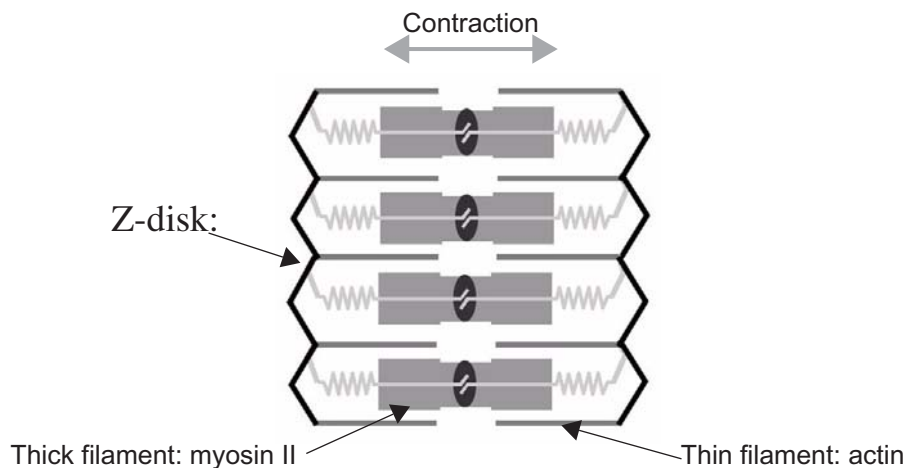


Fig. 2.4: Major ionic currents occurring during the cardiac action potential. Refer to Tab. 2.1 for a description of the currents cited.  $[Ca^{2+}]_i$  is the concentration of free calcium in the myoplasm [Kléber and Rudy, 2004].

## MUSCLE CONTRACTION

It is the transient increase of cytosolic  $Ca^{2+}$ , a result of the action potential, that triggers muscle contraction. This is termed excitation-contraction coupling. When the membrane is depolarized, voltage-sensitive proteins, located in membranous folds of the cell membrane (called transverse tubules or T tubules) cause large  $Ca^{2+}$  release channels in the sarcoplasmic reticulum to open, allowing  $Ca^{2+}$  to flow into the cytoplasm. An increase in cytosolic  $Ca^{2+}$  opens more  $Ca^{2+}$

release channels, thereby amplifying the response. The flooding of  $\text{Ca}^{2+}$  ions into the cytosol causes myofibrils to contract. Myofibrils are composed of repeating units of thin and thick proteinaceous filaments. The base unit of a myofibril is a contractible sarcomere (Fig. 2.5). A sarcomere comprises thin filaments, made up of the actin protein, that are arranged in a hexagonal lattice. In the center of the lattice are the thick filaments, which are made of the protein myosin-II. Tiny cross-bridges, called myosin-II heads, extend from the myosin filaments, intermittently making contact with adjacent actin filaments. During contraction, these myosin-II heads cause the actin and myosin-II filaments to slide relative to one another, converting ATP to adenosine diphosphate (ADP) in the process [Alberts *et al.*, 1994, Bers, 2003].



*Fig. 2.5: Schematic representation of 4 contractile sarcomere units. The light gray arrow indicates the direction of contraction. Figure courtesy of Preeti Ahuja.*

## NEURAL ACTION POTENTIAL

Perhaps one of the most amazing feats of biology is the propagation of unattenuated neural signals at high speeds over long distances. That the signal is self-amplifying is a characteristic of the positive feedback mechanism occurring during an action potential. As with the cardiac action potential, the neural counterpart is triggered when the membrane is depolarized, by a neurotransmitter or externally applied stimulus, enough to open the voltage-gated  $\text{Na}^+$  channels (i.e. from resting potential of  $-70$  mV to  $-55$  mV, Fig. 2.6, left). Sodium ions flow into the cells down their electrochemical gradient (see Fig. 2.7 for intra- and extracellular ion concentrations), further depolarizing the cell, in turn opening more  $\text{Na}^+$

channels, leading to a larger influx current, rapidly increasing the sodium ion transmembrane conductance (Fig. 2.6, right). This positive feedback is a rapid process resulting in the action potential reaching its maximum value in less than a millisecond. As the membrane potential approaches the reversal potential for  $\text{Na}^+$  of +60 mV, the electrochemical driving force of  $\text{Na}^+$  approaches zero. At this point, the  $\text{Na}^+$  ion channels close and are inactivated (they remain in this state until the membrane has returned to its resting potential for some milliseconds). Membrane depolarization causes the voltage-gated  $\text{K}^+$  channels to open, albeit much more slowly than their sodium counterparts (compare the time course for the ion channel conductances in the bottom curves of Fig. 2.6). Potassium ions flow out of the cell, down their electrochemical gradient, repolarizing the membrane. Before returning to its resting potential, the membrane is briefly hyperpolarized, during which time (known as the refractory period) the membrane is unresponsive to stimuli. This is yet another unique feature of neurons to accurately process information as it precludes the back-propagation of signals. Finally, active transport is used to pump  $\text{Na}^+$  and  $\text{K}^+$  against their electrochemical gradients, out and into the cell respectively, thus restoring the resting membrane potential.

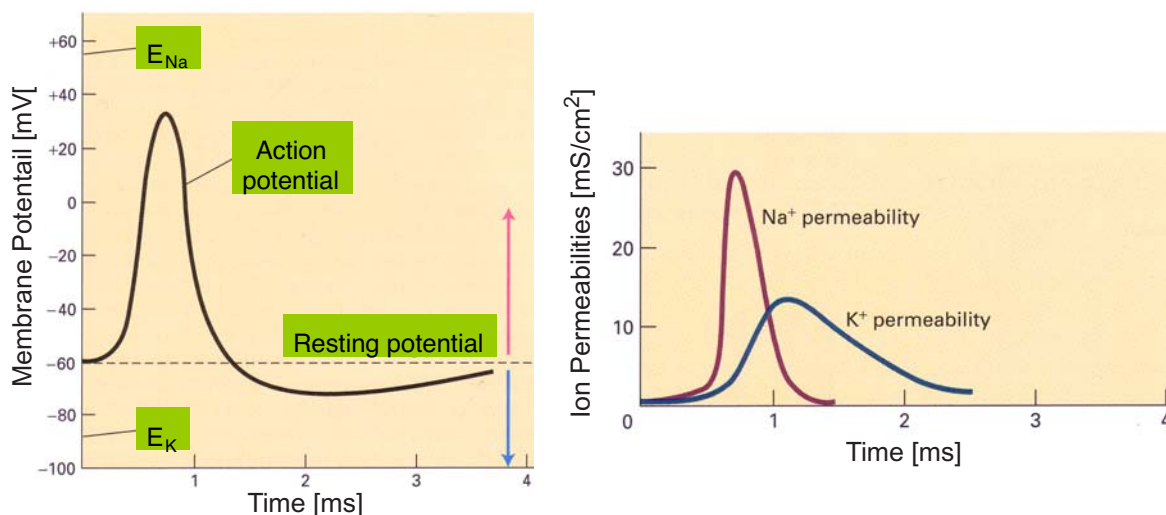


Fig. 2.6: The neural action potential (left) with corresponding sodium and potassium permeabilities (right) as determined by Hodgkin and Huxley in 1952 [Lodish et al., 2000]. Note the rapid increase in sodium ion channel conductance, in comparison to the relatively slow time course of the potassium ion channel conductance.



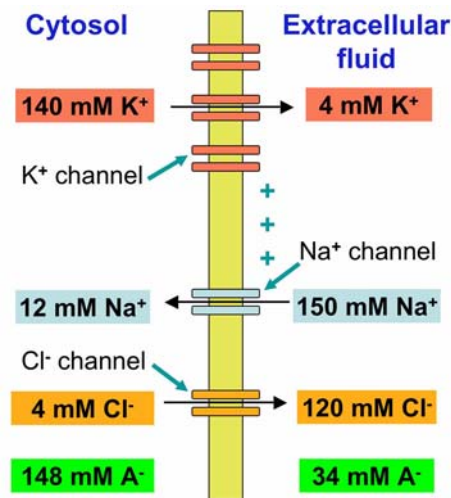


Fig. 2.7: Intra- and extracellular ion concentrations, with corresponding electromotive forces,  $E_i$ , for the species primarily involved in the electrogenic properties of the neural membrane,  $\text{Na}^+$ ,  $\text{K}^+$ , and  $\text{Cl}^-$  [Lodish et al., 2000]. Active transport of  $\text{Na}^+$  and  $\text{K}^+$  across the membrane, at a cost of 1 ATP molecule, is shown in the bottom of the figure.  $F_e$  and  $F_d$  represent the force generated by the local electric field across the membrane and the force of diffusion, respectively. Note that the outside of the membrane is considered to be positively charged.

### EQUIVALENT CIRCUIT MODEL

As a result of the extensive electrical characterization of the neural action potential performed over the last 60 years, an equivalent circuit is often used to model neural electrical activity. The model encompasses the electrogenic features of the membrane including: the variable transmembrane conductances of voltage-gated  $\text{Na}^+$ ,  $\text{K}^+$ , and leakage ion channels,  $g_{\text{Na}}$ ,  $g_{\text{K}}$ , and  $g_{\text{L}}$ ; the electromotive forces driven by the electrochemical potential across the membrane,  $E_{\text{Na}}$ ,  $E_{\text{K}}$ , and  $E_{\text{L}}$ ; and the  $\text{Na}^+$ - $\text{K}^+$  pump for active ion transport,  $I_a$  (Fig 2.8). The bilipid plasma membrane has a capacitive element, represented by  $C_m$ , and the potential across the membrane is  $V_m$ .

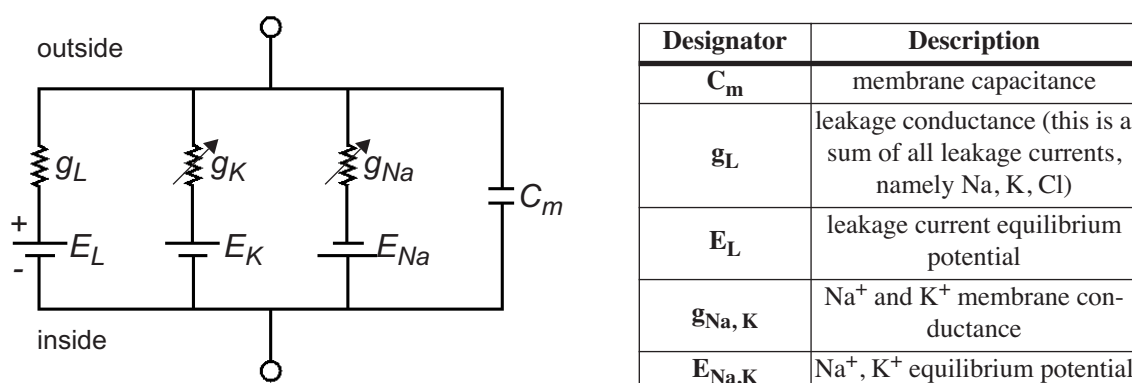


Fig. 2.8: Equivalent circuit model representing the membrane of a typical nerve cell. See table below for a description of the variables [Hodgkin and Huxley, 1952].

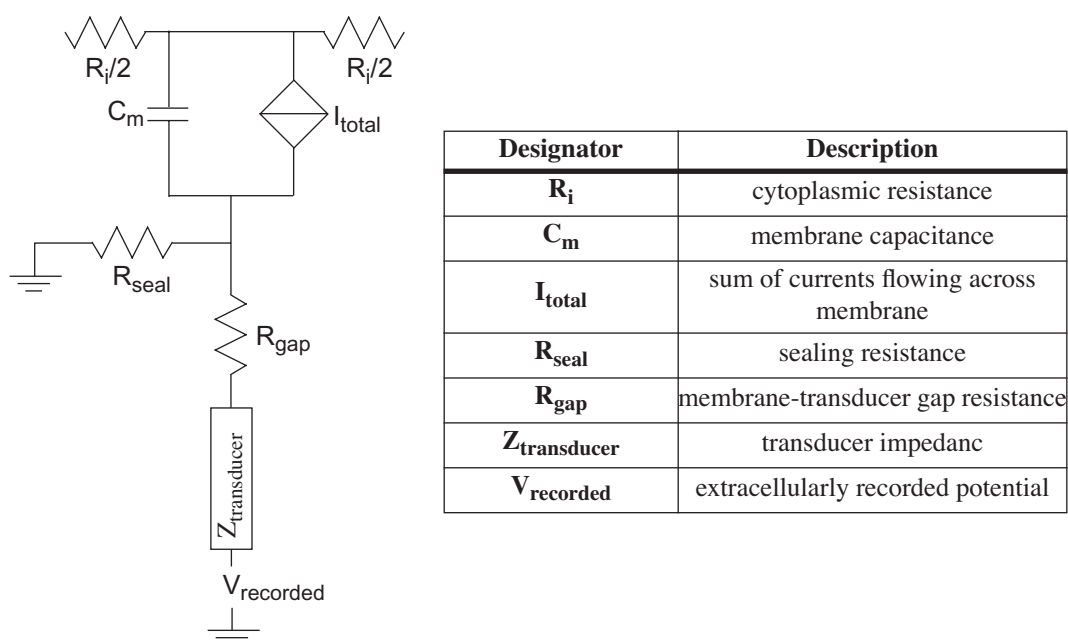


Fig. 2.9: Equivalent circuit of the electrogenic cell membrane-transducer interface, after Stenger and McKenna, 1994.

Combining this model with an equivalent circuit model of the electrode-electrolyte interface (see Appendix A), and the sealing resistance between the cell-electrode gap yields a complete model of the extracellularly recorded action potential given in Fig 2.9. This type of representation of the electrogenic cell-transducer

interface has been the focus of many research groups for the purpose of gaining an enhanced understanding of the processes contributing to the extracellular recording (the reader is referred to Grattarola *et al.*, 1995, Buitenweg *et al.*, 2003 and Ingebrandt *et al.*, 2004).

To conclude this section, a summary of the main differences and similarities between the neural and cardiac action potential is given in Tab. 2.2. Relevant details on the cell itself, such as size and availability, are also included.

Tab. 2.2: Summary of typical characteristics of neural and heart muscle cells<sup>a</sup>

	Cardiac Myocyte	Neuron
<b>AP Amplitude [intracellular, mV]</b>	100 mV	80 mV
<b>AP Duration [ms]</b>	1 - 100's ms	< 5 ms
<b>Intracellular Signal Propagation Velocity [m/s]</b>	1 (intercellular)	100 (myelinated) 1 (unmyelinated)
<b>Principle Ions</b>	Na <sup>+</sup> , K <sup>+</sup> , Ca <sup>2+</sup>	Na <sup>+</sup> , K <sup>+</sup>
<b>Ion Exchanger [per ATP molecule]</b>	3Na <sup>+</sup> ⇌ Ca <sup>2+</sup>	3Na <sup>+</sup> ⇌ 2K <sup>+</sup>
<b>Cell body Size [µm]</b>	30	10
<b>Culture Age When Cells Become Electrically [days <i>in vitro</i>]</b>	1 - 2	14 - 21
<b>Availability of Electrically Active Cell Line</b>	HL-1	ND 23/7 PC12 (not electrically active, commonly used)

- a. Note that these are typically values and may vary greatly with cell and culture type. They are nevertheless presented here to demonstrate that a measurement system requires a high degree of flexibility.

### 2.1.2 EXTRACELLULARLY RECORDED FIELD POTENTIALS

Extracellularly recorded field potentials are representative of the electrical activity of groups of cells or regions of the culture (Johnston and Wu, 1995). These signals are referred to as *field potentials*, as they represent a measurement of the surrounding electrical field. This is quite different from action potential recordings, such as patch clamp measurements, which are quantitative measurements of the ion currents flowing across the cell membrane. When recording extracellularly, the activity is typically measured between the working electrode, ideally located directly below the cell, and a distant reference electrode. The recorded

signal represents the activity in one or more cells, depending on the size of the cell relative to the size of the electrode. For recordings from slices of brain tissue, planar electrodes can detect spikes that are at most 50 - 60  $\mu\text{m}$  away, and this value will be bigger for cardiac myocytes, which produce larger signals [Egert *et al.*, 2001]. In the most complex case, activity is recorded from regions of the brain yielding electroencephalograms or EEGs.

Volume conductor theory is typically used to qualitatively describe the extracellular recording principle. Here the extracellular fluid is considered to be a volume conductor. When an action potential occurs, the cell becomes non-uniformly polarized, meaning different regions of the cell are at different potentials. This results in the flow of a local current and the generation of current sources and sinks. The non-uniformity in the membrane potential establishes an electric field that induces an electric charge on the surface of a conductor, for example an underlying metal electrode. The potential difference arising from the variation in electric charge on the working electrode versus a distant reference electrode is the recorded signal. The simplest case, a single action potential propagating over an external planar electrode, is depicted in Fig. 2.10. At  $t_1$ , the action potential occurs slightly to the left of the extracellular recording electrode. A current flows into the cell, at the site of the action potential, creating a current 'sink'. To preserve charge neutrality, current is drawn from the neighboring regions, creating a current 'source' on either side of the action potential site, as shown at  $t_2$ . A sink is recorded as a negativity, whereas a source is recorded as a positivity. Thus, an action potential propagating towards the extracellular electrode is recorded as a positive signal. As the signal travels over the electrode, the induced field changes direction, and a sharp negative down-swing is recorded. It is this point of steepest negative deflection, classically referred to as the point of 'intrinsic deflection' [Kleber and Rudy, 2004], that is defined as the point of local activation (i.e. the time at which the action potential occurs directly above the electrode). The action potential then travels away from the electrode, the region over the electrode once again becomes a current source, and a positivity is recorded. Therefore, an extracellularly recorded action potential is typically triphasic, although recordings made at the site of the pace-maker or at the edge of a syncytium (a confluent layer of cells) will be monophasic.

Many groups report that the field potential is related to the first derivative of the intracellular action potential, a result of the capacitance between the cell membrane and the planar electrode [Omura 1970, Halbach 2003]. Recall that

$I_C = C(dV/dt)$ . However, the shape of the recorded signal can vary greatly, from monophasic to triphasic and some research groups have even reported waveforms that are proportional to the action potential itself [Fromherz 2002].

### 2.1.3 FIELD POTENTIAL WAVEFORM ANALYSIS

When an action potential occurs in a group of cells in the immediate vicinity of planar microelectrode, a field potential (FP) is recorded. Although, traditionally information was considered to be contained in frequency-orientated parameters only, new research shows that biophysical information can be found in the shape of the waveform as well. The shape of the extracellularly recorded waveform is affected by many variables, such as the membrane-electrode spacing, ion-channel conductances, cell-electrode coupling or sealing resistance, and intercellular resistance [Sproessler 1999]. The goal of waveform analysis is to be able to identify certain parameters that can be extracted from the signal waveform, for example amplitude and duration of unique components. Ideally, these parameters are standardized and are common to waveforms recorded at several electrodes within the same preparation, or from various preparations. The parameters are correlated to biophysical processes occurring in the cell and, hence, are used to study the pharmacological effect of a test compound, or physiological and pathophysiological changes within the culture. In this section, waveform analysis is presented for cardiomyocytes only. Conversely, biosensing analysis for neurons largely employs frequency-dependent parameters, for example firing rate, average bursting rate and average burst duration [Gross *et al.*, 1997, Morefield *et al.*, 2000].

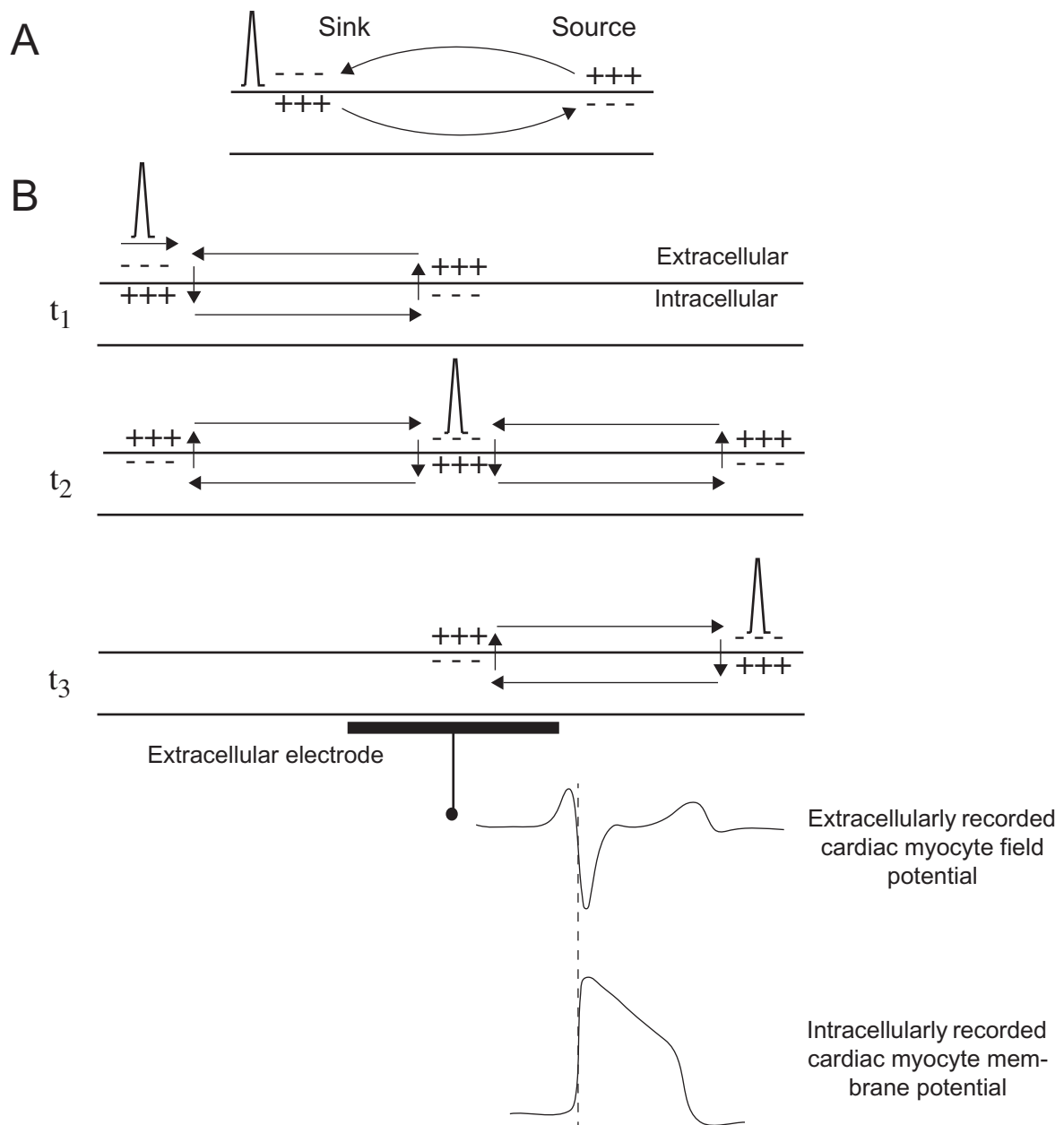


*Fig. 2.10: Recording principle of an extracellularly recorded action potential as explained using volume conductivity theory. The shape of the action potential is a result of currents flowing towards and away from the electrode creating current sinks and sources, A. This is depicted as the action potential travels towards the extracellular electrode,  $t_1$ , over the electrode,  $t_2$ , and away from the electrode,  $t_3$ , B. The arrows indicate the direction of current flows. Adapted from Johnston and Wu, 1995 and Kleber and Rudy, 2004.*

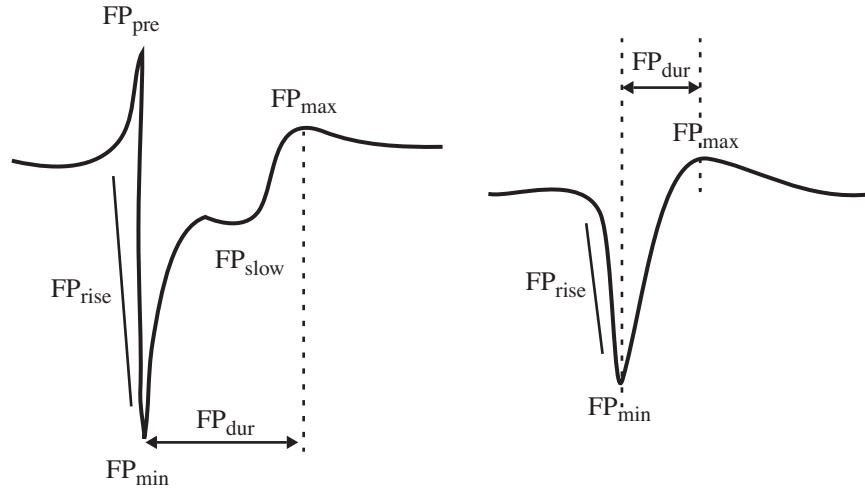


Fig. 2.11: Typical field potential waveforms measured from spontaneously beating embryonic mouse cardiac myocytes and the parameters that are used to characterize them. Adapted from Halbach, et al., 2003.

Tab. 2.3: Description of parameters used in Fig. 2.11 [Halbach et al., 2003].

Variable	Description
$FP_{pre-time}$ and $FP_{pre-amp}$	Timing and amplitude of $FP_{pre}$ , the first positive peak
$FP_{min-time}$ and $FP_{min-amp}$	Timing and amplitude of $FP_{min}$ , the first negative peak
$FP_{max-time}$ and $FP_{max-amp}$	Timing and amplitude of $FP_{max}$ , the last positive peak
$FP_{slow-time}$ and $FP_{slow-amp}$	Timing and amplitude of $FP_{slow}$ , the last negative peak before $FP_{max}$
$FP_{dur}$	Time between $FP_{min}$ and $FP_{max}$
$FP_{rise}$	time for the voltage to decline from the baseline to $FP_{min}$ (from 10% of $FP_{min}$ to 90% of $FP_{min}$ )

## CARDIOMYOCYTES

In an attempt to quantize specific aspects of the waveform, key features have been identified, see Fig. 2.11 and Tab. 2.3. It has been experimentally determined by Banach and co-workers that  $FP_{dur}$  and  $FP_{rise}$  are proportional to the APD90 (the duration of the intracellularly recorded action potential to 90% repolarization), and the rise time of the action potential, respectively. Additional attempts to correlate these FP characteristics to physical processes occurring during an action potential have yielded compelling results.  $FP_{rise}$  can also be used to differentiate the pace maker cell from the rest of the preparation. The pace maker cell is characterized by a slow depolarization which translates into an absence of the

$FP_{pre}$  peak;  $FP_{rise}$  of the culture's pacemaker cells can be 5-times greater than  $FP_{rise}$  throughout the rest of the frequency entrained culture [Halbach 2003, Sprossler 1999]. Blocking the voltage-dependent  $Na^+$  channels with tetrodotoxin (TTX), or replacing the medium with a  $Na^+$ -free medium, results in a reduction of  $FP_{min}$ , an increase in  $FP_{slow}$  and a lengthening of the FP duration, which is expected since the absence of  $Na^+$  will prolong the corresponding action potential rise-time [Rohr 1998]. Similarly, the absence of  $Ca^{2+}$  is known to shorten the action potential duration (recall that  $I_{Ca}$  is responsible for supporting the plateau phase of the action potential). The use of a  $Ca^{2+}$ -free medium or Nimodipine, a  $Ca^{2+}$ -channel blocker, results in the disappearance of  $FP_{slow}$  and a decrease in  $FP_{dur}$ .  $FP_{pre}$  is attributed to an outward current that occurs simultaneously to the depolarization of surrounding cells [Halbach *et al.*, 2003, Yamamoto *et al.*, 1998]. These findings demonstrate the potential of a cardiomyocyte-based biosensor as a platform for pharmacological investigations.

### 2.1.4 INTERFACE IMPEDANCE

A key parameter in the transduction of action potentials is the interface impedance because of its affect on noise. Thermal noise is directly proportional to the impedance of an electrode-electrolyte interface, which is inversely proportional to the electrode area. For high spatial resolution recordings (for example, to follow the electrical signal propagation through a neural culture) it is necessary to shrink the electrode dimensions thereby increasing the electrode thermal noise. To preserve the total electrode area, while reducing the overall electrode dimensions, techniques are applied to roughen the electrode surface. These techniques include mechanical roughening of the surface, the deposition of platinum black [Feltham *et al.*, 1971], or a complex electrochemical process where platinum is oxidized to form an irregular surface and then reduced back to pure platinum known as the HiQ electrode, a proprietary material developed by Cochlear Ltd. [Tykocinski *et al.*, 2001].

A carefully designed and well-understood cell-electrode interface is crucial to the successful recording and stimulation from planar metallic electrodes. To this end an equivalent circuit model, where each parameter represents a macroscopic physical process contributing to the interface impedance, has been validated (this theory is presented in its entirety in Appendix A, and only a brief summary will be reported here). Electrochemical impedance spectroscopy (EIS) has been used to electrically characterize various electrode materials and sizes: bright platinum



(1 cm<sup>2</sup>), platinum black (1 cm<sup>2</sup> and 900 μm<sup>2</sup>) and titanium nitride (1 cm<sup>2</sup>). The equivalent circuit model comprises an interface capacitance, shunted by a charge transfer resistance, together in series with the solution resistance. Values for these individual circuit elements have been derived from the fitted experimental EIS results. To confirm the veracity of the equivalent circuit model, theoretical equations have been used to independently calculate the parameter values. These calculated parameter values are in good agreement with experimental findings, indicating that the equivalent circuit model can indeed be used to model the interface impedance. As an extension of this theory, the model has been used to quantify the effects of protein adhesion promoters (laminin and poly-L-lysine) and incubation time on the impedance.

The clear advantage of having such a model as a design tool is that new materials and surface treatments (such as surface roughening techniques or adhesion coatings) can be evaluated and compared with existing methods. For example, an evaluation of a high-surface area, nanostructured gold material was performed, the results of which are given in section 3.3.

## 2.2 CELL ADHESION

A general discussion on the adhesion of a typical vertebrate cell to a solid substrate is given here. Three main units are involved in the adhesion of a cell to a substrate: the cytoskeleton, transmembrane proteins, known as integrins, and the extracellular matrix (ECM) with its complex scaffolding apparatus. The cytoskeleton consists of three protein filaments: actin filaments, microtubules, and intermediate filaments. Collectively these filaments give strength, help facilitate mobility and serve to organize the cytoskeleton. On the outside of the cell, a complex mixture of secreted extracellular macromolecules makes up the ECM. These macromolecules can be divided into two classes: glycosaminoglycans (GAGs) in the form of a hydrated gel that resists compressive forces on the matrix, and the fibrous proteins, providing tensile strength (e.g. collagen) as well as sites for cell adhesion (e.g. fibronectin and laminin). It is the role of the integrins to link these two systems together.

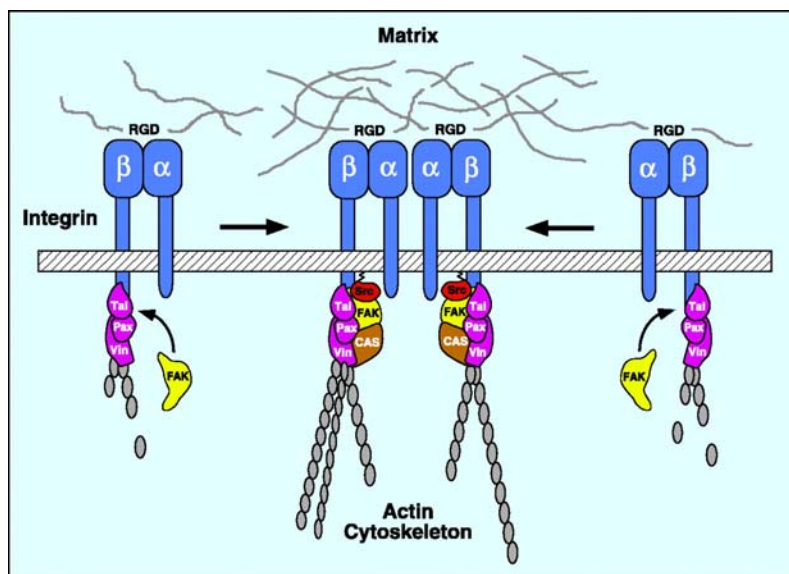


Fig. 2.12: Schematic showing relationship between fibronectin in the extracellular matrix, integrin transmembrane proteins, and the actin cytoskeleton [Giancotti and Ruoslahti, 1999]. In this simplified diagram, the integrin linker proteins bind only to the RGD motif.

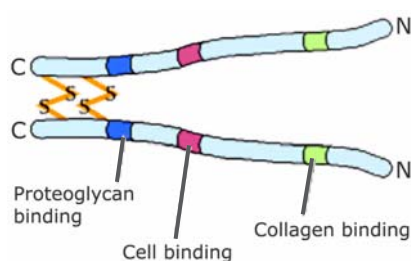


Fig. 2.13: Schematic of the main binding sites of fibronectin (from Cooper, 2000).

Fibronectin and laminin are the two proteins known to mediate cell adhesion [Beck *et al.*, 1990]. Adhesive proteins consist of multiple domains which are specific binding sites for other matrix molecules or for receptors on cell surfaces (see Fig. 2.13). For example, the major cell binding site in fibronectin, and other adhesive proteins, contains the

RGD amino acid sequence (see Fig. 2.14 for the chemical structure). If this RGD sequence is immobilized on a solid substrate in the correct concentration, then it is known that cells (with the exception of neurons) will be immobilized at the surface [D'Souza *et al.*, 1991, VandeVondele, *et al.*, 2003, Tosatti *et al.*, 2003, Tosatti *et al.*, 2004,]

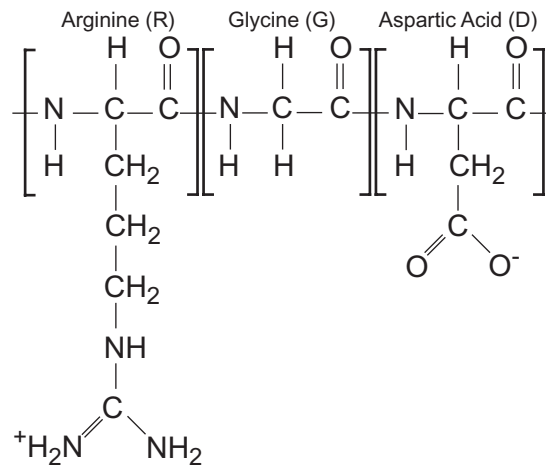


Fig. 2.14: Chemical formula of the RGD amino-acid sequence attributed to adhesion mediation between the integrin transmembrane linker protein and the extracellular matrix.

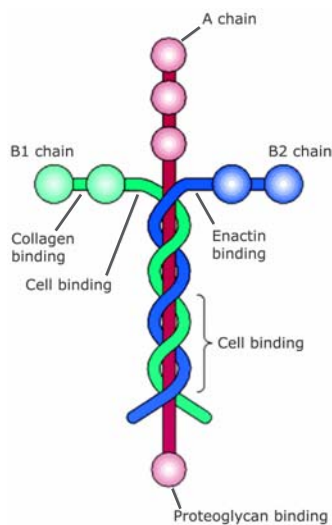


Fig. 2.15: Schematic of laminin adhesive protein showing the main binding sites (from Cooper, 2000).

Laminin is an integral part of the basal laminae, the thin mat of specialized ECM that underlies all epithelial cell sheets and tubes. It surrounds individual muscle cells, fat cells and Schwann cells. Laminin is a large glycoprotein with 3 polypeptide chains containing functional domains that bind to laminin-receptor integrin proteins on the cell surface (among others), see Fig. 2.15.

During cell adhesion, the adhesive ligands bind simultaneously, albeit weakly, to many of their respective receptor sites in the transmembrane integrin protein, see Fig. 2.12. The integrin protein is composed of 2 non-covalently bound glycoprotein subunits,  $\alpha$  and  $\beta$ . Integrin binding to ECM proteins may be highly selective or weakly selective: some integrins bind to the RGD motif only, while others recognize several domains. When a receptor binds to a ligand in the matrix it triggers a complex cascade of events initiating the

assembly of intracellular attachment proteins, namely the binding of actin filaments to the integrin protein via several intermediary proteins, as well as activating intracellular signaling pathways. In some simplistic models used to develop engineered surfaces for cell adhesion, the periphery of the integrin protein is considered to be negative and hence a positive surface will attract the cell. The surface of the integrin may be hydrophilic, leading to interaction and some form of adhesion between integrins and a positive substrate. However, certain pathways may not be triggered as would be the case if the cell were in contact with certain proteins from the ECM. For example, neurons are extremely sensitive and may not develop neurites if they are not cultured on the appropriate surface. Hence, certain differentiation of the cell must be demonstrated in order to establish that an adequate phenotype is conserved. This is not to say that the cell should act and behave exactly as if it were *in vivo*, yet certain basic cellular structures and functions should be present. With respect to the patterned adhesion strategy presented in this work, the functionalized surfaces may be subsequently incubated in fibronectin, or laminin, which will adhere to the amino groups only, therefore presenting the surface with an appropriate surface for cell adhesion and differentiation.

An good example of how sensitive cellular operations may be to the extracellular environment is demonstrate by Fig. 2.16. The figure shows electrical activity from neurons of the same type (cat V1) measured *in vitro* (left) and *in vivo* (center). Activity was elicited using an identical constant-current stimulation protocol. The spike trains vary greatly between the two cases. That is, the spike trains from a slice of neocortical tissue is regular, in comparison to the irregular spike response measured in the cortex of the intact animal.

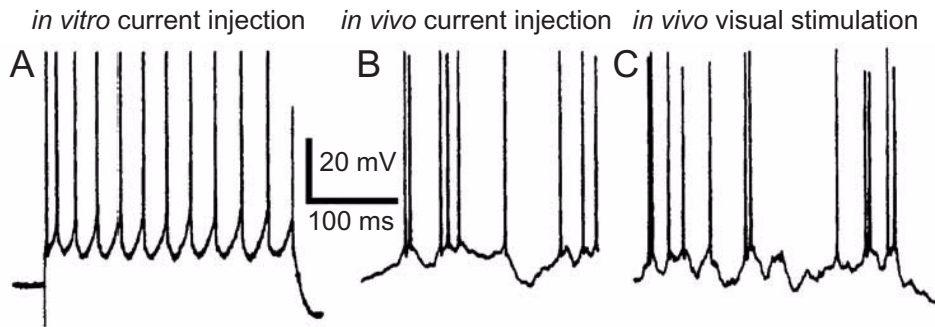


Fig. 2.16: Neural response depends on whether the experiment was performed *in vivo* or *in vitro* [Holt et al., 1996]. Spike trains recorded under three different experimental conditions: *in vitro* stimulation of cat V1 neuron by constant-current stimulation, A; *in vivo* stimulation of cat V1 neuron by constant-current stimulation, B; *in vivo* visual stimulation, C. The stimulation protocol in case A and B was identical.

## 2.3 SUMMARY

In this chapter, theory supporting the understanding and design of a cell based biosensor was presented. This includes a description on the action potential signal itself and the extracellular recording principle. To introduce how a CBB might be used to test the pharmacological effect of a test compound on a cardiomyocyte, a discussion on waveform analysis was included. Although a CBB will not yield quantitative information on ion-channel currents, it has the potential to perform valuable qualitative analyses.

A section on the mechanisms underlying cell adhesion was presented. This was intended to highlight the importance of the cell environment, as a parameter that can significantly alter cell functioning. Hence, cell adhesion requires careful consideration when designing the CBB. A second intention of the section was to introduce the difference between the *in vitro* and *in vivo* cell. As is clearly demonstrated in Fig. 2.16, cellular response varies greatly with environment.

## 2.4 REFERENCES

- Alberts, B., Bray, D., Lewis, J., Raff, M., Roberts, K., and Watson, J. (1994). *The Cell*, Garland Publishing.
- Beck, K., Hunter, I., and Engel, J. (1990). "Structure and function of laminin: anatomy of a multidomain glycoprotein." *Faseb J*, 4(2), 148-60.
- Bers, D. M. (2001). *Excitation-Contraction Coupling and Cardiac Contractile Force*, Kluwer Academic, London.
- Buitenweg, J. R., Rutten, W. L., and Marani, E. (2003). "Geometry-based finite-element modeling of the electrical contact between a cultured neuron and a microelectrode." *IEEE Trans Biomed Eng*, 50(4), 501-9.
- Cooper, G. M. (2000). *The cell: A molecular approach*, Sinauer Associates Inc., Boston.
- D'Souza, S. E., Ginsberg, M. H., and Plow, E. F. (1991). "Arginyl-glycyl-aspartic acid (RGD): a cell adhesion motif." *Trends in Biochemical Sciences*, 16, 246-250.
- Dayan, P., Abbott, L. (2001). *Theoretical Neuroscience: Computational and Mathematical Modeling of Neural Systems*, MIT Press, Cambridge.
- Egert, U., Heck, D., and Aertsen, A. (2002). "Two-dimensional monitoring of spiking networks in acute brain slices." *Exp Brain Res*, 142(2), 268-74.
- Feltham, A. M., and Spiro, M. (1971). "Platinized Platinum Electrodes." *Chemical Reviews*, 71(2), 177-&.
- Fromherz, P. (2002). "Electrical interfacing of nerve cells and semiconductor chips." *Chemphyschem*, 3(3), 276-284.
- Giancotti, F. G., and Ruoslahti, E. (1999). "Integrin Signaling." *Science*, 285(5430), 1028-1033.
- Grattarola, M., Bove, M., Martinoia, S., and Massobrio, G. (1995). "Silicon neuron simulation with SPICE: tool for neurobiology and neural networks." *Medical & Biological Engineering & Computing*, 33(4), 533-6.

- Gross, G. W., Harsch, A., Rhoades, B. K., and Gopel, W. (1997). "Odor, drug and toxin analysis with neuronal networks *in vitro*: Extracellular array recording of network responses." *Biosensors & Bioelectronics*, 12(5), 373-393.
- Halbach, M., Egert, U., Hescheler, J., and Banach, K. (2003). "Estimation of action potential changes from field potential recordings in multicellular mouse cardiac myocyte cultures." *Cell Physiol Biochem*, 13(5), 271-84.
- Ingebrandt, S., Yeung, C. K., Krause, M., and Offenhausser, A. (2004). "Neuron-transistor coupling: interpretation of individual extracellular recorded signals." *Eur Biophys J*.
- Johnston, D., Wu, S. (1995). *Foundations of Cellular Neurophysiology*, The MIT Press, London.
- Kandel, E. R., Schwartz, J. H., Jessell, T. M. (2000). *Principles of Neural Science*, McGraw-Hill, London.
- Kleber, A. G., and Rudy, Y. (2004). "Basic mechanisms of cardiac impulse propagation and associated arrhythmias." *Physiological Reviews*, 84(2), 431-88.
- Nosek, N. M., ed. *Essentials of Human Physiology*, online at: <http://www.imc.gsm.com/demos/hpdemo/program/start.htm>.
- Morefield, S. I., Keefer, E. W., Chapman, K. D., and Gross, G. W. (2000). "Drug evaluations using neuronal networks cultured on microelectrode arrays." *Biosensors & Bioelectronics*, 15(7-8), 383-96.
- Omura, Y. (1970). "Relationship between transmembrane action potentials of single cardiac cells and their corresponding surface electrograms *in vivo* and *in vitro*, and related electromechanical phenomena." *Trans N Y Acad Sci*, 32(8), 874-910.
- Redfern, W. S., Carlsson, L., Davis, A. S., Lynch, W. G., MacKenzie, I., Palethorpe, S., Siegl, P. K., Strang, I., Sullivan, A. T., Wallis, R., Camm, A. J., and Hammond, T. G. (2003). "Relationships between preclinical cardiac electrophysiology, clinical QT interval prolongation and torsade de pointes for a broad range of drugs: evidence for a provisional safety margin in drug development." *Cardiovasc Res*, 58(1), 32-45.

Rohr, S., Kucera, J. P., and Kleber, A. G. (1998). "Slow conduction in cardiac tissue, I: effects of a reduction of excitability versus a reduction of electrical coupling on microconduction." *Circ Res*, 83(8), 781-94.

Sprossler, C., Denyer, M., Britland, S., Knoll, W., and Offenhausser, A. (1999). "Electrical recordings from rat cardiac muscle cells using field-effect transistors." *Physical Review E*, 60(2), 2171-2176.

Stenger, D. A., McKenna, T. M. (1994). *Enabling Technologies for Cultured Neural Networks*, Academic Press, London.

Tosatti, S., Paul, S. M. D., Askendal, A., VandeVondele, S., Hubbell, J. A., Tengvall, P., and Textor, M. (2003). "Peptide functionalized poly(-lysine)-g-poly(ethylene glycol) on titanium: resistance to protein adsorption in full heparinized human blood plasma." *Biomaterials*, 24(27), 4949-4958.

Tosatti, S., Schwartz, Z., Campbell, C., Cochran, D. L., VandeVondele, S., Hubbell, J. A., Denzer, A., Simpson, J., Wieland, M., Lohmann, C. H., Textor, M., and Boyan, B. D. (2004). "RGD-containing peptide GCRGYGRGDSPG reduces enhancement of osteoblast differentiation by poly(L-lysine)-graft-poly(ethylene glycol)-coated titanium surfaces." *J Biomed Mater Res*, 68A(3), 458-72.

Tykocinski, M., Duan, Y., Tabor, B., and Cowan, R. S. (2001). "Chronic electrical stimulation of the auditory nerve using high surface area (HiQ) platinum electrodes." *Hear Res*, 159(1-2), 53-68.

VandeVondele, S., Voros, J., and Hubbell, F. (2003). "RGD-grafted poly-l-lysine-graft-(polyethylene glycol) copolymers block non-specific protein adsorption while promoting cell adhesion." *Biotechnology and Bioengineering*, 82(7), 784-790.

Yamamoto, M., Honjo, H., Niwa, R., and Kodama, I. (1998). "Low-frequency extracellular potentials recorded from the sinoatrial node." *Cardiovascular Research*, 39(2), 360-372.



---

# 3 EXPERIMENTAL METHODS

The realization of a CMOS cell-based biosensor (CBB) primarily involves chip fabrication and cell culturing. In this case, the fabrication of the CMOS chip is out-sourced to an industrial foundry. Since the conductors available in a typical CMOS process are not biocompatible, in-house post-processing is required to form biocompatible electrodes. The chip is wire-bonded and packaged in a way that protects the bond wires from the culture medium. At each processing step, care must be taken to ensure the stability of the packaged chip, since the culturing conditions (elevated temperature, saline solution and high humidity) present a rather unfriendly environment. Conversely, the package materials and chip surface must be selected to ensure that the cells survive long-term culturing. This is particularly relevant to neurons, which are extremely sensitive to their environment, and must be maintained for at least 2 - 3 weeks, when they become electrically active. In short, the chip must survive the harsh cell culture environment and the cells must survive in the unnatural *in vitro* environment.

Another key aspect of the CBB is the impedance characterization of the electrode-electrolyte interface. As introduced in Chapter 2, this is performed by electrochemical impedance spectroscopy (EIS). Additionally, EIS can be used as a tool to evaluate candidate electrode materials and surface treatments. In addition to the model presented in Appendix A, EIS was used in this work to investigate an alternative electrode material, a nanostructured gold. The material was selected because the nanostructure, comprising nanowires, has a larger surface area which reduces impedance. Different nanostructured gold materials, meaning surface with nanowires of varying physical dimensions, were fabricated and the impedance was measured<sup>1</sup>. The nanostructured gold with the best impedance characteristic was then compared with other electrode materials, such as bright platinum and platinum black, to determine the optimal electrode material.

In this chapter, the first section describes the post-processing of the CMOS chip. This includes a discussion on the selection of the electrode material, the fabrication of the gold nanowire material, the shifted-electrode design, and experiment

---

1. The gold nanowire investigation was performed by Marco Zappa as a semester project jointly led by the BioInterfaces Group and the Physical Electronics Laboratory.

results demonstrating the stability of the chip under culture conditions. The next section outlines the packaging scheme as a way to protect the bond wires and to form the culture bath. In the third section, impedance measurements of potential electrode materials are then presented. The chapter concludes with a discussion of the culturing of cardiomyocytes, the cell type primarily used in this work.

### 3.1 CMOS POST-PROCESSING

In a typical CMOS process the available conductive materials are limited to polycrystalline silicon, doped silicon, and aluminum (Al)<sup>1</sup> [Trapp *et al.*, 1985]. This list is further limited by CMOS design rules, that specify which layers can be exposed, or opened, and how much may be exposed. As a result, Al was selected as the contact material and post-processing was used to cover the Al with a bio-compatible material, such as platinum or gold, thereby forming the measurement electrode. However, since the standard electrode potential of Al (-1.66 V) is significantly more negative than that of platinum (Pt, +1.20 V) or gold (Au, +1.69 V), contacting Al to a noble metal, in the presence of an electrolyte such as the culture medium, creates a galvanic cell. If the Al is not properly sealed, and both the Al and Pt are in contact with the culture medium, then the Al will spontaneously dissolve. Therefore, care must be taken to adequately cover areas of exposed Al.

#### 3.1.1 ELECTRODE MATERIAL

In addition to Au and Pt, many different materials have been developed as the cell contact material: titanium nitride (TiN), iridium oxide (IrO), and HiQ platinum (a proprietary material from Cochlear Ltd.) [Stenger and McKenna 1994, Janders *et al.*, 1997, Maher *et al.*, 1999, Tykocinski *et al.*, 2001]. The key requirements for the electrode material are biocompatibility, process compatibility, low impedance and high charge storage capacity. This last requirement refers to the fact that, in the ideal case no faradaic currents should flow since the products of redox reactions may damage the cells. For example, the charge storage capacity for IrO, Pt and TiN is reported to be 4 mC/cm<sup>2</sup>, 400  $\mu$ C/cm<sup>2</sup> and 0.87 mC/cm<sup>2</sup> [Weiland *et al.*, 2002], indicating that IrO is the best material in this respect. Low impedance is particularly important when small-area electrodes are to be used, i.e. for high

---

1. In exceptional cases, palladium [Lehmann *et al.*, 2001], copper or silicide may be available.

spatial resolution recordings. A smaller electrode area becomes more sensitive to random charge fluctuations, introducing noise to the recorded signal. As a result, techniques are used to increase the total electrode surface area, such as surface roughening [Stenger and McKenna 1994]. Surface roughening serves to increase the total or effective surface area, while allowing the geometric, the two-dimensional surface area, to remain constant. The most common surface roughening technique is the electrochemical deposition of dendritically structured Pt, referred to as Pt black [Gesteland *et al.*, 1959, Feltham and Spiro, 1971], which can be deposited on either Au or Pt [Maher *et al.*, 1999]. As an alternative optimization technique, chemical modification is used. This involves the formation of highly conductive oxide layers under anodic conditions. Iridium oxide is the best example of this treatment, although its widespread application is hampered by high film stress [Borkholder *et al.*, 1998].

### NANOSTRUCTURED GOLD

As a high surface area material suitable for biocompatible applications, a nanostructured gold material was investigated, Fig. 3.1. Gold is a particularly useful electrode material because it can be chemically functionalized directly with a self-assembled monolayer (SAM). The material is structured using the template synthesis technique as described in Forrer *et al.*, 2000. To form the nanoporous template, Al is oxidized anodically in phosphoric acid to alumina, step A in Fig. 3.2. Pore dimensions, length and diameter, can be controlled by varying the anodization conditions (voltage, current density and electrolyte concentration). The nanopores are seeded with Au nanoparticles by applying an anodic AC potential to a bath containing Au particulate. Electroless deposition is used to fill the nanopores with Au and to deposit a thin, 10 - 20  $\mu\text{m}$ , top Au layer, step B in Fig. 3.2. The alumina is subsequently removed in a NaOH solution, thereby releasing the gold nanowires, step C in Fig. 3.2.

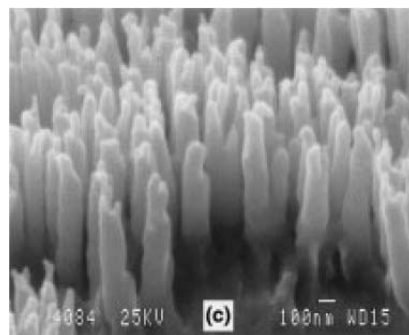
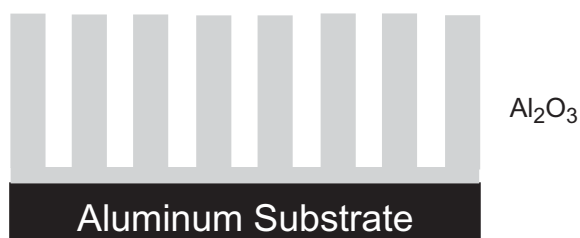


Fig. 3.1: SEM of nanostructured Au, Forrer *et al.*, 2000.

A. Anodic oxidation of aluminum in phosphoric acid.



B. Electroless deposition to fill nanopores.



C. Etch aluminum and alumina in NaOH.

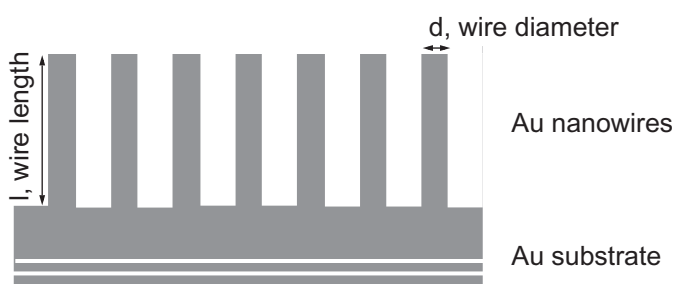


*Fig. 3.2: Schematic representation of the gold nanowire formation (after Forrer et al., 2000). The white horizontal lines in the gold substrate indicate that it is much thicker, 10 - 20  $\mu\text{m}$ , than the length of the nanowire, hundreds of nm's.*

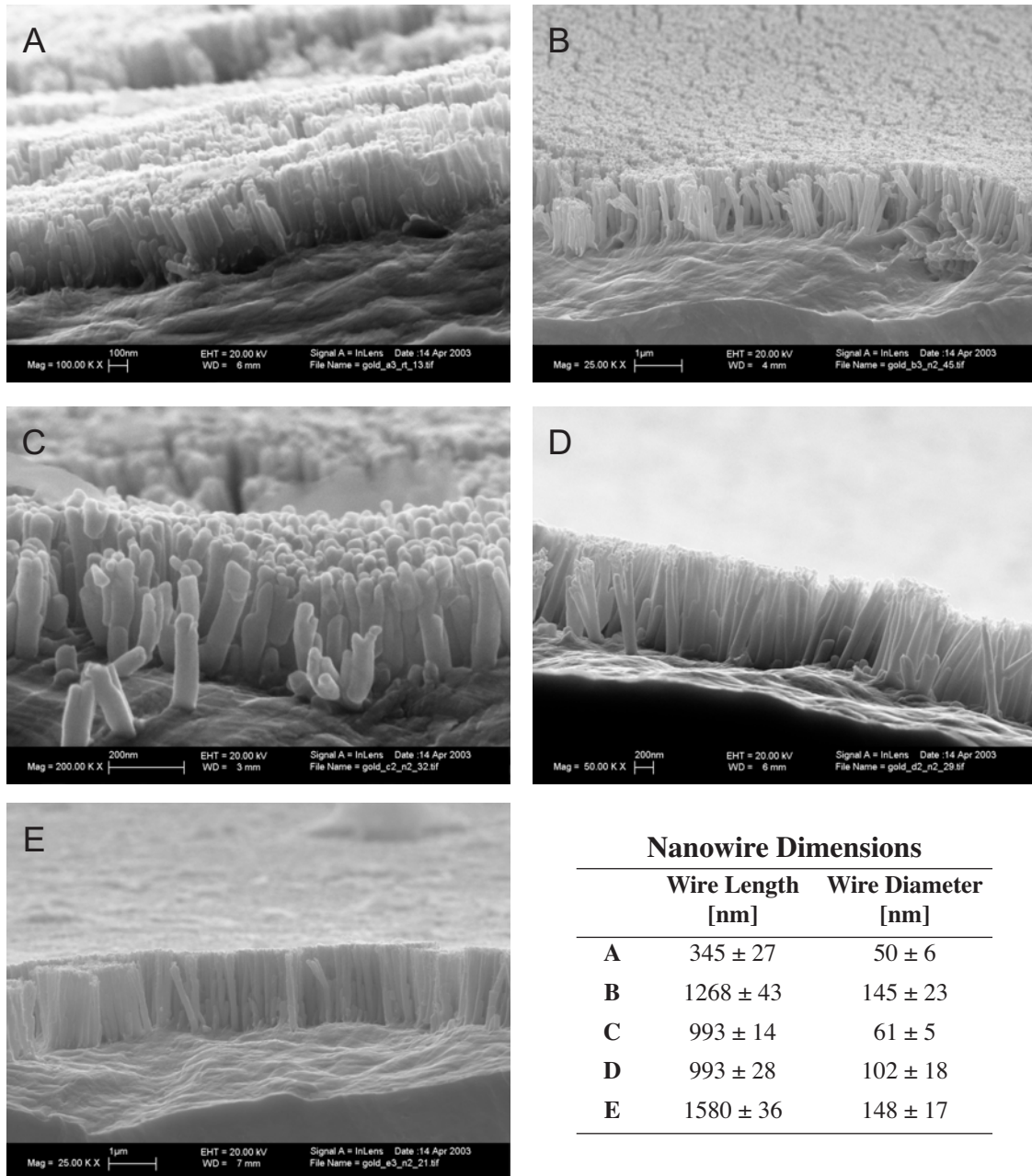


*Fig. 3.3: Gold nanowires of varying dimensions. The table gives the dimensions,  $d$ , wire diameter and  $l$ , wire length, for the 5 different gold nanowires.*

### 3.1.2 SHIFTED ELECTRODE DESIGN

Post-processing is required to cover the Al from the CMOS process with a bio-compatible material, and to seal the metals to avoid undesirable electrochemistry. A shifted-electrode design was developed to achieve both of these goals, see Fig. 3.4.

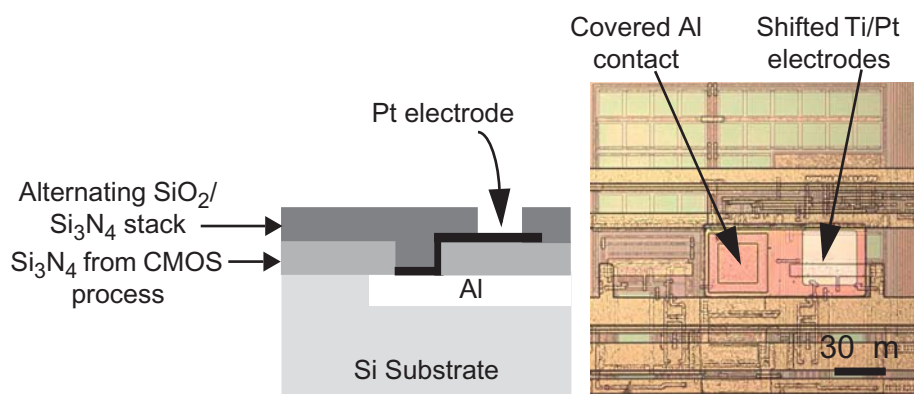


*Fig. 3.4: Cross-section (left) and image (right) of the covered Al contact and the shifted TiW/Pt electrode. The image shows one repeatable unit of circuitry (see Sec. xx).*

The processing is described briefly in Appendix B, and a more detailed description is given here. The starting point of the process is a CMOS wafer<sup>1</sup> with openings in the passivation to the Al contacts. To form the electrode metal, 50 nm of TiW (an adhesion promoter) followed by 270 nm Pt are sputter-deposited to cover the Al, and structured in a lift-off process. An alternating stack of silicon dioxide (SiO<sub>2</sub>) and silicon nitride (Si<sub>3</sub>N<sub>4</sub>), comprising 1.0 μm Si<sub>3</sub>N<sub>4</sub>, followed by two times 100 nm SiO<sub>2</sub> and 200 nm Si<sub>3</sub>N<sub>4</sub> for a total thickness of 1.6 μm, is deposited by plasma enhanced chemical vapor deposition (PECVD) to seal the metals. In later processing an additional top layer of 100 nm SiO<sub>2</sub> was added to prepare the surface for functionalization. It was necessary to deposit such a thick stack for stability purposes, because the presence of pinholes could lead to metal dissolution. As more passivation layers are present, the probability that a pinhole extends to the metal is significantly reduced (discussed further in the following section). Finally, a reactive ion etch (RIE) is used to etch through the passivation stack, thereby defining the measurement electrode size and shape. The advantage

1. This is true for the 2<sup>nd</sup>-generation design. For the 1<sup>st</sup>-generation design, individual chips were processed. See Chapter 5 for the description of the 1<sup>st</sup>- and 2<sup>nd</sup>-generation CMOS chips.

of this post-processing is the flexibility it affords with respect to the electrode material, size, shape, and location. For example, it is possible to draw the electrodes into a tight cluster, left image Fig 3.5, or small, isolated clusters, right image Fig. 3.5. Electrodes with varying sizes (right image, Fig. 3.5) may be fabricated on the same chip and used to optimize the electrode size. Since all other experimental conditions are kept constant, i.e. culture conditions, the effect of electrode size on the amplitude of the recorded signal can be accurately determined. Flexibility is further enhanced by the fact that the post-processing requires only two masks. A redesign is therefore relatively inexpensive.

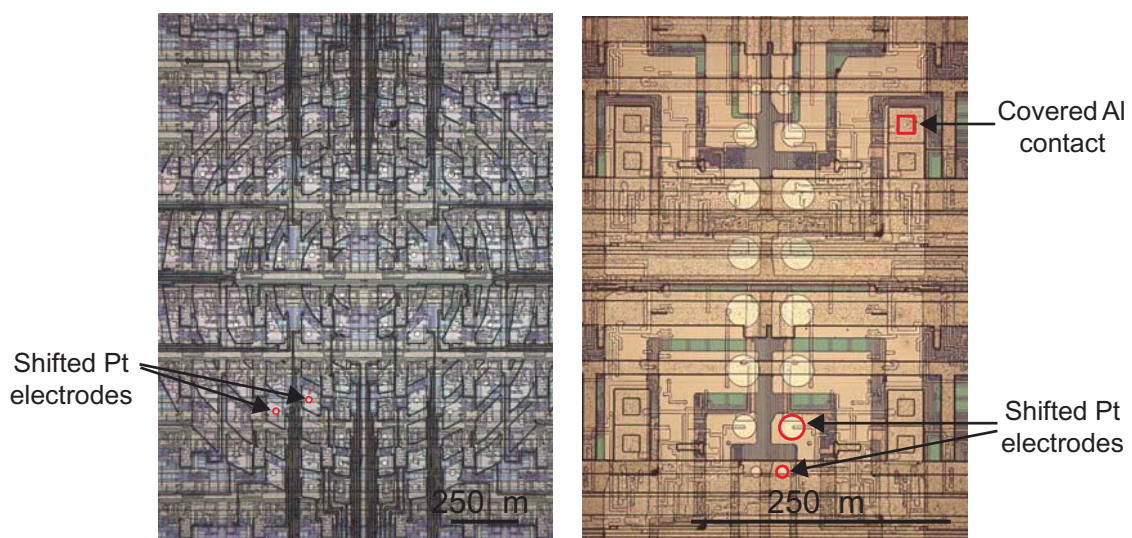


*Fig. 3.5: Variations of the shifted-electrode design. All the electrode can be clustered into the center of the chip (left, courtesy of Agabi Oshioyena), or small clusters, with electrodes of varying sizes ( $10\ \mu\text{m}$ ,  $20\ \mu\text{m}$  and  $30\ \mu\text{m}$  diameter, right), may be formed.*

### 3.1.3 STABILITY UNDER CULTURING CONDITIONS

It was experimentally determined that a thick, multi-layered passivation stack was required to adequately seal the Al. This is in part due to the roughness of the Al from the CMOS process, visible in the atomic force microscopy (AFM) images of an Al contact shown in Fig. 3.6. For a  $20\ \mu\text{m} \times 20\ \mu\text{m}$  area, the average roughness, Ra, was found to be 37 nm.

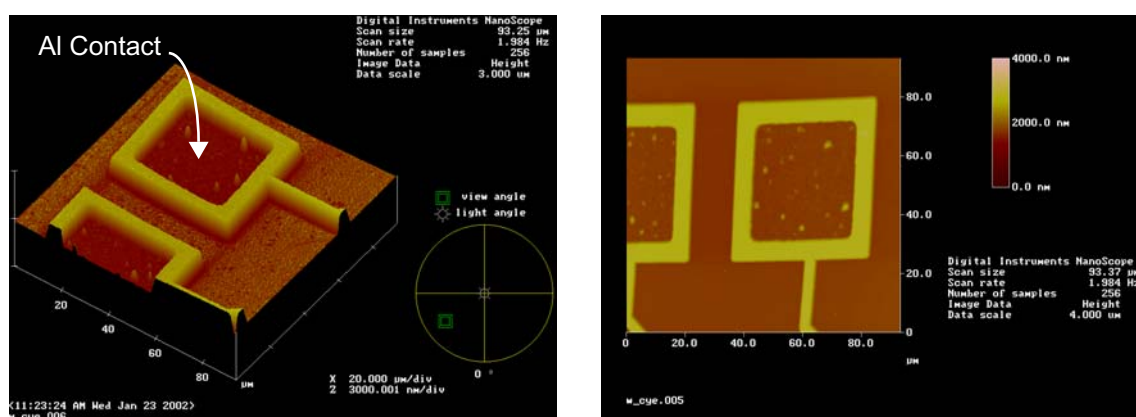


*Fig. 3.6: AFM images showing a 3-D view of an Al contact (left), with height scale (right). Large surface features are visible in both images.*

When only a 1.0- $\mu\text{m}$ -thick layer of  $\text{Si}_3\text{N}_4$  was used to cover the Al areas of the chip, the Al dissolved after only four days of culturing, see Fig. 3.7<sup>1</sup>. Using the alternating-stack configuration, it was found that the Al was stable for 200 DIV.

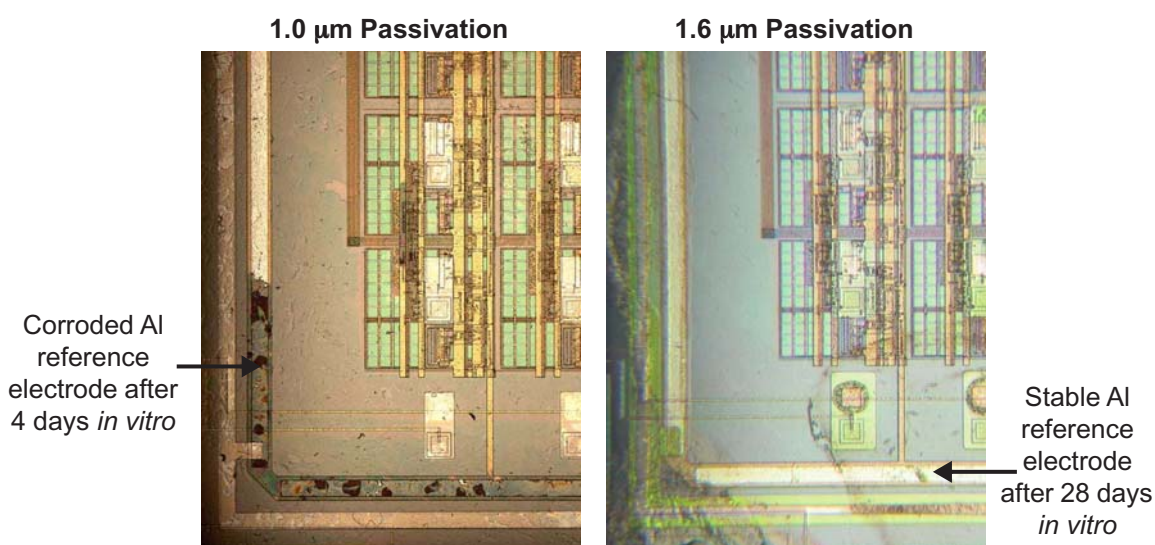


*Fig. 3.7: Corroded Al (left): when a 1.0- $\mu\text{m}$ -thick  $\text{Si}_3\text{N}_4$  layer was used, the Al reference electrode dissolved after only 4 days in vitro (DIV). The reference electrode is not attacked (right) after 28 DIV when the 1.6  $\mu\text{m}$  stack of alternating  $\text{SiO}_2$  and  $\text{Si}_3\text{N}_4$  passivation is used.*

1. Culturing was kindly performed by Axel Blau at the University of Kaiserslautern, Germany.



It is believed that any dust or sharp irregularities in the surface topography will lead to pinhole formation during the PECVD deposition. A simplified representation of the PECVD process in the presence of gross surface topographies is shown in Fig. 3.8 [Sze, 1988]. Sharp surface structures impede the arrangement of impinging vapor particulate, resulting in a pinhole. It is believed that the passivation does not simply fill around the surface irregularity because it is not thermodynamically favorable to form an interface between dissimilar materials (in this case Al, or dust, and  $\text{Si}_3\text{N}_4$ ). No matter how thick the layer is, the pinhole will persist. Multiple passivation layers are deposited to reduce the probability of pinholes aligning through the entire passivation stack.

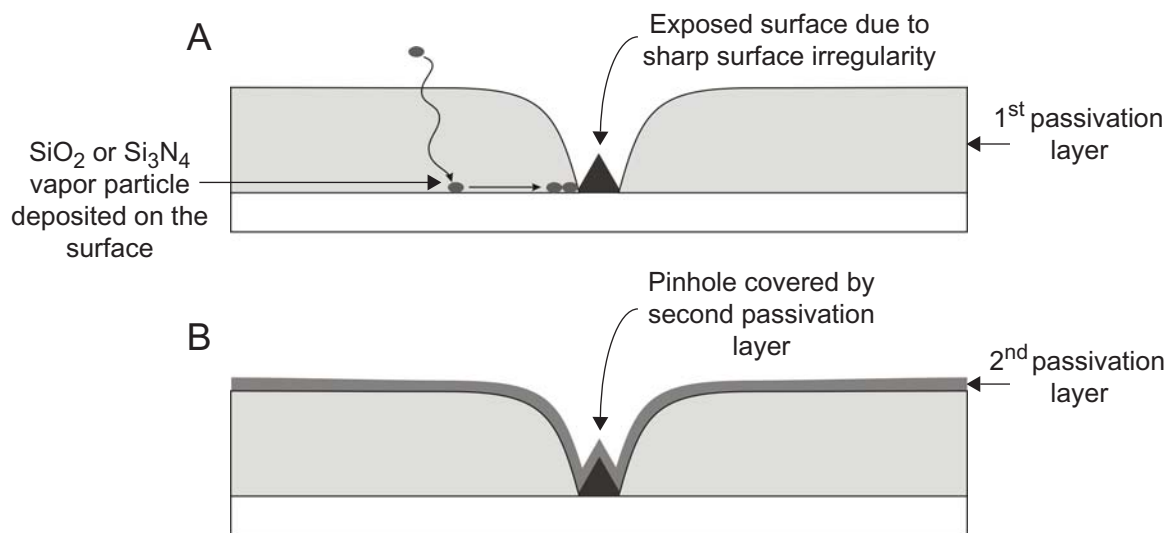


*Fig. 3.8: Schematic of the PECVD process in the presence of large surface irregularities [Sze, 1988]. In A, the deposited particles migrate on the substrate surface, but stop at the side wall of a sharp feature. A pinhole will persist, regardless of the passivation thickness. A second passivation layer is required to cover the exposed surface (B).*

## 3.2 PACKAGING

Packaging plays a key technological role in this work, due to the complicated nature of contacting the CMOS chip both electrically and physically with a wet cell culture environment. The packaging scheme is depicted in Fig. 3.9. The chip is first wire-bonded to a ceramic package. Bond pads and wires must then be encapsulated. The encapsulant must satisfy two criteria: the Al bond pads and

bond wires must be protected from the culture medium and the packaging itself must be compatible with the cell culture bath, if not forming the bath itself. A simple two-step encapsulant strategy was used where the bond wires were first encapsulated in an epoxy, such as MasterBond 42HT-T (Master Bond Inc., USA) or Epo-Tek 353ND (Epoxy Technology, USA). PDMS and a glass o-ring were then used to form the culture bath, see Fig. 3.10 for a photograph of the final package.

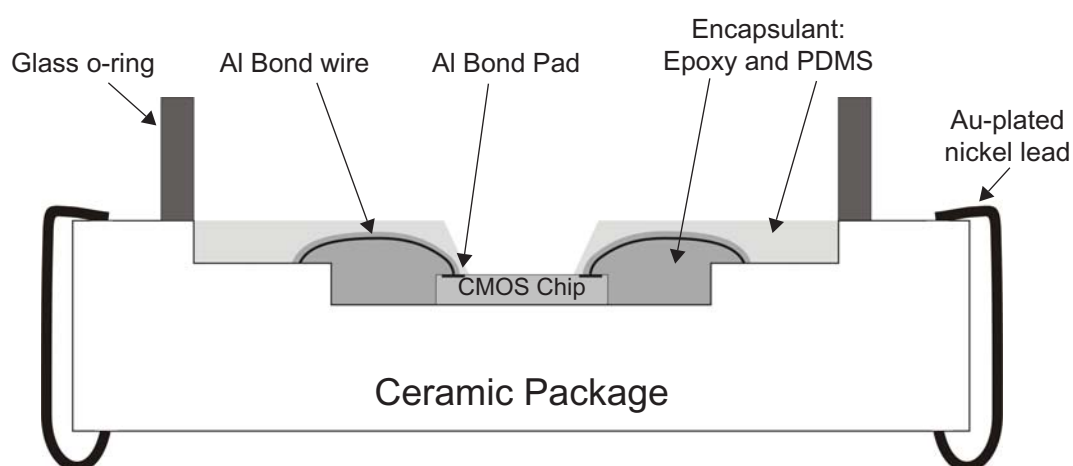


*Fig. 3.9: Cross-section schematic of the wire-bonded and packaged CMOS chip. The active area of the CMOS chip, where the electrodes are located, is exposed to the cell culture, while the bond wires and pads are not. Epoxy and PDMS is used to encapsulate the bond wires and form the culture bath. A glass o-ring is used to expand the culture bath. All the metal surfaces of the ceramic package are nickel plated with 150  $\mu\text{m}$  of Au.*

Although the packaging appears to be simple, it was not without technological issues. For example, PDMS alone cannot be used as the encapsulant, since it is porous, leading to contact between the bond wires and the medium. This situation compromises electrical isolation and, more importantly, material stability. In fact, when a PDMS-only scheme was tested, the bond wires were completely corroded leaving behind empty tunnels in the PDMS. Furthermore, swelling of the PDMS lifted the bond wires away from the bondpads resulting in broken connections. The epoxy must be selected not only for biocompatibility and electrical isolation, but also for adhesion to the CMOS chip. If the epoxy does not adhere well to the surface of the chip, liquid may flow between the epoxy and chip, lead-

ing to bond pad corrosion. Other options, such as the use of non-porous PDMS, or bond wire and pad protection with a thin layer of conformal, water-proof parylene may be used for enhanced long-term stability. To date, electrophysiological measurements have been made at 55 DIV.

This packaging scheme was designed to demonstrate proof of concept and is not without drawbacks. It is time consuming, costly (the ceramic packages cost USD 25.00 each) and does not allow for integration with microfluidics. Parallel packaging schemes, such as flip-chip packaging with integrated microfluidics, would be an elegant, albeit technically challenging, solution.

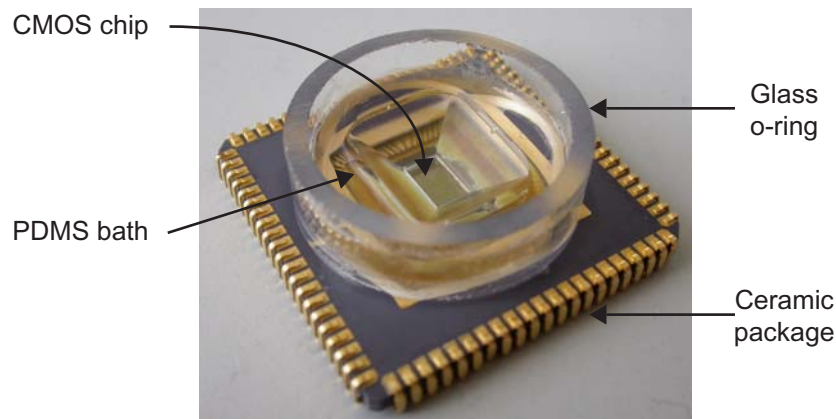


*Fig. 3.10: Image of the packaged CMOS chip. Photo credit: Flavio Heer.*

### 3.3 IMPEDANCE MEASUREMENTS

The impedance model based on electrochemical impedance spectroscopy (EIS) was initially developed to characterize the electrode-electrolyte interface for bright Pt, Pt black and TiN (see Appendix A for complete model details and results). The model was further used to evaluate a gold-nanowire material, with 5 different wire dimensions, for potential use as the electrode material. Experimental conditions for the EIS nanowire recordings are similar to those described in Appendix A, and are given in Tab. 3.1. Fig 3.11 shows the Bode plots for the 5 different nanowires, generated using the fitted parameters listed in the inset table. Under the assumption that the constant phase angle impedance represents the impedance due to the interface capacitance, or  $|Z_{CPA}| = |Z_{C_i}|$ , it follows that  $C_i = Q^n$  for  $\omega = 1 \text{ s}^{-1}$  (where  $C_i$  is the interface capacitance,  $Q$  is a measure of

the magnitude of  $Z_{CPA}$ ,  $n$  is a constant ( $0 \leq n \leq 1$ ), and  $\omega$  is the angular frequency). For comparison purposes,  $Q^n$  is included in Fig 3.11, although it has been assigned arbitrary units as a reminder that  $Q^n$  is not exactly equal to  $C_T$ . Recall that, in the ideal case, the total electrode interface capacitance is large, to dampen the effects of noise, while allowing the geometric area of the electrode to shrink for high spatial-resolution recordings. Therefore, the best nanowire material is **A**, which has the largest value for  $Q^n$ .

*Tab. 3.1: Experimental parameters for EIS Au nanowire measurements*

<b>Parameter</b>	<b>Value</b>
<b>Measurement area [mm<sup>2</sup>]</b>	15
<b>Electrolyte</b>	0.9 % NaCl
<b>Perturbation Voltage [mV]</b>	10
<b>Frequency Scan Range [Hz]</b>	$10^{-2}$ - $10^5$

Since impedance is a function of both area and frequency, any valid comparison takes both these variables into consideration. Bode plots for the materials under consideration (bright Pt, bright Au, Au nanowire and Pt black) based on a 30  $\mu\text{m}$  diameter spherical electrode (total geometric area 700  $\mu\text{m}^2$ ) are shown in Fig. 3.12. The bode plots were generated from model parameter values that were scaled by area. For bright Pt and Pt black the fitted parameters determined from the 1  $\text{cm}^2$  measurements presented in Appendix A were used. In the case of the gold nanowire, the parameters from material **A** (inset, Fig 3.11), were used. Note that the parameters presented in Fig. 3.11 are for a 15  $\text{mm}^2$  measurement area; while those in Appendix A are for an area of 1  $\text{cm}^2$ . Fig. 3.12 clearly shows that Pt black has the lowest impedance and is therefore the best electrode material. An interesting observation is that the electrode impedance is predominately capacitive, the phase angle is almost  $-90^\circ$ , over the expected measurement frequency range, from 10 - 5 kHz. This satisfies the design criteria that the interface be capacitive to avoid redox reactions, the products of which may be harmful to the cell culture.

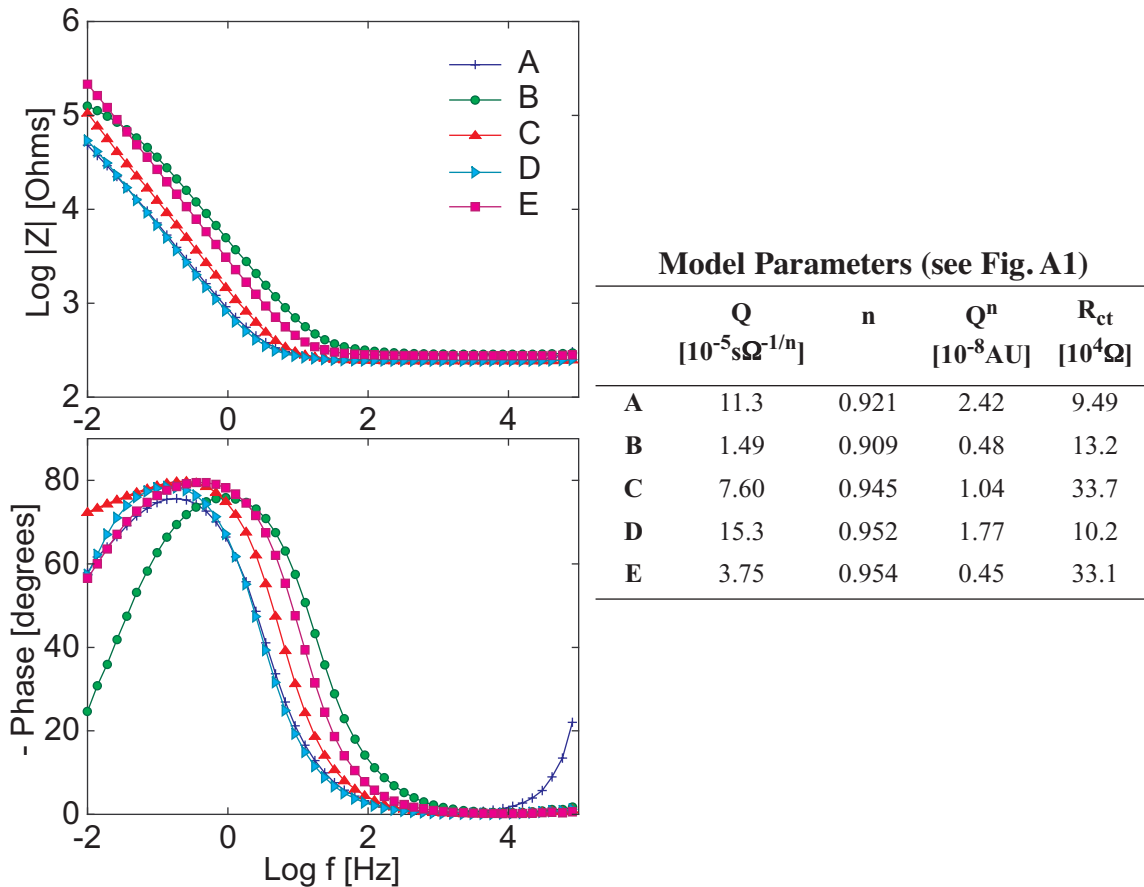


Fig. 3.11: Bode plots for the nanowires with varying dimensions (measurement area 15 mm<sup>2</sup>). The table gives the EIS model parameters. The solution resistance for all materials has an average value of 260 Ω.

Finally, to analyze the accuracy of scaling fitted parameters, bode plots generated from parameter values determined experimentally versus parameter values that were scaled are presented in Fig. 3.13. The plots on the left side, 900 μm<sup>2</sup> Pt black, show the worst case scenario where the generated plots differ greatly. This is potentially due to the small measurement area. As the electrode size shrinks, the current that must be measured for impedance testing becomes too small to measure accurately. Alternatively, the discrepancy is an effect of non-uniform platinization, as discussed below. Plots on the right side of Fig 3.13, 9 mm<sup>2</sup> bright Pt, coincide nicely with one another. A recommendation from this discussion is that large-area impedance measurements should be performed, and the parameter values scaled for improved accuracy. Nevertheless, small-area recordings are not without merit. Some structured surfaces, such as Pt black, may not be homogeneous over small areas leading to highly variable recordings, with

respect to impedance (for example those presented in Appendix A), and activity from electrogenic cells. In this case, impedance measurements would help to identify these inconsistencies and may be a valuable tool in optimizing the surface structuring.

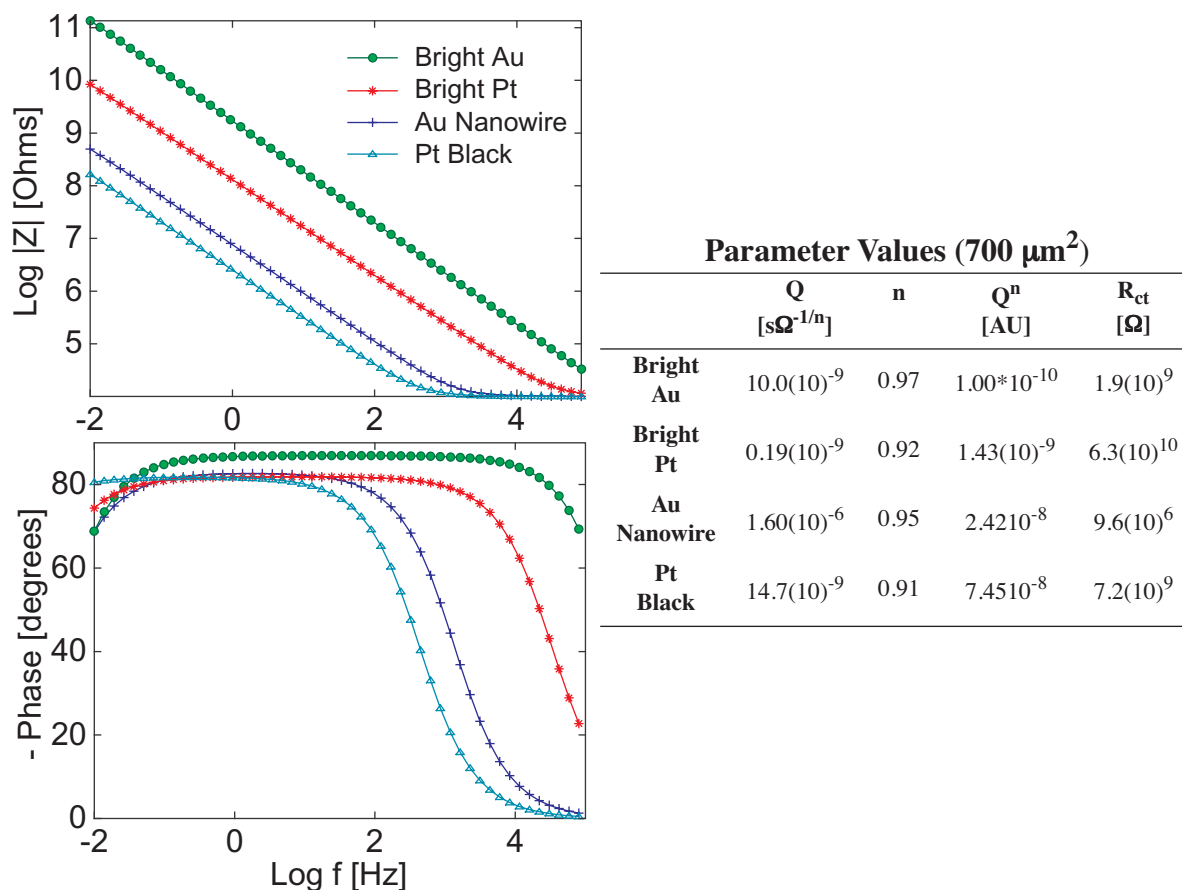


Fig. 3.12: Bode plots generated from scaled parameter values (see table) for a  $30 \mu\text{m}$ -diameter spherical electrode. In all cases a solution resistance,  $R_s$ , of  $10^4 \Omega$ , calculated using Eq. A8, was used.

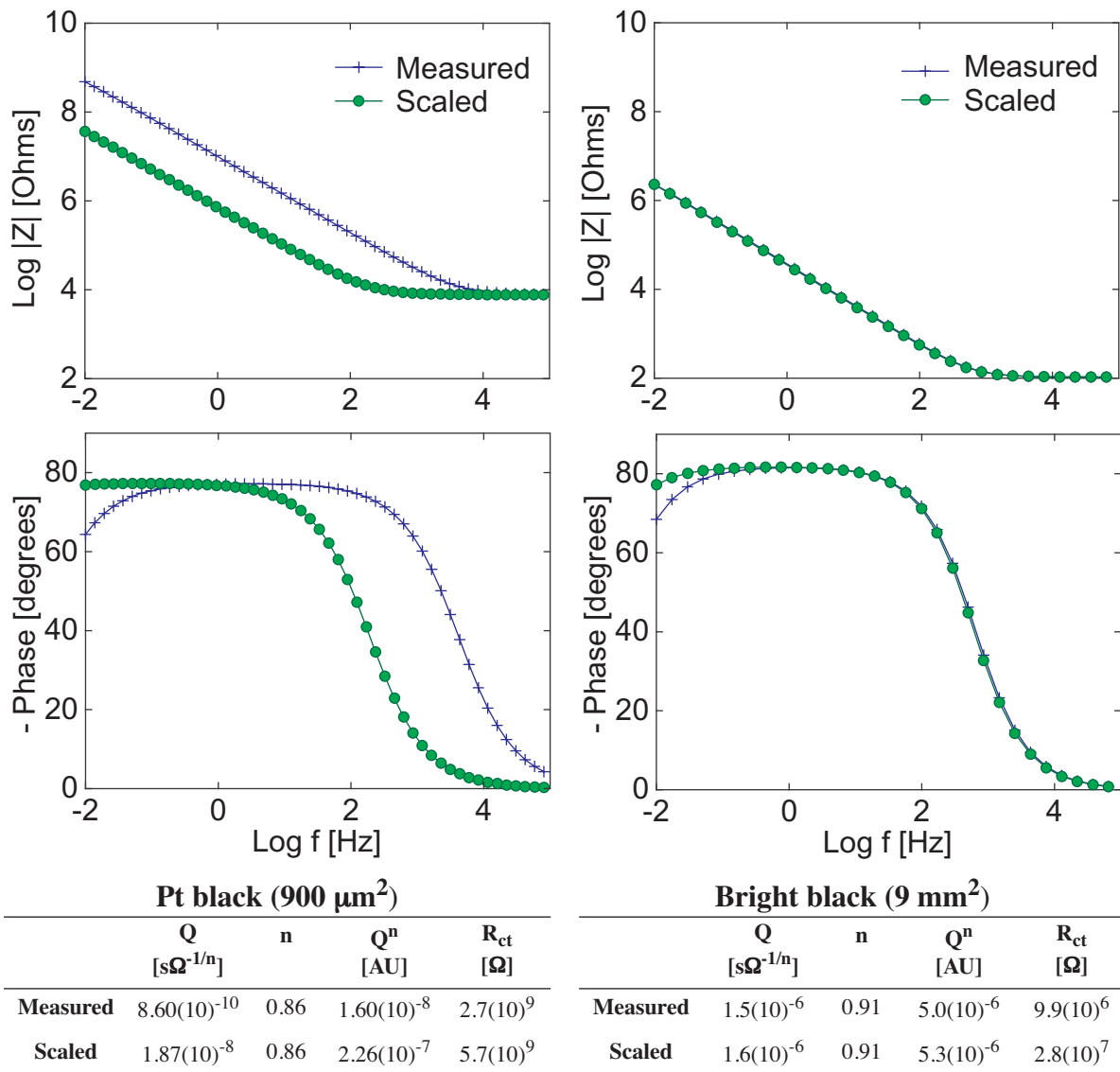


Fig. 3.13: The effects of scaling the fitted parameters. Bode plots generated from experimentally determined parameters and parameters whose values have been scaled accordingly to represent a smaller electrode area. In the worst case (left), the generated bode plots differ by an order of magnitude; in the best case (right), the curves closely match one another. The parameter values are given in the tables.

### 3.4 CARDIOMYOCYTE CELL CULTURING

Cardiomyocytes were selected as an optimal vehicle for system development and research for several reasons. Firstly, they are an ideal tool for testing and developing the CMOS chip because they illicit large signals (100 mV, see Tab. 2.2) and the beating can be seen under a microscope. Once it is established that the cells are indeed beating, electrophysiological experiments may be attempted. Visual confirmation of electric activity is an advantage over other cell types, such as neurons, where one cannot know for certain if the cells are active. If signals are not recorded it is not clear whether the problem lies with the ‘wet-ware’ or the hardware. Secondly, that an electrically active, immortalized cell line is available (see Tab. 2.2) greatly improves experiment flexibility. A supply of cells may be frozen and thawed, as required, and animal sacrifice is avoided. Thirdly, they provide an interesting pharmacological research tool. For example, *torsade de pointes*, or arrhythmic cardiac activity, has been associated with the blocking of the hERG K<sup>+</sup> channel [Redfern *et al.*, 2003]. The American Food and Drug Administration has recently regulated that each submitted drug candidates may not affect the K<sup>+</sup> channel (see Sec. 1.1). A tool that provides information about pharmacological effect of a drug on the cardiac myocyte electrophysiology may be useful in the drug development process.

Two types of cardiomyocytes were used in this work: the HL-1 cell line and neonatal rat cardiomyocytes (NRCs). The HL-1 cell line was derived from the AT-1 mouse atrial cardiomyocyte tumor lineage [Claycomb *et al.*, 1998, White *et al.*, 2004]. While both the AT-1 and HL-1 cell lines have the ability to contract and retain differentiated cardiac morphological, biochemical and electrophysiological properties, only the HL-1 cell line can be serially passaged and recovered from frozen stocks. The culturing details for the HL-1 cell line, including the components of the required Claycomb Medium<sup>®</sup>, are given in Appendix C. These cells were primarily used to develop the engineered surfaces for patterned cell adhesion, presented in Appendix C and Section 4.2. The HL-1 cell line was generously provided by Dr. Claycomb at the Louisiana State University Health Sciences Center.

The NRCs were dispersed from the ventricles of 1-3-day-old Sprague-Dawley rats by digestion with collagenase II (Worthington Biochemical Corp., U.S.A.) and pancreatin (Sigma-Aldrich, U.S.A.). To obtain cultures comprising more than 95% cardiomyocytes, the cell suspensions were separated on a discontinu-



ous Percoll gradient [Sen *et al.*, 1988]. Details on the culture medium are given in Appendix C and in Auerbach *et al.*, 1999. The NRCs were used to demonstrate that the patterned surface does not affect cell differentiation with respect to myofibrillogenesis, the formation of muscle microstructure, and for electrophysiological recordings (for system development as mentioned above). They were generously provided by Evelyne and Jean-Claude Perriard, Department of Cell Biology, ETHZ.

Although electrophysiological recordings with neural cell cultures are also presented in this thesis, culturing details are presented in Appendix D. In this case, culturing was performed either at the University of Kaiserslautern or at the Scuola Superiore di Studi Avanzati (SISSA).

### 3.5 SUMMARY AND CONCLUSIONS

In this chapter, the experimental methods contributing to the design and realization of the CBB were presented. One particularly challenging aspect of this work was the post-processing and packaging. Once the alternating stack of silicon dioxide and nitride was used, chip stability under culture conditions improved dramatically – from less than 4 DIV to 200. The shifted-electrode design affords a great deal of flexibility with respect to electrode material, size, shape and location. A simple, yet effective, packaging scheme was presented. The CMOS chip was wire bonded to a ceramic package and encapsulated with epoxy and PDMS. Although this is a successful packaging method, it is time consuming and expensive. It would be worthwhile to investigate alternative packaging approaches that are faster and have the capability to integrate microfluidics.

In the third chapter section, an impedance-based evaluation of candidate electrode materials: bright Pt, Pt black, bright Au and nanostructured Au, was presented. It was found that Pt black has the lowest impedance, after nanostructured gold. In some cases, it may be advantageous to use high-area gold since it can be functionalized with a self-assembled monolayer. However, to use the nanostructured gold with the CMOS chip would require several technically complex processing stages, not the least of which would be to determine a way to achieve small-area electrodes. One possible solution would be to use a nano-pore sieve rather than the alumina template. Additionally, the model was used to demonstrate that the electrode-electrolyte interface impedance is predominately capaci-

tive over the measurement range of 1 Hz to 5 kHz. This is an important finding that helps to define the measurement conditions.

## 3.6 REFERENCES

Auerbach, D., Bantle, S., Keller, S., Hinderling, V., Leu, M., Ehler, E., and Perriard, J. C. (1999). "Different domains of the M-band protein myomesin are involved in myosin binding and M-band targeting." *Mol Biol Cell*, 10(5), 1297-308.

Borkholder, D. A. (1998). "Cell based biosensors using microelectrodes," Stanford University.

Claycomb, W. C., Lanson, N. A., Jr., Stallworth, B. S., Egeland, D. B., Delcarpio, J. B., Bahinski, A., and Izzo, N. J., Jr. (1998). "HL-1 cells: a cardiac muscle cell line that contracts and retains phenotypic characteristics of the adult cardiomyocyte." *Proc. Natl Acad Sci U S A*, 95(6), 2979-84.

Feltham, A. M., and Spiro, M. (1971). "Platinized Platinum Electrodes." *Chemical Reviews*, 71(2), 177-&.

Forrer, P., Schlottig, F., Siegenthaler, H., and Textor, M. (2000). "Electrochemical preparation and surface properties of gold nanowire arrays formed by the template technique." *Journal-of-Applied-Electrochemistry*, 30(5), 533-41.

Gesteland, R. C., Howland, B., Lettvin, J. Y., and Pitts, W. H. (1959). "Comments on Microelectrodes." *Proceedings of the Institute of Radio Engineers*, 47(11), 1856-1862.

Janders, M., Egert, U., Stelzle, M., and Nisch, W. "Novel thin film titanium nitride micro-electrodes with excellent charge transfer capability for cell stimulation and sensing applications." *Proceedings of 18th Annual International Conference of the IEEE Engineering in Medicine and Biology Society*, Amsterdam, Netherlands, 245-247.

Lehmann, M., Baumann, W., Brischwein, M., Gahle, H. J., Freund, I., Ehret, R., Drechsler, S., Palzer, H., Kleintges, M., Sieben, U., and Wolf, B. (2001). "Simultaneous measurement of cellular respiration and acidification with a single CMOS ISFET." *Biosensors & Bioelectronics*, 16(3), 195-203.

- Maher, M. P., Pine, J., Wright, J., and Yu Chong, T. (1999). "The neurochip: A new multielectrode device for stimulating and recording from cultured neurons." *Journal of Neuroscience Methods*, 87(1), 45-56.
- Redfern, W. S., Carlsson, L., Davis, A. S., Lynch, W. G., MacKenzie, I., Palethorpe, S., Siegl, P. K., Strang, I., Sullivan, A. T., Wallis, R., Camm, A. J., and Hammond, T. G. (2003). "Relationships between preclinical cardiac electrophysiology, clinical QT interval prolongation and torsade de pointes for a broad range of drugs: evidence for a provisional safety margin in drug development." *Cardiovasc Res*, 58(1), 32-45.
- Sen, A., Dunnmon, P., Henderson, S. A., Gerard, R. D., and Chien, K. R. (1988). "Terminally differentiated neonatal rat myocardial cells proliferate and maintain specific differentiated functions following expression of SV40 large T antigen." *J Biol Chem*, 263(35), 19132-6.
- Stenger, D. A., McKenna, T. M. (1994). *Enabling Technologies for Cultured Neural Networks*, Academic Press, London.
- Sze, S. M. (1988). *VLSI Technology*, McGraw-Hill Book Company, London.
- Trapp, O. D., Blanchard, R. A., Lopp, L. J., Kamins, T. I. (1985). *Semiconductor Technology Handbook*, Bofors Inc., San Mateo.
- Tykocinski, M., Duan, Y., Tabor, B., and Cowan, R. S. (2001). "Chronic electrical stimulation of the auditory nerve using high surface area (HiQ) platinum electrodes." *Hear Res*, 159(1-2), 53-68.
- Weiland, J. D., Anderson, D. J., and Humayun, M. S. (2002). "*In vitro* electrical properties for iridium oxide versus titanium nitride stimulating electrodes." *IEEE Trans Biomed Eng*, 49(12 Pt 2), 1574-9.
- White, S. M., Constantin, P. E., and Claycomb, W. C. (2004). "Cardiac physiology at the cellular level: use of cultured HL-1 cardiomyocytes for studies of cardiac muscle cell structure and function." *Am J Physiol Heart Circ Physiol*, 286(3), H823-9.



---

# 4 PATTERNED CELL ADHESION

The ability to precisely confine cell attachment to specific regions has long been a design goal of fundamental cell biology studies, tissue engineering, and, more recently, biosensor fabrication [Kane *et al.*, 1999, Jung *et al.*, 2001]. In basic neuroscience, patterns are used to generate defined networks of neurons to be used to study development and computation within the neural network [Kleinfeld *et al.*, 1988, Wyart *et al.*, 2002]. Although patterned neurochips are still in the embryonic stages of development, and the type of information that can be derived from *in vitro* studies is not fully established (see Fig. 2.16), this is nevertheless a compelling research niche. The applicability of patterned cell cultures for pharmacological studies is better defined. A device where the electrical signal flows through discrete cell strands, independent from one another, can be used to simultaneously perform multiple screenings while all other environmental conditions are kept constant. A third application area is basic cardiology. Signal propagation through a syncytium (a continuous carpet of cells) of cardiomyocytes can be highly non-uniform. Reducing signal propagation to a one-dimensional path helps to simplify analysis [Rohr *et al.*, 1991, Thomas *et al.*, 2000, Kleber and Rudy, 2004].

This chapter opens with an overview of the wide range of patterning strategies published in literature, namely: microcontact stamping, ink jet printing, photolithography, selective molecular assembly patterning (SMAP, the technique used in this work), microfluidics, physical immobilization and real-time manipulation. The key features of each technique are summarized in Tab. 4.1. The method for patterning dissociated cell cultures used in this work, including process steps, characterization and results with cardiac myocytes, is then presented. In certain situations, it may be advantageous to generate a pattern of specific protein molecule, such as laminin to promote neural adhesion. A preliminary experiment was performed to demonstrate that the functionalized surface can be used to pattern adhesion-mediating proteins. Finally, results from an initial patterning attempt with hippocampal rat neurons are shown.

## 4.1 PATTERNED CELL ADHESION

Physicochemical<sup>1</sup> and topographical features are used to control not only cell location, but also phenotypic and genotypic cell attributes [Jung *et al.*, 2001]. It is well known in biology that the environment surrounding the cell, the extracellular matrix (ECM), can have a profound effect on the internal functioning of the cell [Alberts *et al.*, 1994]. When working *in vitro* it is important to realize that the surface presented to the cell may significantly alter cellular operations. With respect to the discussion here on a cell-based biosensor as a tool to study the pharmacological effect of a compound, care must be taken to identify the differences between the *in vitro* and *in vivo* cell. Therefore, biomimically inspired adhesion compounds, such as laminin or fibronectin (or fragments thereof), which are naturally present in the ECM, are commonly used as an adhesion-promoting mediator.

### 4.1.1 REVIEW OF CONTROLLED CELL ADHESION STRATEGIES

The desired characteristics of an engineered surface for patterned adhesion include: biocompatibility, high-contrast adhesion, facile processing, compatibility with other technologies (CMOS, microfluidics), high resolution, flexibility (to tailor surface composition to cell type), long-term stability, reusability and, last but by no means least, cost. No single patterning method possesses all of these qualities; nonetheless, several methods have found wide-spread application. The most commonly used technique is micro-contact stamping, which is extremely simple, inexpensive, and flexible with respect to choice of patterning chemicals. As an alternative, ink-jet printing offers ease of use, flexibility and low costs, although nanometer-sized structures are presently not achievable. The technique used in this work, selective molecular assembly patterning (SMAP), leverages specific adsorption interactions to form patterns of high-contrast pattern adsorption. High-resolution patterns self-align to a pre-patterned substrate. Other methods include photolithographic techniques, microfluidic channels, and physical immobilization. A description of each of these techniques follows, and a summary is given in Table 4.1.

- 
1. Following the nomenclature in Jung *et al.*, 2001, the term *physicochemical* is used because it alludes to the wide spectrum of both physical and chemical phenomena that mediate cell-surface interactions. Where physical interactions are electromagnetic and van der Waals or dispersion forces, chemical interactions refer to covalent, ionic and hydrogen bonding.

The various patterning schemes can be divided into two categories: those based on chemical cues and those based on physical cues. Techniques based on chemical cues have the basic structure shown in Fig 4.1. To generate the pattern, adhesion-promoting (R and P in Fig. 4.1) and adhesion-inhibiting (R' in Fig. 4.1) moieties are immobilized on the substrate [Kane *et al.*, 2001]. Adhesion-promoting molecules are attached to the surface either via a thiol bond, as is the case for a self-assembled monolayer (SAM), or via a silane bond (denoted by X in Fig. 4.1). In general, cells adhere to a surface via an interfacing protein; hence patterned regions are chemically tuned to control protein adhesion. This is accomplished in one of two ways, denoted A and B in Fig. 4.1. In case A, the functional group R, such as  $\text{CH}_3$  or  $\text{NH}_3^+$ , mediates protein adhesion. The patterned surface is exposed to a solution containing the adhesion-mediating protein, denoted by P in the figure. In an example of biomimicry, case B, R may be a moiety that directly mediates cell adhesion. For example, a peptide known to support cell adhesion, such as the RGD motif (see section 2.2), may be used. Finally, for high-contrast patterns a second, protein-repellent molecule, R', is immobilized on the surface. In most cases R' is Poly(ethylene glycol) [Prime and Whitesides, 1991].

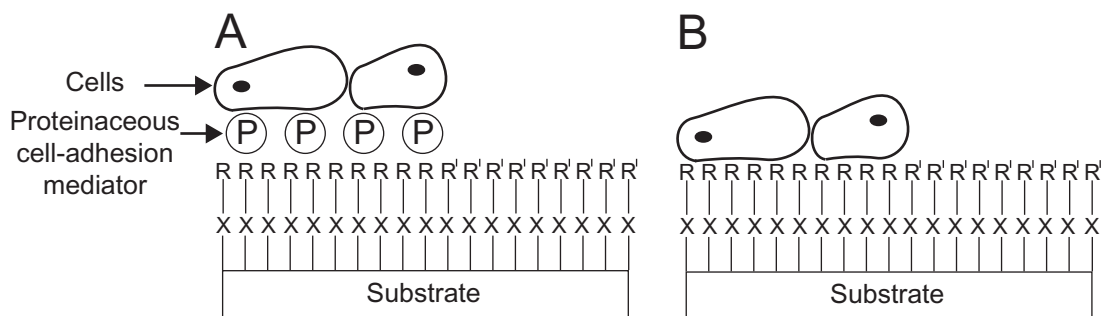
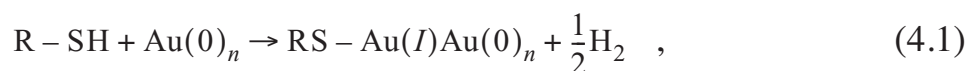


*Fig. 4.1: Schematic showing general schemes for cell adhesion patterning based on chemical cues. The molecules are attached to the substrate via a thiol or silane bond, denoted by X. The functional groups R and R' either promote ( $R = \text{CH}_3$  or  $\text{NH}_3^+$ ) or inhibit ( $R' = \text{OH}(\text{CH}_2\text{CH}_2\text{O})_n$ ) protein and/or cell immobilization. In A, cell adhesion is mediated by an intermediate protein layer, denoted by (P). In B, R mediates cell adhesion directly. For example, a peptide known to promote cell adhesion (e.g. RGD, see section 2.2) may be used.*

Techniques based on physical cues use three-dimensional structures to manipulate cell location, such as cages and fences, or grooved patterns and engineered surface roughness.

### MICROCONTACT STAMPING

Arguably the most common patterning technique, microcontact stamping, or soft lithography, is an easily accessed procedure because, for medium-resolution patterns ( $> 20 \mu\text{m}$ ), no cleanroom is required (an excellent review is given in Kane *et al.*, 1999). Devised in the group of George Whitesides at Harvard University, the technique involves casting an elastomer, typically poly(dimethylsiloxane) (PDMS), against a master. The master is made from a silicon substrate with photoresist structures forming a relief pattern. A shadow mask is used to selectively expose and harden the photoresist structures. If the structure feature size is larger than  $20 \mu\text{m}$ , then the shadow mask can be made using a high-quality laser printer, thereby obviating the need for a cleanroom. To control protein adhesion, the well-known gold-thiol chemistry is used to form SAM's according to the following reaction:



where  $R$  is a functional group used to tune the relative adsorption of proteins to the surface (the roman numerals in the brackets refer to the oxidation state of gold). To form the adhesion pattern, the stamp is inked with a solution of an alkanethiol and brought in conformal contact with the substrate. The surface is then exposed to a solution containing a second alkanethiol, with a protein-repellent end group. The SAM binds to the remaining bare-gold surface creating a high-contrast protein adhesion pattern. For areas of cell adhesion, methyl groups are used, and oligo(ethylene glycol),  $\text{R}' = (\text{CH}_2)_{11}(\text{OCH}_2\text{CH}_2)_3\text{OH}$ , groups are used as an inhibitory background. Immersion of the patterned surfaces in solutions containing proteins such as fibronectin, fibrinogen, pyruvate kinases, steptavidin and immunoglobins, resulted in adhesion at the methyl groups only [Lopez *et al.*, 1993]. Subsequent plating with bovine capillary endothelial cells yielded cells adhering to the patterned proteins only [Mrksich *et al.*, 1997]. In a more complicated scheme, the synthetic peptide PA22-2, known to mimic laminin, is printed on a surface pre-functionalized with an aminosilane, an anchored intermediary crosslinker [Scholl *et al.*, 2000]. In an alternative scheme, the protein



themselves are stamped [Benard *et al.*, 1998]. Although the amount of deposited protein is similar to that adsorbed from solution, protein function is compromised due to the non-solution environment inevitable with micro-contact stamping.

### **INK JET PRINTING**

High flexibility in pattern design is achievable when an ink jet printer is used to 'write' chemical patterns [Klebe *et al.*, 1988, Turcu *et al.*, 2003, Sanjana and Fuller, 2004]. The printer cartridge is modified to dispense small volumes of adhesion mediators, for example, laminin solution (Turcu *et al.*) or collagen/poly-D-lysine (Sanjana and Fuller). Substrates pre-functionalized with poly(ethylene glycol) (PEG) are used. The advantage of this method is that the pattern is stored in a digital format and can be easily altered.

### **PHOTOLITHOGRAPHIC TECHNIQUES**

For sub-micron-resolution patterns, photolithographic techniques have been developed. In general, photoresist is used either as a protective mask, or as a sacrificial layer in a lift-off procedure, to pattern organic molecules. In one of the original schemes developed by Kleinfeld and coworkers, photoresist is used as a mask while alkyltrichlorosilane is fluxed over the surface defining regions of cell inhibition ( $X-R' = \text{Si}(\text{CH}_2)_{13}\text{CH}_3$  in Fig. 4.1, Kleinfeld *et al.*, 1988). Once the photoresist is removed, the surface is exposed to amine derivatives that bind to the unexposed areas ( $X-R = \text{Si}(\text{CH}_2)_3\text{NH}_2^+\text{CH}_2\text{CH}_2\text{NH}_3^+$  in Fig. 4.1 B). Relevant to this work is the finding that embryonic mouse spinal cells and perinatal rat cerebellar cells preferentially attached and developed at surfaces of bound diamines and triamines. These cells types developed less well on surfaces of monoamines.

In a scheme developed by Wyart and coworkers, photoresist is used as a mask to selectively etch away hydrophobic fluorosilane [Wyart *et al.*, 2002]. Poly-L-lysine was subsequently adsorbed to the etched areas defining sites of cell adhesion. Another group working at the Paul Scherrer Institute, Switzerland, used both lift-off and plasma etching techniques to pattern layers of covalently immobilized proteins [Sorribas *et al.*, 2002]. In a scheme developed by Ruehe and co-workers, photoreactive intermediary crosslinkers were used to covalently immobilize polymeric molecules. The polymers are bound to the intermediary upon exposure to UV radiation, thus allowing for the transfer of high-resolution patterns [Ruehe *et al.*, 1999, Prucker *et al.*, 1999]. With this technique it was

shown that the rat cerebellum cells adhered best to poly(methacryoyl oxypropyl(trimethyl ammonium) bromide), a material that is positively charged in neutral solutions.

A promising new micropatterning technique has recently been developed by the BioInterfaces group at the ETH, Switzerland. Termed molecular assembly patterning by lift-off (MAPL), this method yields high-contrast cell adhesion and long-term pattern fidelity [Falconnet *et al.*, 2004, Falconnet 2005]. Niobium oxide surfaces are functionalized with poly(L-lysine)-*graft*-poly(ethylene glycol) (PLL-*g*-PEG) and PLL-*g*-PEG/PEG-X, where X is a bioactive molecule such as biotin. Photoresist is patterned and the wafer is exposed to a solution containing the PLL-*g*-PEG/PEG-X. The photoresist removal process, incorporating an organic solvent and sonication, does not harm the adlayer and suitably prepares the surface for the next step, the adsorption of PLL-*g*-PEG.

### **SELECTIVE MOLECULAR ASSEMBLY PATTERNING (SMAP)**

The SMAP process yields high-contrast, high-resolution protein patterns. It is based on a combination of a photolithographically structured substrate and selective self-assembly of organic molecules. Once the substrate is structured, functionalization is achieved in a simple dip-and-rinse process. It was originally developed for a system of SiO<sub>2</sub>/TiO<sub>2</sub> surfaces [Michel *et al.*, 2002, Lussi *et al.*, 2004]. The substrate is first exposed to a solution containing an alkane phosphate, which selectively assembles on the TiO<sub>2</sub>, forming the regions of protein adhesion. The substrate is subsequently exposed to a solution of PLL-*g*-PEG, which adsorbs to the areas of SiO<sub>2</sub>. The chemistries must be carefully selected to ensure that the desired molecule assembles at appropriate surface and does not disrupt previously assembled molecules. An advantage of this system is that it is self-aligning; molecules assemble at pre-defined surfaces only. In this thesis, the SMAP method was extended to functionalize surfaces of Au and SiO<sub>2</sub>, as discussed in the following section.

### **MICROFLUIDICS**

Micrometer-sized channels are formed over a substrate using an elastomer stamp, such as PDMS or photoresist [Kim *et al.*, 1995, Martinoia *et al.*, 1999, Griscom *et al.*, 2002]. The channels are filled with a solution containing the adhesion molecule, a precursor, or the cells themselves. The microfluidics may be removed and cells are plated over the entire surface. Alternatively, microfluidics with mul-

multiple inlets operated in a laminar flow regime are used to pattern regions within a single channel [Takayama *et al.*, 1999]. In general, microfluidic-patterned surfaces yield high-contrast patterns, if the cells are cultured within the microfluidics themselves; although culturing in small volumes requires a specialized culture regime.

### **PHYSICAL IMMOBILIZATION**

Physical immobilization based on 3D structures are used to manipulate cell location and development. Cages and pillars have been fabricated from silicon wafers and polyimide [Maher *et al.*, 1999, Zeck *et al.*, 2001, Jung *et al.*, 2001, Dowell-Mesfin *et al.*, 2004]. This technique is fairly complicated to realize, cells are known to escape from the immobilizing structures, and low-density cultures without glia cells do not exhibit long-term longevity (survival is 10% after 2 weeks in culture, Maher *et al.*, 1999).

Other groups have investigated nano- and micro-scale surface topographies to manipulate cell growth. Fan and co-workers have determined that surface roughness ( $R_a$ ) of 20 to 50 nm promotes neural adhesion, while roughnesses of less than 10 nm or greater than 70 nm adversely affect neural adhesion [Fan *et al.* 2002]. Britland, McCaig and co-workers have extensively studied the effect of chemical, topographical and electrical (see next section) cues on cell cultures. It was demonstrated that BHK (baby hamster kidney) cells and neurons aligned to aminosilane adhesive tracks with 6  $\mu\text{m}$  grooves, and did respond to sub-micron feature topographies [Britland *et al.*, 1996(A), Britland *et al.*, 1996(B)]. Neurons were found respond to both adhesive and electrical guidance cues [Britland *et al.*, 1996(C)]. In both cases, however, cells responded preferentially to adhesive cues.

### **REAL-TIME MANIPULATION**

An intriguing body of work uses various real-time techniques to influence neural growth *in situ*. One scheme takes advantage of the fact that neurites tend to grow towards the cathode when placed in a weak ( $\sim 10 - 500 \text{ mV/mm}$ ) extracellular electric field [Erskine and McCaig, 1997, Borgens *et al.*, 1999]. Another technique, developed by Kaehr and colleagues, uses multiphoton excitation to photo-crosslink adhesion promoting proteins, which act as physical barriers to manipulate the outgrowth of processes [Kaehr *et al.*, 2004].

From this discussion, it is clear that the various methodologies offer unique advantages and disadvantages. Ultimately, the decision to select a design rests on the application and available resources. For the application presented in this work, compatibility with the CMOS process is the determining factor. Material selection is limited due to handling of the CMOS chip, as well as packaging constraints. Other key design criteria include: alignment of the pattern to the underlying electrode array; flexibility of the adhesion mediator to tailor the process to different cell types (neurons versus cardiac myocytes); and long-term pattern fidelity (dissociated neurons require up to 3 weeks to become electrically active, at which point electrophysiological recordings may be made).

Method	Ease of Use	Patterning Flexibility	Resolution	Pattern Stability	MEA Compatibility
Micro-contact stamping (soft-lithography)	High	Medium: adhesion chemistry and substrate can be easily varied; stamp redesign required to change the pattern geometry	Medium: 2 - 500 $\mu\text{m}$	From 2 days to 3 weeks; highly dependent on surface chemistry	Poor: additional alignment to underlying electrodes required
Ink-jet printing	High: once printer is modified	High: adhesion chemistry, substrate and pattern geometry easily varied	Low: 10 - 100 $\mu\text{m}$	25 days if inhibitory background is used	Poor: additional alignment to underlying electrodes required
Photolithography	Medium: requires access to a clean-room	Medium: dependent on surface chemistry; mask design required to change pattern	High: sub-micron	2 - 3 weeks	Poor: engineered surface must be protected during dicing, otherwise chip-level photolithography required
Microfluidics	Medium: some technology involved (photolithography, use of fluidics)	Medium: easy to change chemistry; fluidics must be redesigned to change pattern	Low: microns	1 week survival in channels for neurons; 3 weeks for PC12 cells	Poor: additional alignment to underlying electrodes required
Mechanical immobilization	Low: complicated processing	Low: reprocess substrates to change pattern; physical constraints on realisable structures	Low: microns	2 - 8 days for cages and pillars; 2 weeks for topographical cues	Poor: additional alignment required
Real-time manipulation	Low: complicated apparatus	Medium: complicated pattern generation	High: sub-micron	Duration of the experiment (hours); long-term data not available	Good
Selective molecular assembly patterning	High: easy lift-off to structure the gold; simple dip-and-rinse technique	Medium: dependent on surface chemistry and pre-structures substrates	Medium: 3 - 5 $\mu\text{m}$	3 weeks for glia	High: self-aligning

Tab. 4.1: Summary of cell adhesion patterning techniques. See text for references.

## 4.2 PATTERNED CELL ADHESION

A strategy for patterned cell adhesion based on chemical surface modification was developed in this work (Fig. 4.2). The impetus motivating this work is the need to create a device for non-invasive activity measurements from a culture where the electrical signal travels through a defined region of cells. For example, in cardiology the propagation of the electrical signal through a region of cells is an important parameter. Signal propagation through a syncytium of cardiac myocytes is prone to a high degree of non-uniformities. Fig. 4.3 (left) shows the isochronal lines of a convex wavefront propagating through a perfused rabbit ventricular epicardial layer. If the cells are defined within a strand, Fig. 4.3 (right), then the propagation velocity wavefront becomes better defined. Going one step further, such a device could be combined with microfluidics, where each strand of cells is perfused with a different test compound, for example varying concentrations of the same substance. The experimental results are free of inter-culture variability as the experiment is performed under the exact same environmental conditions. What is more, testing is greatly expedited as many experiments are performed simultaneously.

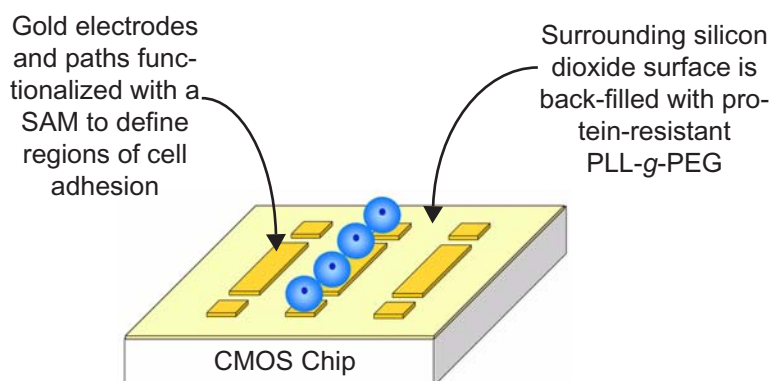


*Fig. 4.2: Strategy for patterned cell adhesion. Cells adhere to a self-assembled monolayer bound to a structured gold surface. The surrounding  $\text{SiO}_2$  is back-filled with a protein-resistant polymer, poly-L-lysine-graft-poly(ethylene glycol). The regions of gold define the areas of cell attachment.*

The strategy for high-contrast adhesion of cells to specific areas is based on the SMAP process introduced in the previous section. The main advantages offered by this process are that it is self-aligning to electrode array and it results in high-contrast patterns of cell adhesion. This process is introduced and described

in detail in Appendix C. Briefly, a thin layer of gold is structured on the  $\text{SiO}_2$  chip surface in a lift-off process. Since only a very thin gold film is required, it is relatively easy to achieve high-resolution structures. An amino-terminated alkane thiol, which defines the areas of cell attachment, is self-assembled on the gold (recall Eq. 4.1). In this case an amino-terminated alkane-thiol was selected because it is known that cells, such as neurons, adhere to the positively charged amino group [Stenger and McKenna, 1994, Kleinfeld *et al.*, 1988, Ruehe *et al.*, 1999]. The surrounding surface is functionalized with a protein-repellent grafted copolymer PLL-g-PEG, that adsorbs to  $\text{SiO}_2$ . PEG is well-known as a material resistant to protein adsorption, [Pasche 2004, Kenausis *et al.*, 2000, Prime and Whitesides, 1991]. Although the exact mechanism by which PEG blocks protein adsorption has been long debated in literature, recent work shows the many factors, acting simultaneously, are involved. These include, but are not limited to: electrical shielding and neutralization, physical shielding and steric exclusionary effects due to hydration (a complete evaluation is presented in Pasche 2004).

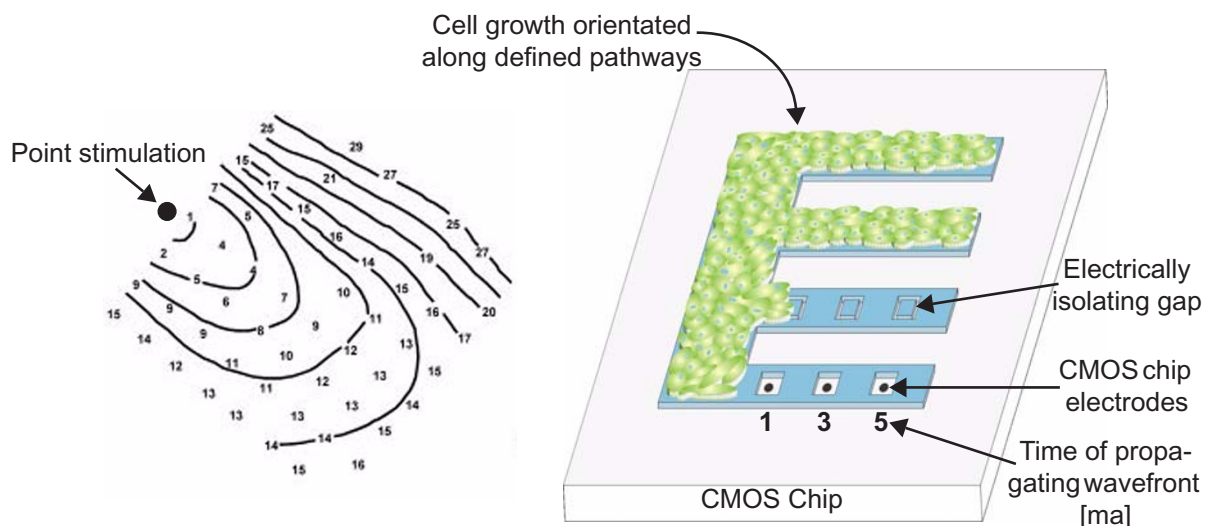


*Fig. 4.3: Example motivation for patterned adhesion of cardiac myocytes: nonuniform convex wavefront propagation through a perfused rabbit ventricular epicardial layer (left, from Kleber and Rudy, 2004). The isochronal lines are drawn at 3 ms. Idealized signal propagation through patterned strand of cells (right). The electrodes of the CMOS chip, indicated on the figure, are covered by structured gold, which forms the total recording area. The gold electrodes are electrically isolated from the rest of the gold pathway by a narrow gap. In this idealized schematic the propagating wavefront is measured at regular intervals: 1, 3, 5 ms.*

### 4.2.1 PROCESS CHARACTERIZATION

X-ray photoelectron spectroscopy (XPS) and variable angle spectral ellipsometry (VASE) surface analysis techniques were used to monitor the individual steps of the SMAP process. Experiment details and results, are presented in Appendix C. XPS measurements were used to identify that the SAM and PLL-g-PEG had indeed been immobilized at the appropriate surface. VASE was used to measure the thickness of the organic layer, as a means of supporting the XPS results. As a means of process control, ellipsometry was used to analyse at least two large-area samples per functionalization cycle. The XPS and ellipsometry results both show that the SMAP processing was successful.

### TEST CHIPS

Two test chip designs, denoted *design 1* and *design 2*, were used to characterize the SMAP process and the efficacy of cell patterning. Their design and fabrication is outlined in Appendix C. Design 1 is a large area chip, 14 x 14 mm<sup>2</sup>, half native SiO<sub>2</sub> and half gold. Design 2 comprised varying gold patterns on a glass substrate (refer to Fig. 3 in Appendix C). With respect to surface functionalization, native SiO<sub>2</sub> and glass were considered to be chemically equivalent.

### 4.2.2 PROTEIN ADHESION

In some cases, it may be desirable to generate patterns of specific proteins that the cells then adhere to (scheme A in Fig. 4.1). For example neurons, which are extremely sensitive to their environment, may not develop properly on amino-functionalized surfaces alone. In such cases, the functionalized surface could be to patterns proteins as well. In this section, the results of a preliminary experiment are presented, the goal of which is to explore the versatility of the functionalized surfaces.

Patterned substrates were treated in solutions of the following proteins and polymers known to mediate cell adhesion: laminin, Matrigel, fibronectin, gelatin, poly-L-lysine, poly-L-ornithine and collagen (Tab. 4.2). Full serum was used as a control. Laminin, fibronectin, gelatin and collagen are all constituents of the ECM, see Sec. 2.2. Matrigel is a solubilized form of the basement membrane, a thin extracellular matrix underlying cells *in vivo*. It is predominantly laminin, with collagen IV, heparan sulfate proteoglycans and other growth factors. It is known to promote adhesion of neurons and the outgrowth of neurites.



Tab. 4.2: List of adhesion mediators with deposition protocols.

Mediator	Deposition Protocol	Vendor
Laminin	Incubation (37 °C, 5 % CO <sub>2</sub> ) for 24 hours in 20 µg/ml PBS	Sigma-Aldrich, U.S.A.
Matrigel	Samples were incubated for 30 min. in ~ 100 µl of 1:50 Matrigel in Hanks balanced salt solution (Sigma-Aldrich)	BD Biosciences, U.S.A.
Fibronectin	Incubation for 24 hours in 0.5% in 0.02% gelatin solution	Sigma-Aldrich, U.S.A.
Gelatin	Incubation for 24 hours in 0.02% in de-ionized water	Sigma-Aldrich, U.S.A.
Collagen	Incubation for 24 hours in 2% in 0.02% gelatin solution	Collaborative Biomedical Products, U.S.A.
Poly-L-lysine	Incubation for 24 hours in 0.1% in de-ionized water	Sigma-Aldrich, U.S.A.
Poly-L-ornithine	Incubation for 24 hours in 15 mg/ml de-ionized water	Sigma-Aldrich, U.S.A.
Human Control Serum N	20 min. at room temperature in HEPES 2 buffer	Roche, Switzerland

Large-area substrates (1 x 2 cm<sup>2</sup>), half Au and half TiO<sub>2</sub> were prepared using the SMAP process described in Appendix C. TiO<sub>2</sub> was used instead of SiO<sub>2</sub> to demonstrate that the patterning process can be used with different oxides. Immediately following functionalization, the surfaces were sterilized with 70% ethanol, dried with N<sub>2</sub>, and exposed to solution containing the adhesion mediator according to the protocols outlined in Tab. 4.2. The samples were then carefully rinsed in deionized water and dried with N<sub>2</sub>. Ellipsometry measurements were performed after SAM deposition, copolymer adsorption and following treatment with the protein/polymeric adhesion mediator. The measured organic layer thicknesses are given in Tab. 4.3. Included is the overall average and standard deviations for the SMAP process on Au/TiO<sub>2</sub>. The SAM thickness immediately following assembly is slightly thinner, 14.6 ± 2.3 Å, than the value reported in Appendix C, 18.9 ± 4.1 Å. Following polymer adsorption, the SAM layer was found to be even thinner, 9.5 ± 1.2 Å. This discrepancy is thought to be due to material degradation, however the overall efficiency of the system is not expected to be adversely affected. The thickness of the PLL-g-PEG on TiO<sub>2</sub>, 16.7 ± 1.6 Å, is similar to that measured on SiO<sub>2</sub>, 14.2 ± 1.2 Å (from Appendix C).

The adhesion of most of the protein mediators, including serum, is successfully controlled by the patterned surfaces. In the case of full serum, the organic layer thickness increases to 49.2 Å on the gold side, while that on the TiO<sub>2</sub> remains thin at 17.2 Å, which is approximately the thickness of the PLL-g-PEG. The organic layer thickness for TiO<sub>2</sub> treated directly with serum has been found to be 33.0 Å, indicating that the patterning procedure is indeed successful. Laminin and Matrigel adhere well to the SAM, as indicated by the organic layer thicknesses on the Au side of 54.1 Å and 45.6 Å, respectively. On the SiO<sub>2</sub> side, the organic layer thickness increases from 20.1 Å to 31.4 Å for laminin, and from 17.3 Å to 19.7 Å for Matrigel. This indicates that the polymer adequately blocks Matrigel adsorption, while it is only somewhat resistant to pure laminin. It is known from previous experiments that the thickness of Matrigel adsorbed onto freshly cleaned SiO<sub>2</sub> substrates is 56.8 Å. TiO<sub>2</sub> and SiO<sub>2</sub> have negatively charged surfaces and laminin adsorption is believed to be similar on both. This further indicates that the polymer successfully blocks Matrigel adsorption. Similarly, the adsorption of gelatin and collagen is patterned by the engineered surfaces, while the results for fibronectin are inconclusive. In the case of the polymeric adhesion mediators, the materials appear to adsorb to the SAM, while actually reducing the organic layer thickness on the TiO<sub>2</sub> surface.

It is possible that the proteins replace the PLL-g-PEG molecules in a substitution reaction (Vroman effect). Therefore, the results presented in this section should be considered an indication of functionalized surface's ability to pattern proteins. A secondary measurement technique, such as XPS, is needed to analyze the surface composition.

Tab. 4.3: VASE results for  $\text{TiO}_2/\text{Au}$  substrates measured after each step in SMAP process and following treatment with an adhesion mediator/serum.

Mediator	$\text{TiO}_2$ Thickness [nm]	After SAM Organic Layer Thickness [Å]		After PLL-g-PEG Organic Layer Thickness [Å]		After Mediator/Serum Organic Layer Thickness [Å]	
		Au Side	$\text{TiO}_2$ Side	Au Side	$\text{TiO}_2$ Side	Au Side	$\text{TiO}_2$ Side
Laminin	20.8	13.8	9.8	11.0	20.1	54.1	31.4
Matrigel	20.7	10.2	7.6	8.1	17.3	45.6	19.7
Fibronectin	20.5	14.0	5.4	9.0	15.2	37.4	39.8
Gelatin	20.6	14.8	6.2	8.9	16.0	23.0	17.5
Collagen	20.6	14.7	6.7	11.3	17.6	18.0	16.1
Poly-L-lysine	20.5	14.8	6.3	8.4	16.0	10.4	10.8
Poly-L-ornithine	20.6	16.7	6.3	9.2	15.7	14.5	11.1
Serum	20.4	18.1	6.2	10.0	15.5	49.2	17.2
<b>Average</b>	20.6	14.6	6.8	9.5	16.7		
<b>Standard Deviation</b>	0.1	2.3	1.4	1.2	1.6		

### 4.2.3 PATTERNED CARDIOMYOCYTES

Although the engineered surface was developed for both neural and cardiac cell types, it has been tested primarily with cardiac myocytes. These results are presented in Appendix C. Fluorescence staining was used to visualize the locations of the cells. Results show that the chemical patterns define the location of the HL-1 cells for 7 DIV, at which point the experiment was terminated. The NRC's were plated on the Design 2 chip for the purpose of determining: (1) the minimum gold line width required for a continuous strand of cells; and (2) the maximum gap, the electrically isolating space between the electrodes and the gold path (refer to fig. 4.3), that the cells would overgrow. Fig 7 (Appendix C) shows that the cells are continuous in a  $60\text{-}\mu\text{m}$ -wide gold path. Fig 8 (Appendix C) shows that the cells bridge gaps of 5 and  $10\text{ }\mu\text{m}$ . The pattern was successfully applied to the CMOS chip, as shown in Fig 9 (Appendix C).

### CELL DIFFERENTIATION

A requirement of chemical patterning is the demonstration that normal cell functioning is retained even when the cells are cultured on the modified surface. One way to test this is to show that certain typical cell architectures are present. Two different myofibrillar structures that are characteristic of differentiated cardiac muscle cells have been investigated. The first is the thick filaments, and the second is the z-disk) (both are parts of the sarcomere schematically represented in Fig. 2.5). When constituent proteins of either these structures are stained, fluorescence microscopy should reveal highly organized, striated patterns.

Neonatal rat cardiomyocytes were cultured on design 2 test chips that had been functionalized with the SMAP process (see Fig. 3 in Appendix C). To visualize the thick filaments, cardiac myosin-binding protein C was first stained with a polyclonal rabbit antibody (pR anti MyBP-C, which was provided by Jean-Claude Perriard, ETH, Zurich and Matias Gautel, King's College London, van der Ven, *et al.*, 1999). A second fluorescing antibody, goat-anti-rabbit cy3 (GaR cy3, Jackson ImmunoResearch Laboratories Inc., U.S.A.) was attached to the first anti-body. Figure 4.4 (left) shows the fluorescence microscopy image of the stained thick filaments. To visualize the z-disks, the monoclonal anti- $\alpha$ -actinin (Sigma Clone EA53, Sigma) was used. In this case, the second anti-body was goat-anti-mouse cy3 (Jackson). The resultant fluorescence microscopy image is shown in Fig. 4.4 (right). In both cases, well-ordered, striated structures indicative of myofibrillogenesis are distinguishable. Note that, in addition to staining the sarcomere, the nucleus and actin filaments were stained with 4', 6'-diamidino-2 phenylindole dihydrochloride (DAPI, Sigma) and Alexa Fluor 488 phalloidin (Molecular Probes, USA), respectively. The staining protocol is given in Appendix E.

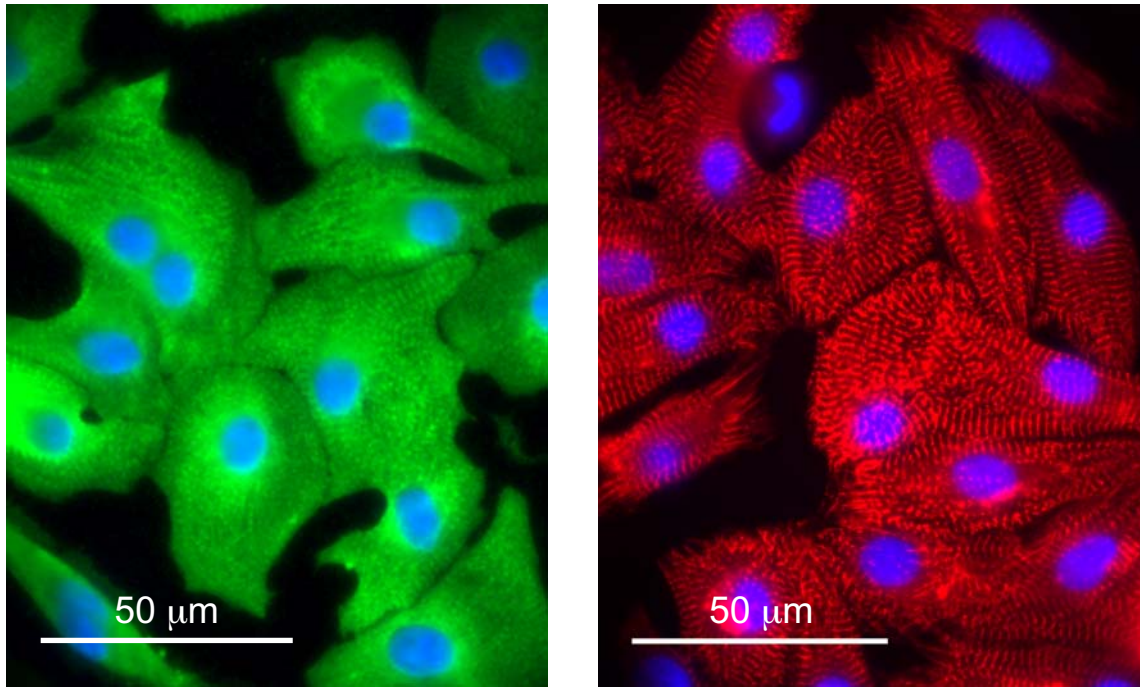


*Fig. 4.4: Fluorescence microscopy images showing proper sarcomeric differentiation. NRC's were cultured on glass chips patterned with gold, referred to as design 2 test chip in Appendix C, which had been functionalized with the SMAP process. The NRC's shown in the image on the left have been stained for cardiac myosin-binding protein C to visualize the thick filaments of the sarcomere. The NRC's shown in the image on the right have been stained for  $\alpha$ -actinin to visualize the z-disks. In both images, highly ordered, striated patterns indicative of the sarcomere are clearly distinguishable. The nucleus has been stained with DAPI. Although the actin filaments were also stained with Phalloidin, the fluorescence is not shown for enhanced clarity. Cells were fixed at 4 DIV.*

#### 4.2.4 PATTERNED NEURAL NETWORKS

Initial experimental results of patterned neural cultures are presented in this section. Design test chip 2 was also tested with cultures of dissociated rat hippocampal neurons. For this experiment, chips were sent to Elisabetta Ruaro (at the Scuola Superiore di Studi Avanzati (SISSA), Trieste, Italy), who performed the

cell preparation, plating, maintenance and immunofluorescence microscopy. The chips were prepared according to the procedure detailed in Appendix C. Dissociated hippocampal neurons were plated on the chips at a concentration of approximately  $8.0 \times 10^5$  cells/cm<sup>2</sup> according to the protocol outlined in Appendix D [Ruaro *et al.*, 2005]. After 3 weeks *in vitro* the cells were fixed. To determine whether neurons had been immobilized, immunofluorescence staining was performed. Neurons were visualized using TUJ1 (Covance Research Products Inc., U.S.A.), an anti-neuron-specific class III beta-tubulin antibody that reacts with class III beta-tubulin of neurons only, and does not identify with beta-tubulin found in glia. This antibody stains neuronal cell bodies, axons and axonal terminations. Glia cells were identified using the GFAP antibody (glial fibrillary acidic protein, Sigma). The cell nucleus was stained with Hoechst DNA stain (Sigma). Resultant immunofluorescence images are shown in Fig. 4.5. The low magnification image, Fig. 4.5 (A), shows that cell growth is indeed confined to the gold pathways. However, Fig. 4.5 (B) shows that the majority of the cells are glia. Cell bodies from two neurons, and their dendrites, can be identified in Fig. 4.5 (C). Since glia cells proliferate, whereas neurons do not, it is not uncommon that the glia cell population will overtake the neural cell population. However, in a typical culture, more neurons are normally present. The reason for the low neural population is not clear. The patterned surface may be deleterious to neural growth, or the preparation may have initially contained a low neural count.

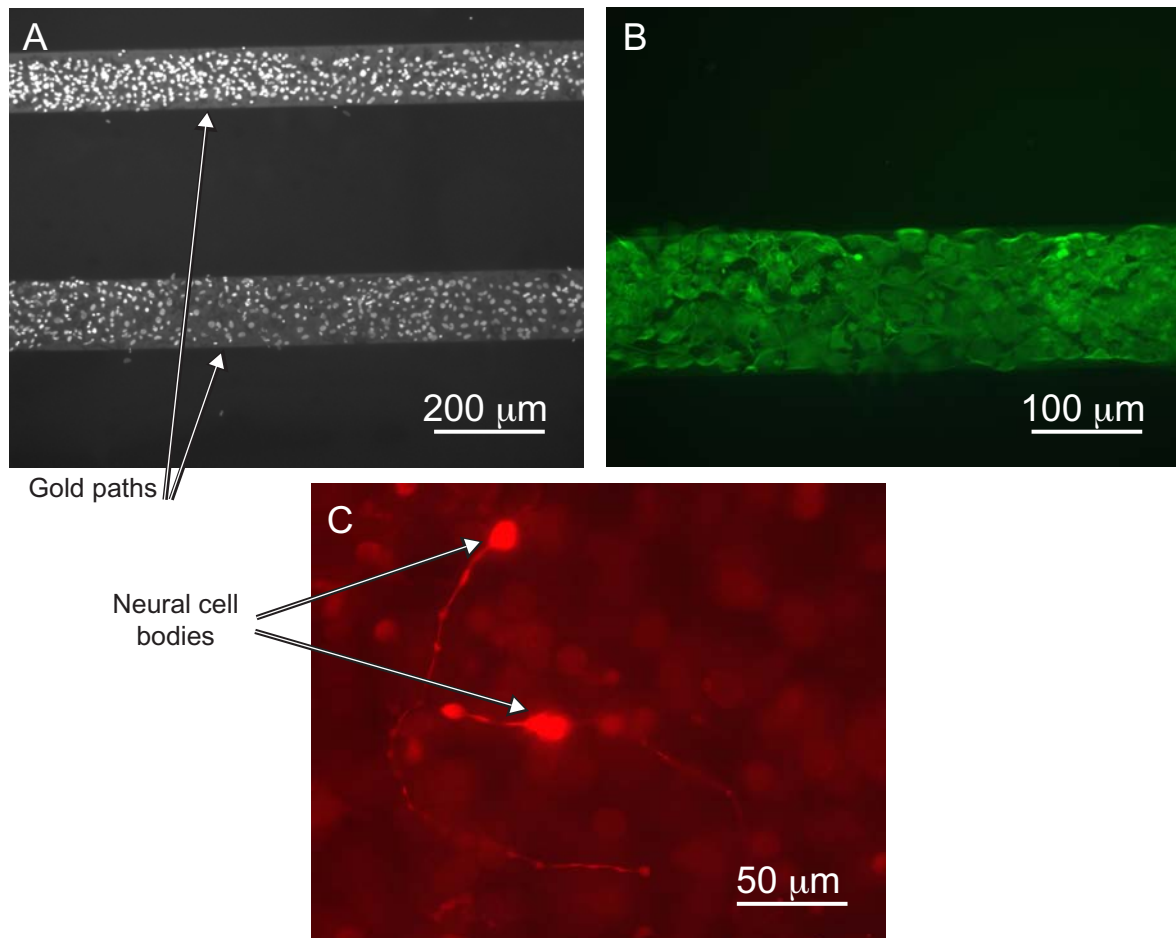


*Fig. 4.5: Immunofluorescence microscopy of rat hippocampal neurons and glia cells at 21 DIV cultured on functionalized Design 2 test chips. Image A shows the Hoechst-stained cell nuclei. Cell adhesion is confined to the gold paths. The glia cells have been stained with the GFAP antibody, image B; and the neurons have been stained with TUJ1, image C. At least two neural cell bodies are visible. The majority of the cells growing on the SAM-treated gold surface are glia.*

### 4.3 SUMMARY AND CONCLUSIONS

In the first half of this chapter the various patterning techniques reported in literature were presented. An attempt has been made to highlight the key characteristics of each method. Although many parameters may be considered, the decision

to select one technique is largely dependent on the application and available resources, e.g. access to cleanroom facilities.

To chemically functionalize the surface of a CMOS MEA, the SMAP procedure is ideal. Preparation of the Au/SiO<sub>2</sub> surface is prepared using the lift-off procedure, which is well-known in microfabrication. The thinness of the gold layer means that high resolution structures can be achieved. The dip-and-rinse procedure is compatible with CMOS chip and package, demonstrating that the technique can be used to create a more complex cell-based biosensor system.

It is known that proteins from the medium may replace the PLL-g-PEG molecule in a substitution reaction. This is not expected to adversely affect long-term pattern fidelity for culture of *non-dividing* cells, such as cardiomyocytes. Indeed, results show that NRC's retain the pattern structure at 4 DIV. Videos have been made of the beating NRC's on a patterned CMOS chip up to 7 DIV.

Immunofluorescence staining was used to investigate cell differentiation. When cells are cultured on the functionalized surface, they develop striated, sarcomeric structures indicative of muscle fibres. It is important to study the microstructure of the cell *in vitro* to gain an understanding of the differences between the *in vivo* and *in vitro* cell.

For co-cultures of neurons and glia cells, substitution of PLL-g-PEG by a protein becomes more critical. While neural cells do not divide, glia cells do. Initial results with a neural/glia cell co-culture indicate that the pattern is retained at 21 DIV, although only a few neuronal cells were found in the culture. That not many neural cells were present in the culture could be because they do not develop well on the amino groups. These findings prompted the experiment to investigate the patterning of adhesion mediators such as laminin and Matrigel. Although the protein patterning experiment results are not conclusive, they indicate that the adhesion mediators tested can be patterned, thereby increasing the flexibility of the system for use with various cell types.

## 4.4 REFERENCES

Bernard, A., Delamarche, E., Schmid, H., Michel, B., Bosshard, H. R., Biebuyck, H. (1998). "Printing patterns of proteins." *Langmuir*, 14(9), 2225-2229.



- Borgens, R. B. (1999). "Electrically mediated regeneration and guidance of adult mammalian spinal axons into polymeric channels." *Neuroscience*, 91(1), 251-64.
- Britland, S., Perridge, C., Denyer, M., Morgan, H., Curtis, A. S., and Wilkinson, C. D. (1996A). "Morphogenetic guidance cues can interact synergistically and hierarchically in steering nerve cell growth." *Expmntl. Bio. Online*, 1(2), 1-12.
- Britland, S., Morgan, H., Wojniak-Stodart, B., Riehle, M., Curtis, A., and Wilkinson, C. (1996B). "Synergistic and hierarchical adhesive and topographic guidance of BHK cells." *Exp Cell Res*, 228(2), 313-25.
- Britland, S., and McCaig, C. (1996C). "Embryonic *Xenopus* neurites integrate and respond to simultaneous electrical and adhesive guidance cues." *Exp Cell Res*, 226(1), 31-8.
- Dowell-Mesfin, N. M., Abdul-Karim, M.-A., Turner, A. M. P., Schanz, S., Craighead, H. G., Roysam, B., Turner, J. N., and Shain, W. (2004). "Topographically modified surfaces affect orientation and growth of hippocampal neurons." *Journal of Neural Engineering*(2), 78-90.
- Erskine, L., and McCaig, C. D. (1997). "Integrated interactions between chondroitin sulphate proteoglycans and weak dc electric fields regulate nerve growth cone guidance in vitro." *J Cell Sci*, 110 ( Pt 16), 1957-65.
- Falconnet, D., Koenig, A., Assi, F. Textor, M. (2004). "A Combined Photolithographic and Molecular-Assembly Approach to Produce Functional Micropatterns for Applications in the Biosciences." *Advanced Functional Materials*, 14(8), 749-756.
- Falconnet, D. (2005). "Molecular assembly patterning by lift-off at the micro- and nano-scale for applications in the biosciences," Swiss Federal Institute of Technology, Zurich.
- Fan, Y. W., Cui, F. Z., Houb, S. P., Xub, Q. Y., Chenb, L. N., Lee, I. -S. (2002). "Culture of neural cells on silicon wafers with nano-scale surface topograph." *Journal of Neuroscience Methods*, 120(1), 17-23.
- Griscom, L., Degenaar, P., LePioufle, B., Tamiya, E., and Fujita, H. (2002). "Techniques for patterning and guidance of primary culture neurons on micro-electrode arrays." *Sensors and Actuators B (Chemical)*, 83(1-3), 15 - 21.

Jung, D. R., Kapur, R., Adams, T., Giuliano, K. A., Mrksich, M., Craighead, H. G., and Taylor, D. L. (2001). "Topographical and physicochemical modification of material surface to enable patterning of living cells." *Crit Rev Biotechnol*, 21(2), 111-54.

Kaehr, B., Allen, R., Javier, D. J., Currie, J., and Shear, J. B. (2004). "Guiding neuronal development with in situ microfabrication." *Proc Natl Acad Sci U S A*, 101(46), 16104-8.

Kane, R. S., Takayama, S., Ostuni, E., Ingber, D. E., and Whitesides, G. M. (1999). "Patterning proteins and cells using soft lithography." *Biomaterials*, 20(23-24), 2363-76.

Kenausis, G., Voros, J., Elbert, D., Huang, N., Hofer, Ruiz-Taylor, L., Textor, M., Hubbell, J., Spencer, N. (2002). "Poly(L-lysine)-g-poly(ethylene glycol) layers on metal oxide surfaces: attachment mechanism and effects of polymer architecture on resistance to protein adsorption." *J. of Phys. Chem. B*, 104(14), 3298-3309.

Kim, E., Xia, Y., Whitesides, G. (1995). "Polymer microstructures formed by moulding in capillaries." *Nature*, 376(17), 581-584.

Klebe, R. J. (1988). "Cytoscribing: a method for micropositioning cells and the construction of two- and three-dimensional synthetic tissues." *Exp Cell Res*, 179(2), 362-73.

Kleber, A. G., and Rudy, Y. (2004). "Basic mechanisms of cardiac impulse propagation and associated arrhythmias." *Physiological Reviews*, 84(2), 431-88.

Kleinfeld, D., Kahler, K., and Hockberger, P. (1988). "Controlled outgrowth of dissociated neurons on patterned substrates." *J. Neurosci.*, 8(11), 4098-4120.

Lopez, G., Biebuyck, H., Harter, R., Kumar, A., Whitesides, G. (1993). "Fabrication and imaging of two-dimensional patterns of proteins adsorbed on self-assembled monolayers by scanning electron microscopy." *Journal of American Chemical Society*, 115(23), 10774-10781.

Lussi, J. W., Michel, R., Reviakine, I., Falconnet, D., Goessl, A., Csucs, G., Hubbell, J. A., and Textor, M. (2004). "A novel generic platform for chemical patterning of surfaces." *Progress in Surface Science*, 76(3-5), 55-69.

- Maher, M. P., Pine, J., Wright, J., and Yu Chong, T. (1999). "The neurochip: A new multielectrode device for stimulating and recording from cultured neurons." *Journal of Neuroscience Methods*, 87(1), 45-56.
- Martinoia, S., Bove, M., Tedesco, M., Margesin, B., and Grattarola, M. (1999). "A simple microfluidic system for patterning populations of neurons on silicon micromachined substrates." *Journal of Neuroscience Methods*, 87(1), 35-44.
- Michel, R., Lussi, J., Csucs, G., Reviakine, I., Danuser, G., Ketterer, B., Hubbell, J., Textor, M., and Spencer, N. (2002). "Selective Molecular Assembly Patterning: A New Approach to Micro- and Nanochemical Patterning of Surfaces for Biological Applications." *Langmuir*, 18(8), 3281-3287.
- Mrksich, M., Dike, L. E., Tien, J., Ingber, D. E., and Whitesides, G. M. (1997). "Using microcontact printing to pattern the attachment of mammalian cells to self-assembled monolayers of alkanethiolates on transparent films of gold and silver." *Exp Cell Res*, 235(2), 305-13.
- Offenhausser, A., Ruhe, J., and Knoll, W. (1995). "Neuronal cells cultured on modified microelectronic device surfaces." *Journal of Vacuum Science & Technology A (Vacuum, Surfaces, and Films)*, 13(5), 2606-12.
- Pasche, S. (2004). "Mechanisms of protein resistance of adsorbed PEG-graft copolymers," Swiss Federal Institute of Technology, Zurich.
- Prime, K., and Whitesides, G. (1991). "Self-assembled organic monolayers: model systems for studying adsorption of proteins at surfaces." *Science*, 252(5010), 1164-7.
- Prucker, O., Naumann, C., Ruehe, J., Knoll, W., Frank, C. (1999). "Photochemical Attachment of Polymer Films to Solid Surfaces via Monolayers of Benzophenone Derivatives." *Journal of American Chemical Society*, 121(39), 8766-8770.
- Rohr, S., Scholly, D. M., and Kleber, A. G. (1991). "Patterned growth of neonatal rat heart cells in culture. Morphological and electrophysiological characterization." *Circ Res*, 68(1), 114-30.
- Ruaro, M. E., Bonifazi, P., Torre, V. (2005). "Towards the neurocomputer: image processing and pattern recognition with neuronal cultures." *IEEE Transactions on Biomedical Engineering*.

- Ruhe, J., Yano, R., Lee, J. S., Koberle, P., Knoll, W., and Offenhausser, A. (1999). "Tailoring of surfaces with ultrathin polymer films for survival and growth of neurons in culture." *Journal of Biomaterials Science-Polymer Edition*, 10(8), 859-874.
- Sanjana, N., Fuller, S. (2004). "A fast flexible ink-jet printing method for patterning dissociated neurons in culture." *J. of Neuro. Meth.*, 136(2), 151-163.
- Scholl, M., Sprossler, C., Denyer, M., Krause, M., Nakajima, K., Maelicke, A., Knoll, W., and Offenhausser, A. (2000). "Ordered networks of rat hippocampal neurons attached to silicon oxide surfaces." *J. of Neuro. Meth.*, 104(1), 65-75.
- Sorribas, H., Padeste, C., and Tiefenauer, L. (2002). "Photolithographic generation of protein micropatterns for neuron culture applications." *Biomaterials*, 23(3), 893-900.
- Stenger, D. A., McKenna, T. M. (1994). *Enabling Technologies for Cultured Neural Networks*, Academic Press, London.
- Takayama, S., McDonald, J. C., Ostuni, E., Liang, M. N., Kenis, P. J., Ismagilov, R. F., and Whitesides, G. M. (1999). "Patterning cells and their environments using multiple laminar fluid flows in capillary networks." *Proc Natl Acad Sci U S A*, 96(10), 5545-8.
- Thomas, S. P., Bircher-Lehmann, L., Thomas, S. A., Zhuang, J., Saffitz, J. E., and Kleber, A. G. (2000). "Synthetic strands of neonatal mouse cardiac myocytes: structural and electrophysiological properties." *Circ Res*, 87(6), 467-73.
- Turcu, F., Tratsk-Nitz, K., Thanos, S., Schuhmann, W., and Heiduschka, P. (2003). "Ink-jet printing for micropattern generation of laminin for neuronal adhesion." *J Neurosci Methods*, 131(1-2), 141-8.
- Wyart, C., Ybert, C., Bourdieu, L., Herr, C., Prinz, C., and Chatenay, D. (2002). "Constrained synaptic connectivity in functional mammalian neuronal networks grown on patterned surfaces." *J. of Neuro. Meth.*, 117(2), 123-131.
- Zeck, G., and Fromherz, P. (2001). "Noninvasive neuroelectronic interfacing with synaptically connected snail neurons immobilized on a semiconductor chip." *Proceedings of the National Academy of Sciences of the United States of America*, 98(18), 10457-10462.

---

# 5 ELECTROPHYSIOLOGICAL RECORDINGS

Experimentation with electrophysiology is by no means new. In 1791, Luigi Galvani electrically stimulated the nerve-muscle junction of a frog, eliciting leg movement. Since then, the metal-electrogenic cell interface has found many uses in both applied and pure science. Beginning in the 1950's, extracellular recordings have been used to study the physiology of the brain at the cellular level [Kandel *et al.*, 2000]. On the clinical side, pace makers and cochlear implants have advanced to the stage that they have a significant impact on longevity and quality of life. A less well-known example is the use of neural implants in the treatment of epilepsy. Neural prostheses are used to monitor brain activity during an epileptic attack, providing valuable information about the nature and location of the seizure focus (the origin of the seizure event). Accurate identification of the seizure focus is critical since, in severely debilitating cases, these regions are surgically removed [Kandel *et al.*, 2000]. Looking to the future, bioelectronic prostheses may be used for artificial limbs, visual prostheses and to alleviate the symptoms of Parkinson's disease [Stieglitz *et al.*, 2004].

What is new in this field is the combination of CMOS circuitry, with metal transducing electrodes, to record and stimulate signals from electrogenic cells. CMOS circuitry serves three purposes: (1) signal conditioning as close to the source as possible mediates noise and electromagnetic distortion introduced as the signal passes down long wires and through interconnects; (2) multiplexing translates into an array size that is not limited by the number of available interconnects; and (3) high volumes of chips can be inexpensively produced by taking advantage of industrial manufacturing facilities. However, there are several technology issues associated with the development of a CMOS biosensor. First and foremost, the chip must be protected from the culture environment, as has been discussed in Sec. 3.1.3. Secondly, cell culturing is typically performed on transparent substrates to enable optical inspection. When using a CMOS biosensor, cells can only be visualized using a low-magnification upright microscope (high-magnification, short working-distance objectives cannot be located close enough to the

sample due to the medium and the package), or with fluorescent dyes (which usually means that the cells have been fixed in paraformaldehyde). Finally, CMOS is not inexpensive. One engineering run consisting of six 6" CMOS wafers manufactured in a 0.6- $\mu\text{m}$ , triple-metal, double-polysilicon technology costs EUR 40,000, access to expensive cleanroom facilities is required for post-processing, and the ceramic package used here runs USD 25.00 per piece.

Original work combining CMOS circuitry and neural prostheses comes from Ken Wises's group at the University of Michigan [Tanghe and Wise, 1991, Kim and Wise, 1996]. Devices generally consist of electrodes fashioned on multiple shanks with CMOS circuitry located either at the base of the shank, or, in a quasi two-chip solution, on a separate chip connected to the shanks via flexible interconnects. For *in vitro* studies, a two-chip solution was initially realized [Pancrazio *et al.*, 1998]. Single chip-solutions have been developed in Greg Kovacs's group at Stanford University, where circuitry was used for multiplexing, buffering, digital interfacing and temperature monitoring [DeBusschere and Kovacs, 2001]. Infineon Technologies together with Peter Fromherz at the Max Planck Institute in Martinsried, Germany have developed 16,384-electrode CMOS chip replete with amplification, readout multiplexing and buffering circuitry [Eversmann *et al.*, 2003]. The chips used in this work are original in that they comprise both readout and stimulation circuitry realized using analog and digital circuitry.

The focus of this chapter is the CMOS recording system and the electrophysiological recordings performed with it. This includes: a qualitative description of the chip and recording system architecture; an introduction to the two generations of chip design; a description of the electrode platinization process; and the electrophysiological recordings performed with both chip designs. The first generation chip was used to make field potential recordings from organ cultures, whereas recordings from both cardiac myocyte and neural cell cultures were performed with the 2<sup>nd</sup> generation chip<sup>1</sup>. As mentioned in Chapter 3, the cardiac myocyte cell cultures were used to develop the measurement system. Once it was demonstrated that the system could be used to measure cardiac myocyte field potentials, recordings with neural cell cultures were attempted. Neural cell culturing and organ culturing was performed by Axel Blau, Barbara Kochte-Klemens and Tanja Ugniwenko at the University of Kaiserslautern, Germany.

---

1. For the non-biologist, *organ culture* implies a three-dimensional culture of undisaggregated tissue, whereas *cell culture* refers to a culture of cells dissociated by enzymatic, mechanical or chemical disaggregation [Fresney 2000].

## 5.1 RECORDING SYSTEM

The architecture of the recording system is schematically represented in Fig. 5.1. In general, both generations of the CMOS chip have the same architecture: an array of electrodes where each electrode has an associated unit of circuitry for signal conditioning; one analog-to-digital converter per row; a single digital-to-analog converter used for stimulation; and a digital core that interfaces between the chip and the computer. Due to the modular design, the array size is flexible, 4 x 4 for the first generation and 16 x 8 for the second.

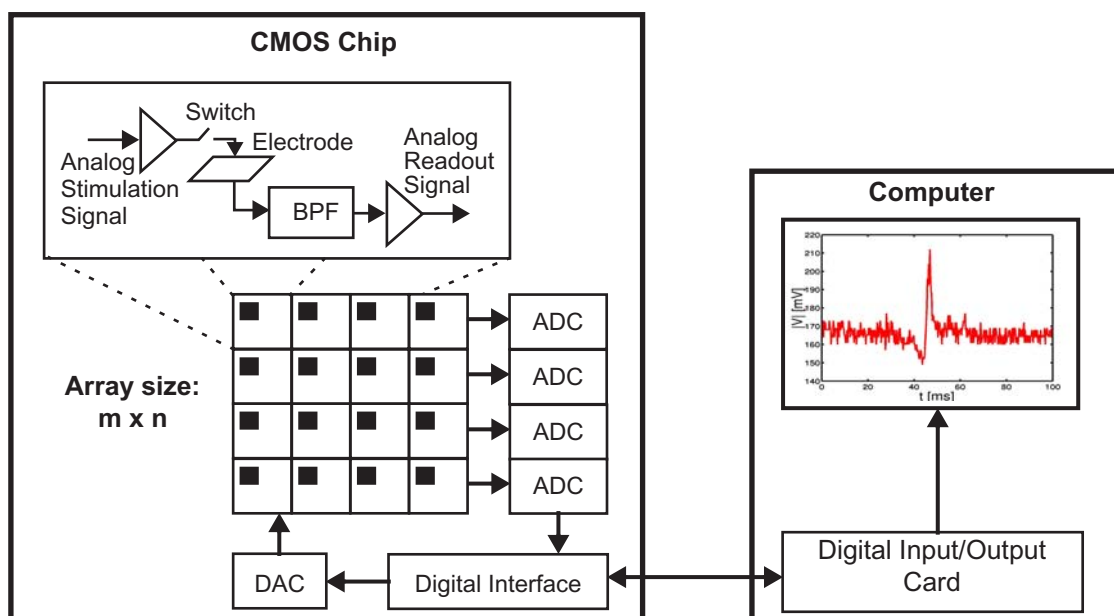


Fig. 5.1: Schematic representation of the system architecture. Recorded signals are conditioned as close to the electrode as possible. Each electrode has a unit of associated circuitry primarily comprising a band-pass filter (BPF), amplifiers and a switch to select the electrode for stimulation. Recorded data flows via an analog-to-digital converter (ADC) and the digital interface to the computer. Digitized data is displayed on the computer using LabView software and a digital input/output card. The digital interface also serves to transfer the stimulation signal, which flows through the digital-to-analog converter (DAC) to each electrode selected for stimulation. Note that the array size is scalable: 4 x 4 for the 1<sup>st</sup>-generation chip and 16 x 8 for the 2<sup>nd</sup>-generation chip.

Referring to Fig. 5.1, the recorded signal is first band-pass filtered and amplified (inset) before being digitized by an analog-to-digital converter (ADC) located at the end of each row. The digital interface continuously scans the array and manages data stream-out to the computer. Recordings are displayed on the computer using LabView software and a National Instruments digital input-output card (NI DAQ Card 6533). For stimulation, the digital interface is used to select the appropriate electrodes (indicated by the switch shown in figure inset). The stimulation signal is set by the user and distributed across the array via a digital-to-analog converter (DAC). A buffer at each electrode ensures that the stimulation signal amplitude is the same at each selected electrode. Design details of the various architecture components for the first- and second-generation design are given in Tab. 5.1. Full details on the circuitry is included in Appendix B.

*Tab. 5.1: Electrical and physical properties of the 1<sup>st</sup>- and 2<sup>nd</sup>-generation chip.*

Property	1st Generation	2nd Generation
Array Size	4 x 4	16 x 8
Pixel Pitch [ $\mu\text{m}$ ]	250	250
Electrode Size [ $\mu\text{m}$ ] and shape	40, square	10, 20, 30, 40 spherical
Amplification	1,000	1,000 or 3,000
Band-pass filter corner frequencies [kHz] <sup>a</sup>	Low-pass: 50 High-pass: 0.1	High-pass: $10^{-3}$ - 1 Low-pass: 1 - 30
Analog-to-digital Converter Resolution	8-bit	8-bit
Digital-to-analog Converter Resolution	8-bit	8-bit
Stimulation Signal	120 kHz, +/- 2.5 V	60 kHz, +/- 2.5 V
Sample Rate [kHz]	20	20 - 160
Noise [ $\mu\text{V}$ , 10 Hz - 100 kHz]	8.7	5.9

a. The order of the corner frequencies reflects the order in which the filters were implemented on the chip, i.e. the 1<sup>st</sup>-generation chip has first a low pass filter, followed by a high-pass filter.



### 5.1.1 CMOS CHIP

Two generations of the CMOS chip were used in this work, see Fig. 5.2. The first is a 4 x 4 array, and the second is a 16 x 8 array. In both cases, post-processing was used to create the shifted electrodes described in Sec. 3.1.2. Chips were packaged according to the scheme outlined in Sec. 3.2.

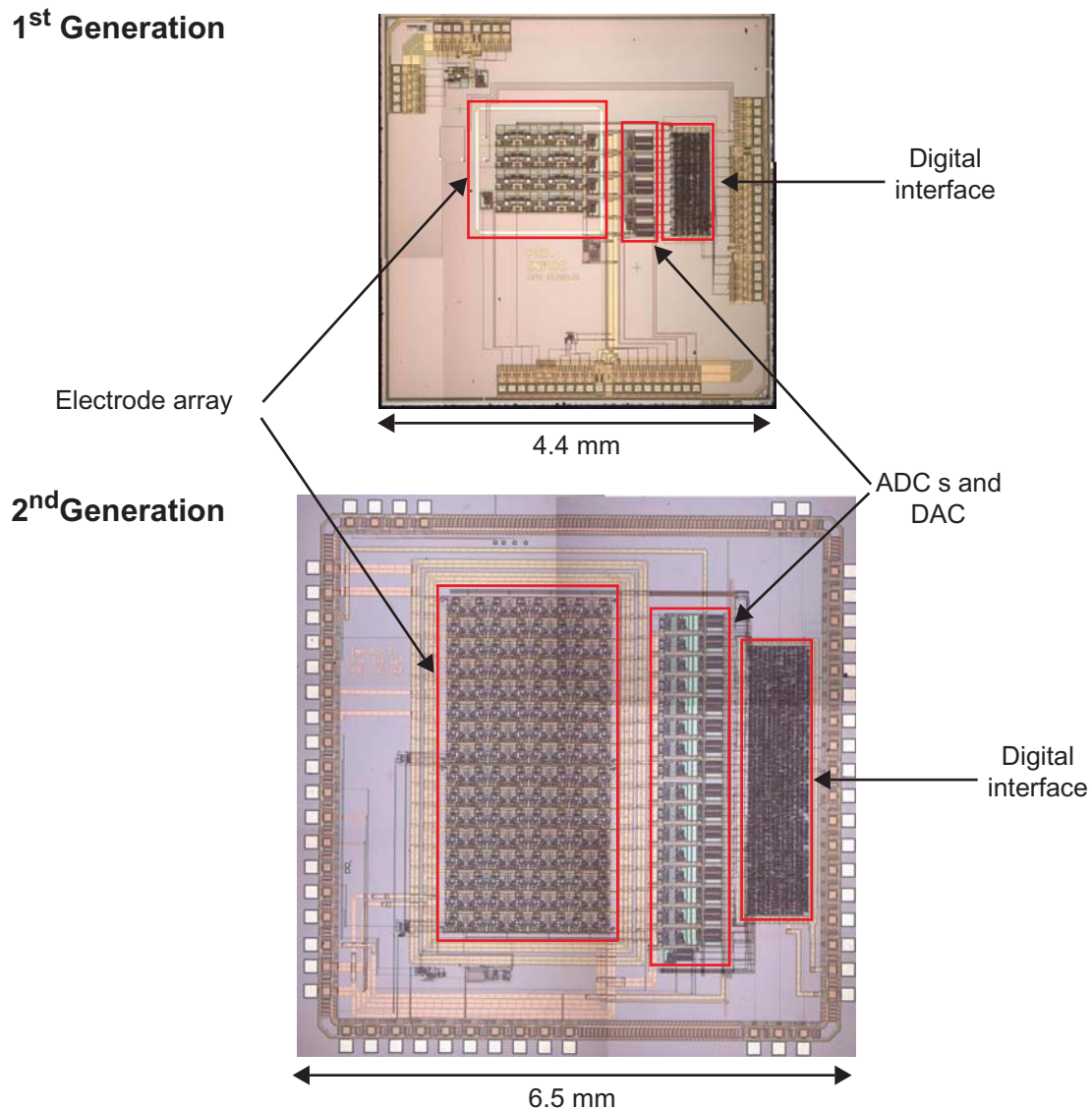
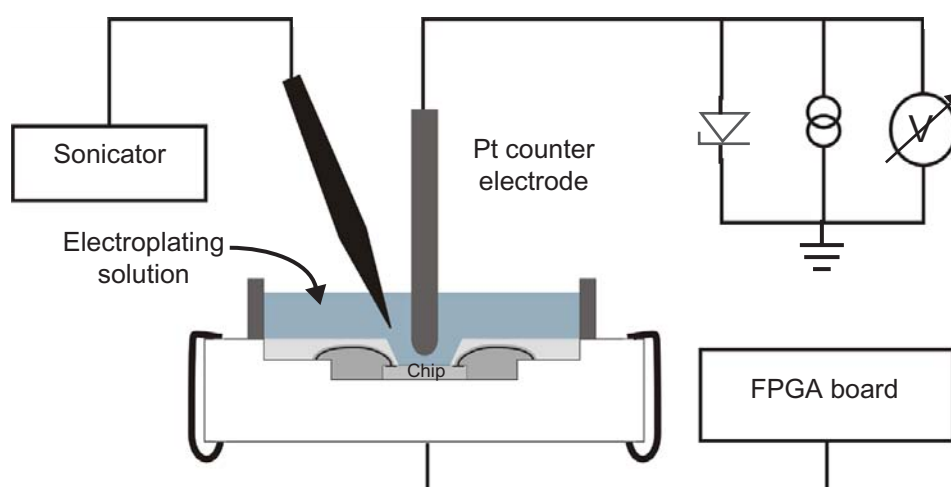


Fig. 5.2: Photographs of the 1<sup>st</sup> generation (top) and 2<sup>nd</sup> generation chips (bottom) used in this work.

### 5.1.2 PLATINIZATION

Deposition of platinum black is performed using the experimental apparatus shown in Fig. 5.3. Dendritically structured Pt black is electrochemically deposited on the electrodes by applying a current density of  $1 \text{ nA}/\mu\text{m}^2$  for 60 sec. in a solution containing 7mM hexachloroplatinic acid, 0.3 mM lead acetate and hydrochloric acid to adjust the pH to close to 1.0 [Borkholder 1998]. The relatively high current density is required to operate the electrochemical cell in mass-transport-controlled distribution mode. This ensures that the metal forms dendritic structures.



*Fig. 5.3: Experiment apparatus for the platinization process. An FPGA board was used to stimulate the entire electrode array with a constant 1.0 - 1.5 V signal. The  $1 \text{ nA}/\mu\text{m}^2$  current density was delivered to electrode array for 60 sec. by a universal source generator via a Pt counter electrode. The zener diode ( $V_{\text{breakdown}} = 6.0 \text{ V}$ ) connected in series to the current source protects the chip from high voltages which may be produced by the current source. A voltmeter was used to monitor the voltage applied to the chip.*

In the set-up used here, a current source (HP 3245A) supplies the appropriate current density to the electrode array via a Pt counter electrode. At the same, all the electrodes are set to 1.0 - 1.5 V using the stimulation circuitry and a printed circuit board outfitted with a field-programmable-gate-array (FPGA) controller. As a safety precaution, a zener diode is connected in parallel to the source generator, which would produce voltages high enough to destroy the CMOS circuitry if the current set-point is not reached (for example if the stimulation circuitry was

not working properly, blocking the flow of current). The voltage applied to the chip is continuously monitored using a voltmeter. For robust Pt black deposits, sonication was used. Fig. 5.4 shows electrodes platinized with (left) and without (right) sonication. From the high-magnification images of platinized electrodes with and without sonication (bottom images in Fig. 5.4), it is apparent that sonication leads to irregularly shaped deposits.

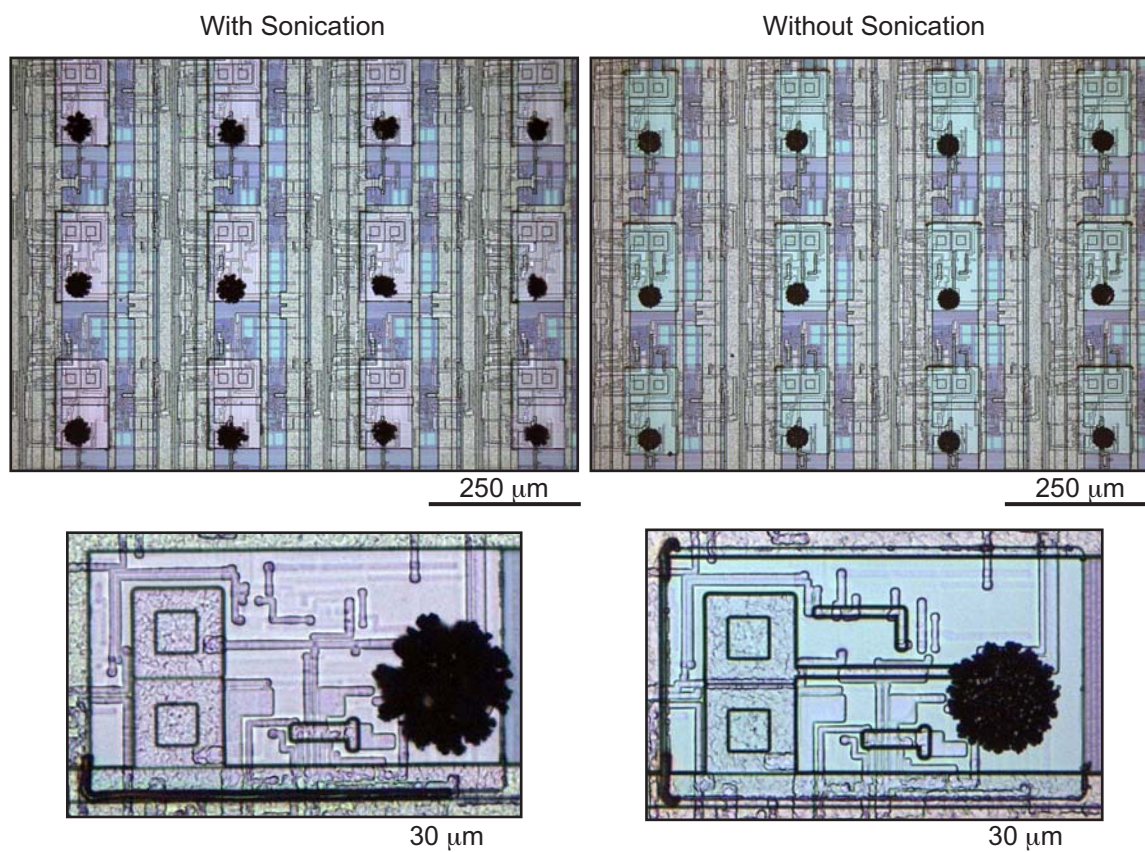


*Fig. 5.4: Platinum black deposits with sonication (left) and without (right). High-magnification images (bottom) show that sonication results in dense, tubular structures.*

## 5.2 ELECTROPHYSIOLOGICAL RECORDINGS WITH 1<sup>ST</sup> GENERATION CMOS CHIP

In the case of the 1<sup>st</sup> generation chip, electrophysiological recordings based on organ culture - meaning a portion of undisaggregated heart tissue is cultured on

the chip - were performed. Hearts from embryonic day 10 chickens were extracted, rinsed with Dulbecco's PBS (Sigma-Aldrich, U.S.A.), and placed on the active area of the chip. A typical spike is presented in Fig. 8 of Appendix B.

Recordings based on dissociated neural cell cultures were attempted, however measurement attempts were unsuccessful due to a circuitry design flaw. In the case of the 1<sup>st</sup> generation chip, low-pass filtering and amplification were performed prior to high-pass filtering. Electrochemical drift and offset arising from the solid-liquid interface caused this first signal-conditioning stage to saturate, precluding the measurement of signals. Nevertheless, cell culturing with the 1<sup>st</sup> generation chip led to valuable insight into the passivation stability and the shifted-electrode design presented in Chapter 3. In the case of the 2<sup>nd</sup> generation chip, the signal was first AC coupled, to filter out drift.

### 5.3 ELECTROPHYSIOLOGICAL RECORDINGS WITH 2<sup>ND</sup> GENERATION CMOS CHIP

#### 5.3.1 CARDIOMYOCYTE RECORDINGS

Electrophysiological recordings were first made from spontaneously beating neonatal rat cardiomyocytes. Fig. 5.5 (top) shows a typical spike train and a high-resolution single spike (bottom). Cells were prepared and cultured according to the protocol given in Sec. 3.4. Recordings were performed at 4 - 5 days *in vitro* (DIV). To stimulate activity, phenylephrine (Sigma) was added to the maintenance medium (end concentration of 0.1 mM) approximately 1 - 2 hours prior to recording. At 6 - 8 DIV the cells tended to delaminate from the surface, probably due to the absence of necessary chemicals, such as hormones, from the medium. Experimental details are summarized in Tab. 5.3 at the end of this chapter.

The signal has the expected biphasic waveform, similar to those described in Sec. 2.1. and to those recorded from mammalian cardiomyocytes reported in literature [Kucera *et al.*, 2000, Halbach *et al.*, 2003]. The slight deviation from the waveform presented in Fig. 2.11 (left), it believed to be a result of the different cell types (embryonic mouse versus neonatal rat cardiomyocytes). A typical recorded spike amplitude of 1.8 mV and a spike duration of  $\sim 2$  ms is consistent with spikes reported in literature. A comparison between the spikes reported here and those reported in literature, measured with a microelectrode array (MEA, a chip without circuitry), is given in Tab. 5.2. The table shows that the spike ampli-

tude and duration varies significantly with cell type. Spikes recorded from embryonic mouse cardiomyocytes are much smaller and longer than those recorded from NRC's. For comparison with the neural recordings, the experiment parameters and results are given in Tab. 5.3.

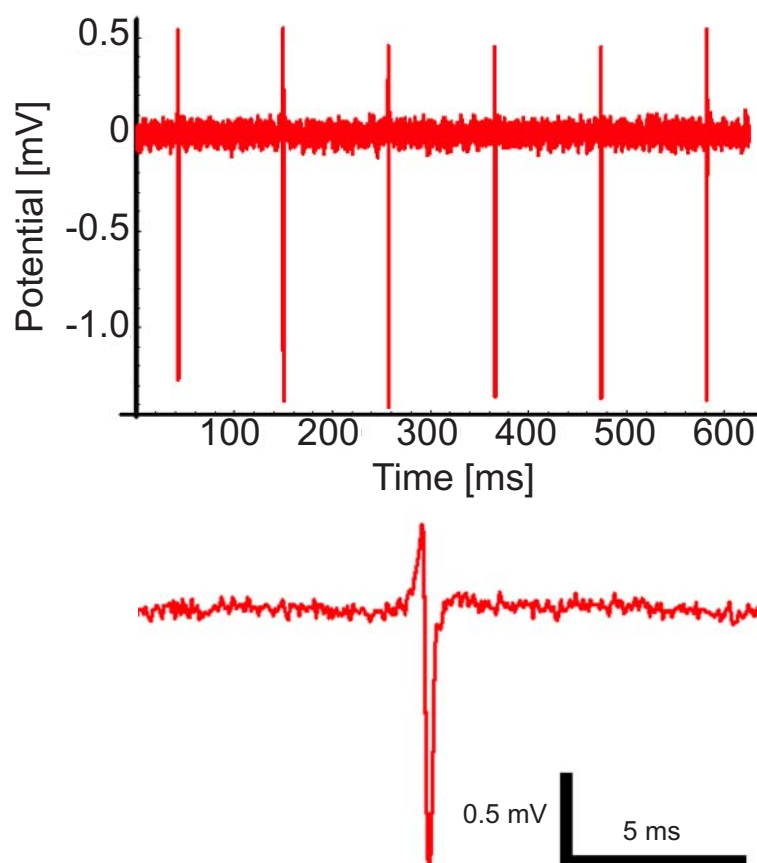


*Fig. 5.5: Electrophysiological recordings from neonatal rat cardiomyocytes. The top graph shows rhythmic spike trains, and the bottom graph shows the waveform of a typical field potential. The waveform has the expected biphasic spike described in Sec. . Raw, unamplified data is presented.*

Tab. 5.2: Comparison between electrophysiological recordings from cardiomyocytes measured using the CMOS chip and recordings performed with a microelectrode array (MEA, without circuitry) published in literature.

Property	CMOS Chip	MEA 1	MEA 2
Cell Type	Neonatal rat cardiomyocyte	Neonatal rat cardiomyocyte	Embryonic mouse cardiomyocyte
Culture Type	Cell	Cell	Cell
Age of Culture at Time of Recording [days <i>in vitro</i> ]	4 - 5	2 - 7	1 - 3
Typical Signal Amplitude [mV]	1.8	> 1.0	0.15
Typical Spike Duration [ms]	2	2	100
Electrode Diameter [ $\mu\text{m}$ ]	30	30	30
Reference	-	Kucera <i>et al.</i> , 2000	Halbach <i>et al.</i> , 2003

### 5.3.2 NEURAL RECORDINGS

Once the measurement system had been developed using the cardiac myocytes, recordings were made with neural cell cultures. Fig. 5.6 shows spikes recorded from cortical neurons from embryonic day 10 chickens using 30- $\mu\text{m}$  (left) and 40- $\mu\text{m}$  (right) diameter platinized electrodes. A high-resolution graph of a typical spike recorded with each electrode is shown in the bottom row of the figure. Field potentials recorded with the larger electrode have a slightly smaller amplitude and are noisier than those recorded with the smaller electrode. Although thermal

noise decreases with increasing electrode size, a noisier signal was recorded with the larger electrode presumably because the electrode is not entirely covered by the cell. As a result, the electrode is prone to noise fluctuations introduced by the medium. Furthermore, signal leaks to the surrounding medium account for the slightly smaller spike sizes.

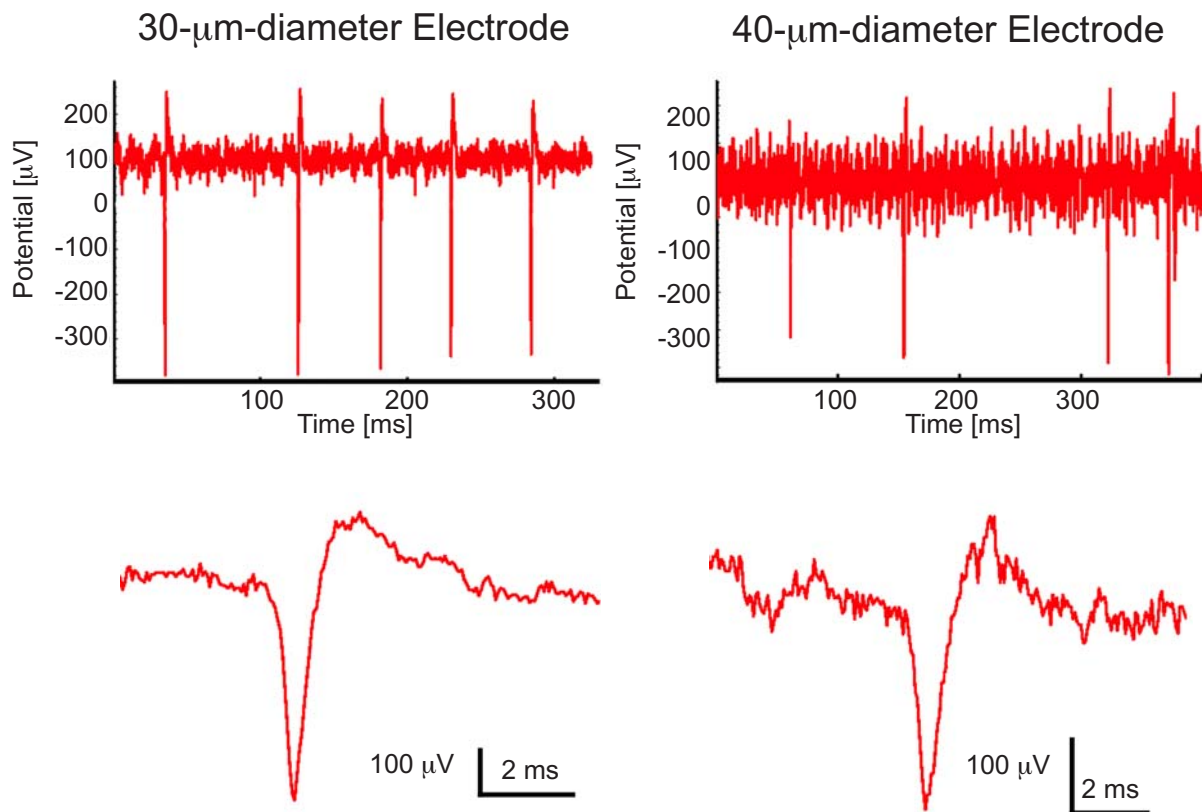


*Fig. 5.6: Electrophysiological recordings from embryonic chicken neural cell cultures (56 DIV). Spikes were measured with 30- $\mu\text{m}$  (left) and 40- $\mu\text{m}$ -diameter (right) electrodes.*

A comparison between the signals reported here and those found in literature is difficult due to the paucity of data available from chick neurons. In one article from Jimbo and Kawana reports on both chick and mouse dorsal root ganglions, however the cell type is not correlated to the results (Jimbo and Kawana, 1992). In general, the spike size, 500 - 600  $\mu\text{V}$ , has the same order of magnitude as signals recorded from mammalian cell cultures (200 - 300  $\mu\text{V}$ , neonatal rat cortical neurons, Jimbo *et al.*, 2000). Similarly, the spike duration,  $\sim 5$  ms, is consistent

with other studies ( $\sim 5$  ms, Jimbo *et al.*, 2000). As above, a summary of the experiment parameters, and results, is given in Tab. 5.3.

*Tab. 5.3: Summary of electrophysiology experiment parameters and results.*

Property	NRC Recordings	Neural Recordings
Electrode Diameter [ $\mu\text{m}$ ]	30	30 and 40
Platinization	no	yes
Band-pass Filter [Hz]	10 - 5,000	10 - 5,000
Typical Spike Size [mV]	1.8	0.6 and 0.5 <sup>a</sup>
Spike Duration [ms]	2.5	3 - 4
Culture Age [DIV]	4 - 5	56

a. For the 30- and 40- $\mu\text{m}$ -diameter electrodes respectively.

## 5.4 SUMMARY AND CONCLUSIONS

The heart of the recording system, the CMOS chip, is presented in this chapter. Although the 1<sup>st</sup> generation design was of limited use for electrophysiological measurements, it was nevertheless instrumental in gaining experience preparing the CMOS chip for the liquid cell-culture environment. To minimize expenses, this first chip was produced on a multi-project wafer run, meaning that single, diced chips were received from the foundry. With the experience gained through the testing and characterization of this first chip, it was economically feasible to produce the 2<sup>nd</sup> generation chip at the wafer level.

The 2<sup>nd</sup> generation chip was successfully used to measure electrophysiological signals from both neural and cardiomyocyte cell cultures. The recorded spikes were similar to those reported in literature. Now that it has been established that



the system is capable of recording signals, more interesting, biology-related experiments, such as drug testing, may be attempted.

## 5.5 REFERENCES

Borkholder, D. A. (1998). "Cell based biosensors using microelectrodes," Stanford University.

DeBusschere, B. D., and Kovacs, G. T. A. (2001). "Portable cell-based biosensor system using integrated CMOS cell-cartridges." *Biosensors-&Bioelectronics*, 16(7-8), 543-56.

Eversmann, B., Jenkner, M., Paulus C., Hofmann, F., Brederlow, R., Fromherz, P., Brenner, F., Schreiter, M., Gabl, R., Plehnert, K., Steinhauser, M., Eckstein, G., Schmitt-Landsiedel, D., Thewes, R. "A 128 x 128 CMOS bio-sensor array for extracellular recording of neural activity." 2003 IEEE International Solid-State Circuits Conference, 222-223.

Halbach, M., Egert, U., Hescheler, J., and Banach, K. (2003). "Estimation of action potential changes from field potential recordings in multicellular mouse cardiac myocyte cultures." *Cell Physiol Biochem*, 13(5), 271-84.

Jimbo, Y., and Kawana, A. (1992). "Electrical-Stimulation and Recording from Cultured Neurons Using a Planar Electrode Array." *Bioelectrochemistry and Bioenergetics*, 29(2), 193-204.

Jimbo, Y., Kawana, A., Parodi, P., and Torre, V. (2000). "The dynamics of a neuronal culture of dissociated cortical neurons of neonatal rats." *Biological Cybernetics*, 83(1), 1-20.

Kandel, E. R., Schwartz, J. H., Jessell, T. M. (2000). *Principles of Neural Science*, McGraw-Hill, London.

Kim, C., and Wise, K. D. (1996). "A 64-site multishank CMOS low-profile neural stimulating probe." *Ieee Journal of Solid-State Circuits*, 31(9), 1230-1238.

Pancrazio, J. J., Bey, R. P., Jr., Loloee, A., Manne, S., Chao, H. C., Howard, L. L., Milton-Gosney, W., Borkholder, D. A., Kovacs, G. T. A., Manos, P., Cuttino, D. S., and Stenger, D. A. (1998). "Description and demonstration of a CMOS amplifier-based-system with measurement and stimulation capability for bioelectrical signal transduction." *Biosensors and Bioelectronics*, 13(9), 971-9.

Stett, A., Egert, U., Guenther, E., Hofmann, F., Meyer, T., Nisch, W., and Haemerle, H. (2003). "Biological application of microelectrode arrays in drug discovery and basic research." *Anal Bioanal Chem*, 377(3), 486-95.

Stieglitz, T., Schuettler, M., and Koch, K. P. (2004). "Neural prostheses in clinical applications--trends from precision mechanics towards biomedical microsystems in neurological rehabilitation." *Biomed Tech (Berl)*, 49(4), 72-7.

# 6 CONCLUSIONS AND OUTLOOK

## 6.1 CONCLUSIONS

In this thesis a cell-based biosensor system has been investigated. The system is based upon a CMOS chip comprising a microelectrode array as well as stimulation and recording circuitry. Post-processing was used to realize biocompatible, transducing electrodes and to achieve chip stability that sustains 200 days in a culture environment. A technique for site-selective cell adhesion based on the selective molecular assembly patterning technique was developed and combined with the CMOS chip. The functionalized surface defines the location of cell adhesion for at least 5 days for neonatal rat cardiomyocytes and for at least 21 days for a neuronal/glia cell culture. Electrophysiological recordings have been made using the CMOS chip from cell cultures of cardiomyocytes and neurons.

### 6.1.1 THE CMOS ADVANTAGE

Throughout the course of this research, the question was often raised why CMOS? The conclusion from this study is it depends on the applications. CMOS possesses some very useful advantages, in particular multiplexing, leading to large array sizes, and on-chip processing capabilities. In the field of computational neuroscience, the goal is to harness the power of parallel processing in neuronal networks for information processing. In this case, one criteria is as many ‘contacts’ to the network as possible, which are used to ‘program’ the culture. The greater the number of inputs/outputs, the more powerful the computation abilities. Without multiplexing, the number of electrodes is limited to the number of interconnects to the outside world (e.g. commercial systems typically offer 64 electrodes).

With a large number of electrodes comes vast amounts of data. Consider 1,000 electrodes recording at a modest 20 ksamples/s. In one second, 20 Msamples have been recorded. This generates 20 Mbytes of data, per second, when converted into a digital signal using an 8-bit ADC. An average 200 Gbyte hard drive

would be filled in 170 min. of recording time; not a short recording period considering in some cases the goal is to study the evolution of culture activity over weeks and months. Furthermore, manipulating (saving and transferring) such large amounts of data becomes cumbersome. On-chip circuitry could be used to implement on-chip data mining algorithms to reduce the amount of data. For example, circuitry could be used to detect field potential events and the chip output becomes event frequency.

Conversely a case can be made for not using CMOS. CMOS is relatively expensive to develop and post-processing is complex. If electrophysiological recordings are to be combined with measurements based on fluorescence, for example in systems-biology inspired investigations, a transparent substrate may be required. If only a few measurement point are necessary, the cost of a CMOS system may not be justifiable. Finally, the complexity of working with a CMOS chip may preclude its wide-spread use by biologists.

### 6.1.2 *IN VITRO* VERSUS *IN VIVO*

Cells cultured *in vitro* are not exactly the same as the same cell *in vivo*. The three-dimensional structure is lost, and chemical signals, such as hormones, are missing. Be this at it may, the cells still behave in a physiologically similar way. The neuron still exhibit an integrate-and-fire mechanism and the heart muscle cell still develop myofibrils. It can be concluded that *in vitro* experimental is indicative of the *in vivo* response, although greatly simplified. Simplification may be advantageous when the aim is to identify response mechanisms. However, to produce the most valuable results, findings must be benchmarked with *in vivo* studies.

## 6.2 OUTLOOK

Much work can be done to improve upon the system presented here. The functionalized surface should be tested with neuronal/glia co-cultures to study pattern fidelity and cell differentiation. A new surface chemistry could be developed where antibodies specific to certain cell parts, i.e. dendrites and cell body, are patterned to create precisely-defined neuronal networks. Electrophysiological measurements from patterned cells is needed to show the next stage of system integration.

Biosensing itself is yet to be demonstrated. Simple drug experiments to alter the signal waveform or frequency can be envisioned. To provide stable environment conditions, such experiments would require a measurement system that can be placed in the incubator, or, conversely, a packaging system that regulates culture temperature and medium pH itself, obviating the need for an incubator. This leads to ideas of integration with other components, such as microfluidics. A partner institute has produced a microfluidic system to be used with the 2<sup>nd</sup> generation CMOS chip. It comprises inlet ports to perfuse rows of electrodes with unique chemical signals. The advantage of such a system is that the effect of different chemical cues can be simultaneously tested, and conclusions drawn from comparisons free of inter-culture variability.

### **6.2.1 COMMERCIAL POTENTIAL**

In the more distant future, such a system could be developed for commercial use in the pharmaceutical industry, as was mentioned in the introduction. A commercial venture requires both a clear advantage over existing methods and a large, growing market. The first condition is potentially satisfied by the whole-cell response of the MEA, the simplicity of the measurement technique and by the array size (i.e. many simultaneous measurement sites). In contrast, the patch-clamp technique is time-consuming and complicated. It takes two scientists one day to perform 10 to 12 experiments and many tests are predicted to be needed in the development of drugs affecting ion channels. In 2005, it is estimated that 10 - 50 ion channel targets will be tested by a large size pharmaceutical company per year. Per ion channel target, one million compounds need to be examined. This is a massive experiment volume that will be difficult to satisfy using traditional technologies. Furthermore, the market for ion channel analysis technologies is thought to be USD 500 million, and growing at a rate of 20% per annum.



---

# APPENDIX A

## IMPEDANCE CHARACTERIZATION AND MODELING OF ELECTRODES FOR BIOMEDICAL APPLICATIONS

W. Franks, I. Schenker, P. Schmutz\*, A. Hierlemann

Physical Electronics Laboratory, Swiss Federal Institute of Technology (ETH),  
Zurich, 8092, Zurich, Switzerland

\* Laboratory for Corrosion and Materials Integrity, Swiss Federal Institute for  
Materials Testing and Research (EMPA), 8600, Duebendorf, Switzerland

Published in: IEEE Transactions on Biomedical Engineering, 2005 (in print)

# Impedance Characterization and Modeling of Electrodes for Biomedical Applications

Wendy Franks\*, Iwan Schenker, Patrik Schmutz, Andreas Hierlemann

**Abstract**— A low electrode-electrolyte impedance interface is critical in the design of electrodes for biomedical applications. To design low-impedance interfaces a complete understanding of the physical processes contributing to the impedance is required. In this work a model describing these physical processes is validated and extended to quantify the effect of organic coatings and incubation time. Electrochemical impedance spectroscopy has been used to electrically characterize the interface for various electrode materials: platinum, platinum black, and titanium nitride; and varying electrode sizes:  $1 \text{ cm}^2$ , and  $900 \mu\text{m}^2$ . An equivalent circuit model comprising an interface capacitance, shunted by a charge transfer resistance, in series with the solution resistance has been fitted to the experimental results. Theoretical equations have been used to calculate the interface capacitance impedance and the solution resistance, yielding results that correspond well with the fitted parameter values, thereby confirming the validity of the equations. The effect of incubation time, and two protein coatings, poly-L-lysine and laminin, on the interface impedance has been quantified using the model. This demonstrates the benefits of using this model in developing a better understanding of the physical processes occurring at the interface in more complex, biomedically relevant situations.

**Index Terms**— Electrochemical impedance spectroscopy, Pt, Pt black and TiN bioelectrodes

## I. INTRODUCTION

Impedance characterization of the electrode-electrolyte interface is of paramount importance in the fields of impedance-based biosensing, neuroprotheses and in vitro communication with electrogenic cells. In impedance-based biosensing, changes in the impedance are correlated to cell spreading and

locomotion [1], to bacterial growth [2], to DNA hybridization [3] and to antigen-antibody reactions [4]. Neuroprotheses, and in particular cochlear implants, represent an important application of impedance characterization. The current applied to stimulate hearing via a cochlear implant is determined from the known electrode impedance [5], which is designed to be as low as possible to avoid cell damage [6]. For the extracellular, in vitro monitoring of electrogenic cells, where small microelectrodes are required for high-resolution stimulation and recording, the need for a low interface impedance is two-fold [7] - [10]. During stimulation a certain current density is necessary to generate activity. A high impedance would result in a large applied electrode voltage leading to undesirable electrochemical reactions that may be harmful to cellular cultures. On the recording side, the extracellular signals are low, on the order of millivolts for cardiomyocytes and microvolts for neurons. The neural signals will be lost in the noisy, ion-based electric fluctuations of the surrounding electrolyte media if the electrode impedance is not low enough. A well-characterized, fully understood interface impedance leads to an optimized electrode-electrolyte interface design.

Equivalent circuit models have long been used to model the interface impedance. In 1899 Warburg first proposed that the interface could be represented by a polarization resistance in series with a polarization capacitor [11]. Experimental findings soon revealed that the polarization capacitance exhibited a frequency dependency leading to the introduction of Fricke's law [12], and the use of a constant phase angle impedance to represent the impedance of the interface capacitance. Randles' work with rapid electrode reaction systems resulted in the well-known Randles model, consisting of an interface capacitance shunted by a reaction impedance, in series with the solution resistance [13]. As the use of platinum electrodes in medical applications became ubiquitous, more research was dedicated to the understanding of the electrode - physiological solution interface. In the case of platinum, the resistive element due to faradaic current was often omitted as measurement equipment was not able to measure at low frequencies where the impedance is finite, and not infinite, as was typically assumed [14]. The work of Schwan and co-workers expanded on previous work to include low frequency considerations [15]. Of particular importance to biomedical applications is Schwan's limit of linearity: the voltage at which the electrode system's impedance becomes non-linear, which is often exceeded during stimulation [16], [17]. McAdams and colleagues extensively studied the platinum pacing electrode (90 % platinum and 10 % iridium) in physiological saline, successfully interpreting the frequency dependent non-linear interface impedance [18] - [20]. Kovacs has presented an equivalent circuit model based on the Randles model, with an additional Warburg impedance due to the diffusion of faradaic current [7].

Manuscript received April 13, 2004. Financial support is generously provided by the Information Societies Technology (IST) European Union Future and Emerging Technologies program, and the Swiss Bundesamt für Bildung und Wissenschaft (BBW). *Asterisk indicates corresponding author.*

W. Franks and A. Hierlemann are with the Physical Electronics Laboratory, ETH, Zurich, 8093, Zurich, Switzerland (phone: +41 1 633 39 28; fax: +41 1 633 10 54; e-mail: [franks@iqe.phys.ethz.ch](mailto:franks@iqe.phys.ethz.ch); [hierlema@iqe.phys.ethz.ch](mailto:hierlema@iqe.phys.ethz.ch)).

I. Schenker was with the Physical Electronics Laboratory, ETH, Zurich, and is now with the Nonmetallic Inorganic Materials group, ETH Zurich, 8093, Zurich, Switzerland (email: [iwan.schenker@mat.ethz.ch](mailto:iwan.schenker@mat.ethz.ch)).

P. Schmutz is with the Laboratory for Corrosion and Materials Integrity, Swiss Federal Institute for Materials Testing and Research (EMPA), 8600, Dübendorf, Switzerland (email: [Patrik.Schmutz@empa.ch](mailto:Patrik.Schmutz@empa.ch)).



In the work presented here, electrochemical impedance spectroscopy (EIS) has been used to characterize the electrode-electrolyte interface for various electrode materials commonly used in biomedical applications: platinum, platinum black and titanium nitride. An equivalent circuit model has been used where each parameter represents a macroscopic physical quantity contributing to the interface impedance: The model consists of an interface capacitance, shunted by a charge transfer resistance, in series with the solution resistance. The model parameters have been fitted to the experimental results. To confirm that the parameters do indeed represent the physical quantities, theoretical equations have been used to calculate the parameter values thereby validating the model. With respect to the measurement technique, the effect of the initial interface conditions on the charge transfer resistance is demonstrated. Measurements have been performed for  $1 \text{ cm}^2$  bright Pt, Pt black and TiN, and for  $900 \mu\text{m}^2$  Pt black. As an extension to models that have been presented in the past [5, 7, 20], this model has been used to quantify the effect of organic cell-adhesion promoting coatings, such as poly-L-lysine (PLL) and laminin, and the effect of incubation time on the interface impedance. This demonstrates the use of the model to develop a complete understanding of the physical processes occurring at the interface in more complex, biomedically relevant situations.

## II. METHODS

Both the macro- and microelectrodes were produced in-house according to the following procedures. For the macroelectrodes a bare p-type Si wafer was electrically isolated with 100 nm  $\text{SiO}_2$  followed by 500 nm of  $\text{Si}_3\text{N}_4$  deposited using plasma enhanced chemical vapor deposition (PECVD). Sputter deposition was used to coat the substrate with 50 nm of TiW, an adhesion promoter, followed by 270 nm of Pt. The wafer was then diced and cleaned. The chips were then either coated with Pt black or TiN. Pt black was deposited using a 0.3 - 10 A/cm<sup>2</sup> current density in a solution containing 7 mM hexachloroplatinic acid, 0.3 mM lead acetate and hydrochloric acid to adjust the solution pH to 1.0. Dendritically structured TiN was vapor deposited by the Naturwissenschaftliche und Medizinische Institut at the University of Tübingen, Germany [21]. For the microelectrodes a p-type Si wafer with 100 nm of  $\text{SiO}_2$  and 500 nm of  $\text{Si}_3\text{N}_4$  was used as the substrate. As above, 50 nm TiW and 270 nm Pt were sputter deposited, and the microelectrodes with leads and bond pads were structured in a lift-off process. The wafer was passivated with 500 nm  $\text{Si}_3\text{N}_4$ . A reactive-ion etch (RIE) was used to open the electrodes, thereby defining their size and shape. The chips were then diced and cleaned. The bond wires of the packaged chips were encapsulated in polydimethylsiloxane (PDMS) for electrical isolation.

Bright Pt macroelectrodes were coated with two different protein coatings, laminin and poly-L-lysine, in the following manner. The samples were cleaned with an air plasma treatment (2 min. at  $\sim 3.0(10)^{-2}$  mbar). It is known from x-ray photon spectroscopy (XPS) measurements that, immediately following plasma cleaning, the surface contains no carbon, indicating that the surface is free of organic residues. Additionally, plasma cleaning has the effect of activating the surface and is believed to lead to better quality protein layers with respect to coverage and adhesion. Within 45 minutes of plasma cleaning the protein coatings were applied. Samples were incubated (37°C, 5 %  $\text{CO}_2$ ) overnight in laminin (20 mg/ml phosphate buffered saline, PBS). For PLL the samples were incubated for 30 minutes in a 0.05 %

solution. After incubation the samples were rinsed three times with PBS.

To investigate the effect of time on the interface impedance, bright Pt samples were incubated in medium containing 10% horse serum. Impedance measurements were performed after 7, 14 and 35 days using neuron medium with serum as the electrolyte.

Measurements were performed using a commercially available Autolab PGSTAT30 potentiostat system with Frequency Response Analysis software (version 4.9, Eco Chemie B.V., Netherlands). In this three-electrode system, a standard calomel electrode (SCE) is the reference electrode, the counter electrode is large-area Pt, and the electrolyte is physiological saline, 0.9 % NaCl. In addition to the time dependency measurements, neuron medium with 10% horse serum was used as the electrolyte in one set of measurements. The perturbation potential was 10 mV and the scan range was  $10^{-3}$  to  $10^5$  Hz, unless otherwise noted. Measurements were typically performed with respect to the open-circuit potential (OCP), the potential naturally occurring between the working and reference electrodes. The OCP is a function of the chemical composition of the interface, and can significantly affect the impedance results. Accordingly, special attention was paid to the preparation of the samples to ensure that the interface was as defined as possible. It is known that organic residues on the substrate surface can contribute to a faradaic current, which decreases the charge transfer resistance and polarizes the electrode. An in situ cleaning process was therefore used where the Pt and Pt black electrodes (without coatings) were treated by voltammetric cycling from -1.0 to 1.0 V for typically 6 cycles, at which point the measurement stabilized. Cyclic voltammetry potentially results in the formation and reduction of Pt oxide and Pt dioxide layers, as indicated by the Pt-H<sub>2</sub>O Pourbaix diagram [22]. Since the OCP is a function of the interface composition, the OCP can be altered through the cycling process. Additionally, the OCP can be used as a quality control to ensure that the initial conditions are the same from measurement to measurement. The average OCP values for Pt, Pt black and TiN were  $0.318 \pm 0.037$ ,  $0.299 \pm 0.061$ , and  $0.046 \pm 0.034$  V respectively. The relatively large range of OCP values for TiN can be attributed to the fact that the samples were not treated with cyclic voltammetry for fear of damaging the dendritic structure.

Measurements were first performed with relatively large area samples ( $1 \text{ cm}^2$ ) to establish the measurement technique and equivalent circuit model under stable experimental conditions. Difficulties with respect to stability were encountered during the measurement of the microelectrodes as the current approached the system measurement limit of 10 nA at low frequencies. As a result, the frequency range for the microelectrode measurements was reduced to  $10^{-2}$  to  $10^5$  Hz.

## III. EQUIVALENT CIRCUIT MODEL

The equivalent circuit model presented in this work comprises a constant phase angle impedance  $Z_{CPA}$ , that represents the interface capacitance impedance, shunted by a charge transfer resistance  $R_{ct}$ , together in series with the solution resistance  $R_S$ , see Fig. 1 [23]. This model is an adaptation from the theoretical models typically used to represent the electrode-electrolyte impedance [7], [19], [24]. The Warburg impedance due to diffusion of the chemical reactants in solution is not included in this model. For the materials and frequency range employed here, it was experimentally determined that the Warburg impedance does not significantly contribute to the overall impedance.

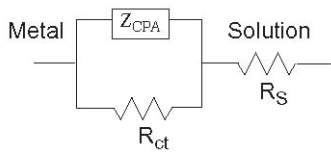


Fig. 1: Equivalent circuit model of electrode-electrolyte interface.

### A. Interface Capacitance

The constant phase angle impedance is a measure of the non-faradaic impedance arising from the interface capacitance, or polarization, and is given by the empirical relation [20]:

$$Z_{CPA}(\omega) = \frac{1}{(j\omega Q)^n} \quad (1)$$

where  $Q$  is a measure of the magnitude of  $Z_{CPA}$ ,  $n$  is a constant ( $0 \leq n \leq 1$ ) representing inhomogeneities in the surface and  $\omega = 2\pi f$ . In a Nyquist plot the angle between the data and the abscissa axes gives  $n$  according to  $n = (2\theta)/\pi$ . When  $n=1$ ,  $Z_{CPA}$  represents a purely capacitive impedance element corresponding to the interface capacitance.

A theoretical derivation of the interface capacitance is given by the Gouy-Chapman-Stern model (GCS) [25]. The interface capacitance is taken to be the series combination of the double-layer capacitance, termed the Helmholtz capacitance  $C_H$ , and the diffuse layer capacitance, the Gouy-Chapman capacitance  $C_G$ , and is given by the following formula:

$$\frac{1}{C_I} = \frac{1}{C_H} + \frac{1}{C_G} = \frac{d_{OHP}}{\epsilon_0 \epsilon_r} + \frac{L_D}{\epsilon_0 \epsilon_r \cosh\left(\frac{z\phi_0}{2U_t}\right)} \quad (2)$$

where  $d_{OHP}$  is the thickness of the double-layer,  $\epsilon_0$  is the permittivity of free space,  $\epsilon_r$  is the permittivity of the double layer,  $z$  is the charge on the ion in solution,  $\phi_0$  is the applied electrode potential, and  $U_t$  is the thermal voltage. The Debye length,  $L_D$ , is given by:

$$L_D = \sqrt{\frac{\epsilon_0 \epsilon_r U_t}{2n^0 z^2 q}} \quad (3)$$

where  $n^0$  is the bulk number concentration of ions in solution and  $q$  is the elementary charge. See Tab. 1 for the values of the constants and variables used here.

TABLE I  
SUMMARY OF THE VALUES USED FOR VARIABLES AND CONSTANTS USED TO CALCULATE THE THEORETICAL VALUE OF CI USING EQN. 2. IN THE 'NOTE' COLUMN ALL ASSUMPTIONS ARE GIVEN.

Parameter	Value	Note
$d_{OHP}$	5 Å	Physiological saline at 25 °C [7]
$\epsilon_0$	$8.85(10)^{12}$ F/m	
$\epsilon_r$	78	Dilute aqueous solution at 25 °C [25]
$z$	4	O <sub>2</sub> reduction reaction [29]
$U_t$	0.0259 V	
$n^0$	$9.3(10)^{25}$ ions/m <sup>3</sup>	Physiological saline at 25 °C
$q$	$1.602(10)^{-19}$ C	

### B. Equilibrium Exchange Current Density and $R_{ct}$

At equilibrium, equal and opposite reduction and oxidation currents flow across the electrode-electrolyte interface. The magnitude of these currents is termed the equilibrium exchange current density  $J_0$  and is given by:

$$J_0 = Fk_c c_A e^{(-\beta F \Delta\phi_0)/(RT)} \quad (4)$$

for the reduction reaction where  $F$  is Faraday's constant,  $k_c$  is

reduction reaction rate constant,  $c_A$  is the concentration of electron-acceptor ions A in solution plane of the interface,  $\beta$  is the symmetry factor,  $\Delta\phi_0$  is the equilibrium potential,  $R$  is the gas constant and  $T$  is the temperature [26]. The equilibrium current is a measure of the electrode's ability to participate in exchange current reactions, and hence is of particular relevance to this work. For an ideally polarizable electrode  $J_0$  equals zero and for an ideally unpolarizable electrode  $J_0$  tends to infinity; in reality,  $J_0$  lies somewhere between these two extremes. It is tempting to use literature values of  $J_0$  to compare various electrode materials, however since  $J_0$  is a function of ion concentration and temperature, literature values must be carefully considered.

The equilibrium exchange current and  $R_{ct}$  can be experimentally determined through the application of the low-field approximation to the Butler-Volmer equation ( $\eta < 0.005/z$ ), which yields:

$$J = \frac{J_0 F \eta}{RT} \quad (5)$$

where  $J$  is the measured current density,  $\eta$  is the applied overpotential,  $z$  is the number of electrons involved in the redox reaction, and  $RT/F = 26$  mV at 298 K. Under the low-field approximation, the Butler-Volmer equation reduces to Ohm's law. A plot of the current versus overpotential yields a straight line and the charge transfer resistance is given by the slope as  $R_{ct} = RT/(J_0 z F)$ . Cyclic voltammetry was used to determine  $J_0$  under the following conditions: 5 mV perturbation signal with respect to the OCP, 0.5 mV/s scan rate, 0.15 mV step potential, averaged over 10 scans. For the case of Pt the charge transfer arises from the electrolysis of H<sub>2</sub>O and reduction of O<sub>2</sub> according to  $2H_2O \leftrightarrow O_2 + 4H^+ + 4e^-$  where the equilibrium potential is

$$0.987 - 0.059 \times \text{pH} \quad (6)$$

with respect to the SCE [27]. For the calculation of  $J_0$ ,  $z$  was therefore assumed to be 4. It should be noted that the presence of contaminants at the interface will also contribute to the faradaic current.

### C. Solution Resistance

The resistance measured between the working electrode and the reference electrode is termed the solution resistance. It can be determined from the spreading resistance, the resistance encountered by current spreading out into solution, under the assumption that the counter electrode is infinitely large and the working electrode is surrounded by electrolyte. The spreading resistance is given by:

$$R_s = \frac{\rho \ln 4}{\pi l} \quad (7)$$

for square electrodes ( $\rho$  is the solution resistivity, 72 Ωcm for physiological saline [7],  $l$  the electrode side length), and

$$R_s = \frac{\rho}{4r} \quad (8)$$

for round electrodes ( $r$  is the radius) [7]. It is worth noting that unlike  $R_{ct}$  and  $C_I$ , which scale with the total electrode area, the solution resistance is dependent upon the geometric area only (where geometric area refers to the planar two-dimensional area, and not the larger total area which increases with roughness).

## IV. RESULTS

EIS measurements and model results for 1 cm<sup>2</sup> Pt, Pt black and TiN are given in Fig. 2 [28]. Table 2 gives a summary of the averaged, fitted parameter values with corresponding standard

deviations. For  $Q$ ,  $n$  and  $R_s$ , the standard deviation is 10 %, or less, in almost all cases. In the case of  $R_{ct}$  the standard deviation is as high as 110 %. This large standard deviation can be attributed to the high sensitivity of  $R_{ct}$  to the electrode-electrolyte interface conditions. Furthermore,  $R_{ct}$  is extrapolated from the low frequency data which leads to increased uncertainty. The sharply decreasing phase angles at high frequencies is an artifact of the measurement system.

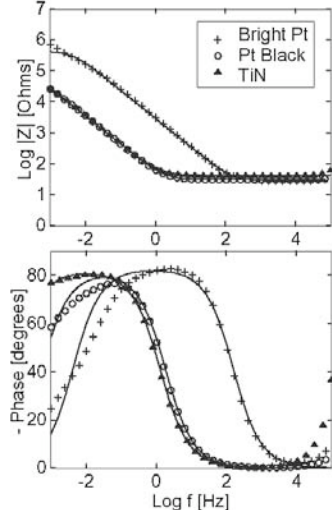


Fig. 2: Impedance modulus and phase as a function of frequency for 1 cm<sup>2</sup> Pt, Pt black and TiN electrode materials [28]. Modeled results are indicated by the smooth lines.

TABLE II

SUMMARY OF THE AVERAGED, FITTED PARAMETER RESULTS, WITH CORRESPONDING STANDARD DEVIATIONS, FOR THE FOLLOWING MATERIALS AND MEASUREMENT AREAS: BRIGHT Pt 1 cm<sup>2</sup>, Pt BLACK 1 cm<sup>2</sup>, TiN 1 cm<sup>2</sup>, Pt BLACK MICROELECTRODE 900 μm<sup>2</sup>, PLL-COATED BRIGHT Pt 1 cm<sup>2</sup>, LAMININ-COATED BRIGHT Pt 1 cm<sup>2</sup>, BRIGHT Pt WITH NEURON MEDIUM AS THE ELECTROLYTE, 1 cm<sup>2</sup>.

	$Q$ [sΩ <sup>-1/n</sup> ]	$n$	$R_s$ [Ω]	$R_{ct}$ [Ω]
Pt	2.72(10) <sup>-5</sup>	0.92	28.0	4.48(10) <sup>5</sup>
Std. dev.	0.26(10) <sup>-5</sup>	0.01	2.81	0.88(10) <sup>5</sup>
Pt black	2.08(10) <sup>-3</sup>	0.91	30.7	5.11(10) <sup>4</sup>
Std. dev.	0.11(10) <sup>-3</sup>	0.03	7.85	2.88(10) <sup>4</sup>
TiN	2.03(10) <sup>-3</sup>	0.91	42.3	3.00(10) <sup>5</sup>
Std. dev.	5.77(10) <sup>-5</sup>	0.00	3.70	3.20(10) <sup>5</sup>
μelectrode Pt black	0.86(10) <sup>-9</sup>	0.86	7.38(10) <sup>3</sup>	2.70(10) <sup>9</sup>
Std. dev.	0.52(10) <sup>-9</sup>	0.02	1.74(10) <sup>3</sup>	1.31(10) <sup>9</sup>
PLL	8.57(10) <sup>-6</sup>	0.91	37.0	1.24(10) <sup>6</sup>
Std. dev.	0.51(10) <sup>-6</sup>	0.01	2.41	0.69(10) <sup>6</sup>
Laminin	5.00(10) <sup>-6</sup>	0.89	28.3	2.46(10) <sup>5</sup>
Std. dev.	2.88(10) <sup>-6</sup>	0.01	5.64	0.68(10) <sup>5</sup>
Neuron Medium	1.46(10) <sup>-5</sup>	0.91	40.4	4.26(10) <sup>5</sup>
Std. dev.	0.18(10) <sup>-5</sup>	0.01	2.30	0.57(10) <sup>5</sup>

### A. Verification of Model Parameters

To confirm the validity of the model, the model parameters have been calculated based on the theoretical principles presented above. A comparison between the fitted and theoretical parameters has been performed for the simplest case of bright Pt. Using Eqn. 2 and the variable values given in Tab. 1, the theoretical interface capacitance was found to be 0.545 mF/m<sup>2</sup>. The impedance of the interface capacitance was calculated using  $Z_{C_I} = (j\omega C_I)^{-1}$ , and at a frequency of 1 Hz,  $|Z_{C_I}|$  is 1.83(10)<sup>4</sup> Ω (for 1 cm<sup>2</sup>). Similarly, using the values of  $Q$  and  $n$  (given in Tab. 2) for 1 cm<sup>2</sup> bright Pt, and Eqn. 1,  $|Z_{CPA}|$  was found to be 1.59 x 10<sup>4</sup> Ω. For  $R_{ct}$ , cyclic voltammetry was used to generate a

current versus overpotential plot, see Fig. 3. From the slope of the plot,  $R_{ct}$  was found to be 300 kΩ; the fitted value was found to be 450 kΩ. From Eqn. 5, the exchange current density was calculated to be 8.5(10)<sup>-8</sup> A/cm<sup>2</sup>. Finally the solution resistance was determined to be 32.0 Ω using Eqn. 8. The fitted parameter value is 28.0 Ω.

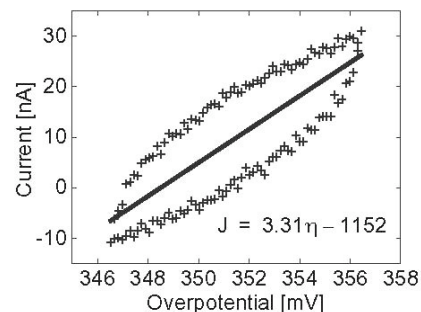


Fig. 3: Equilibrium exchange current density measurement: current versus applied electrode overpotential measurement results for 1 cm<sup>2</sup> bright platinum. A +/- 5 mV overpotential with respect to an OCP of 351.5 mV was applied.

### B. Effect of OCP on Model Results

Throughout the course of this work it has been observed that the model parameter  $R_{ct}$  is highly dependent on the initial electrode-electrolyte interface conditions. To demonstrate this dependance the OCP was set to various values, either by cyclic voltammetry or by an applied potential. The EIS phase results (the modulus results show no variation) and the fitted values for  $R_{ct}$  are given in Fig. 4.

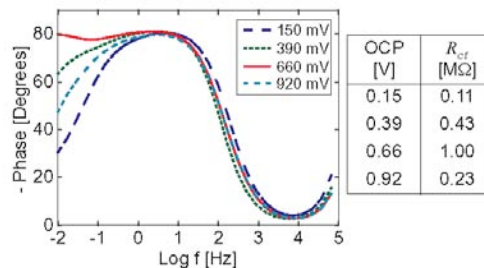


Fig 4: Effect of OCP on measurements results. Measurements were performed using 1 cm<sup>2</sup> bright platinum samples. The table shows the modeled values for  $R_{ct}$ .

### C. Microelectrode Results

The impedance modulus, phase and standard deviations for the Pt black microelectrodes (geometric area 900 μm<sup>2</sup>) are presented in Fig. 5; fitted parameter values are given in Tab. 2. A variation in the total electrode area within the sample population arising from the platinization procedure results in a large measurement standard deviation apparent in the phase measurements at high frequencies. The theoretical value for the interface capacitance, 0.545 mF/m<sup>2</sup> (from Eqn. 2) and the relation  $area_{\omega=1Hz} = |Z_{CPA}| / |Z_{C_I}|$ , which simplifies to  $area = Q_n / C_I$ , were used to determine the total area of each of the 6 microelectrodes measured. The areas ranged from 8.36(10)<sup>3</sup> to 45.5(10)<sup>3</sup> μm<sup>2</sup>, with a standard deviation of 17.2(10)<sup>3</sup> μm<sup>2</sup>. Development of a more uniform platinization process is currently under investigation.

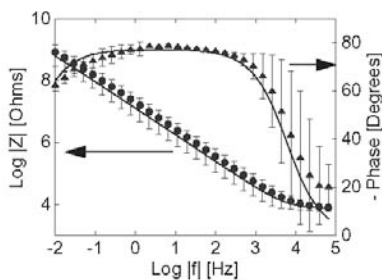


Fig. 5: Impedance modulus and phase experimental results for Pt black microelectrodes (geometrical area  $900 \mu\text{m}^2$ ). The modeled results are indicated by the solid lines [28].

#### D. Effect of Protein Coatings and Neuron Medium as Electrolyte

Fig. 6 shows the impedance modulus and phase results for the two protein coatings, laminin ( $n = 7$ ) and PLL ( $n = 5$ ), and for the measurements performed with neuron medium ( $n = 4$ ) as the electrolyte (see Tab. 2 for fitted parameter values). The charge transfer resistance of PLL and laminin is  $1.24$  and  $0.25 \text{ M}\Omega$ , respectively, a difference which quantifies the relative reactivity of the materials at the given conditions. For the PLL and laminin coatings the value for  $Q$  was found to be  $8.6$  and  $5.0 \mu\text{s}/\Omega^{-1/n}$ , respectively. In the case of the neuron medium as the electrolyte, the parameter value for  $R_{ct}$  is similar to that of bright Pt. The value of  $Q$  was found to be  $14.6 \mu\text{s}/\Omega^{-1/n}$  which is smaller than that of bright Pt. The solution resistance of the neuron medium was found to be  $40.4 \Omega$ , which yields a value of  $90.3 \Omega\text{cm}$  (from Eqn. 8) for the neuron medium resistivity.

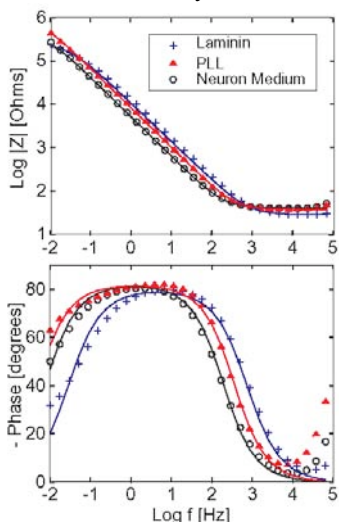


Fig. 6: Impedance modulus and phase for the laminin and PLL protein coatings, and the neuron medium as electrolyte. The modeled results are indicated by the solid lines.

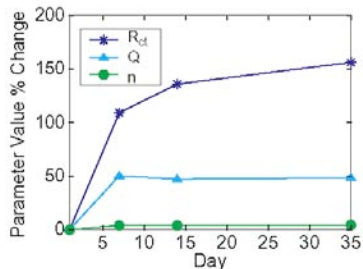


Fig. 7: Relative change in modeled parameter value as a function of time for  $1 \text{ cm}^2$  bright Pt incubated in medium containing 10 % horse serum for up to 35 days.

#### E. Effect of Time

The percent change in model parameter results for impedance recordings performed at days 1, 7, 14 and 35 in incubation are given in Fig. 7. In all cases the parameter value increases from day 1 to day 7, and then levels off. This demonstrates the effective encapsulation of the electrodes, as is discussed in the following section.

### V. DISCUSSION

An equivalent circuit model has been used to describe and analyze the EIS experimental results. A good match between the curves generated using the equivalent circuit model and the measurement results indicates that the appropriate model has been selected. For the simplest case of bright Pt, equations describing the macroscopic physical processes occurring at the electrode-electrolyte interface yield parameter values for  $C_I$  and  $R_S$  that are in good agreement with the experimentally derived parameters. The difference between  $|Z_{C_I}|$  and  $|Z_{CPA}|$  represents a 15 % deviation from the experimental value, which is evidence that the GCS model describes well the interface capacitance. The difference between the fitted and calculated theoretical value could be a result of impurities at the interface that are not accounted for in the GCS model. A 14% deviation from the measured value of the solution resistance indicates that Eqn. 7 can be used to calculate  $R_S$ .

Cyclic voltammetry was used to measure  $R_{ct}$  for the bright Pt-0.9% NaCl system. There is a 50% difference between the fitted  $R_{ct}$  value and that determined from cyclic voltammetry. The source of this difference is difficult to quantify, however is most likely a result of sensitivities, in both the EIS and the cyclic voltammetry measurements, to the interface conditions. It is worthwhile to mention that the  $R_{ct}$  value reported here is four orders of magnitude greater than the values reported in literature  $\sim 30 \Omega\text{cm}^2$  [10], [29]. The literature values are erroneously based on the assumption that the faradaic current flowing across the interface is due to a hydrogen redox reaction. For a neutral pH, the equilibrium potential of the hydrogen reaction is  $-0.654 \text{ V}$ , significantly negative of the OCP value of  $0.318 \pm 0.037 \text{ V}$ . Given the positive OCP value, the theoretical reaction would be the oxidation of hydrogen gas according to:  $\text{H}_2 \leftrightarrow 2\text{H}^+ + 2\text{e}^-$ , although the limited amount of hydrogen gas available in solution precludes this reaction from occurring. It is known from literature that, given the experimental conditions used in this work, it is the  $\text{O}_2$  redox reaction that is mainly responsible for the faradaic current (although contamination at the interface will also contribute to charge transfer) [27]. Experiment results presented here support this assumption. When the OCP is set to value higher or lower than the equilibrium value of approximately  $0.6 \text{ V}$  (from Eqn. 6 using a pH of 7.0), the  $R_{ct}$  is lower than if the OCP were equal to the equilibrium value. The higher or lower potential shifts the reaction from equilibrium conditions, more faradaic charge transfer occurs, and  $R_{ct}$  is reduced. For example, for an OCP of  $0.66 \text{ V}$  the charge transfer resistance is  $1.0 \text{ M}\Omega$  (Fig. 4). For an OCP of  $0.66 \text{ V}$  and  $0.92 \text{ V}$  the charge transfer resistance reduces to  $0.43 \text{ M}\Omega$  and  $0.23 \text{ k}\Omega$ , respectively. Since  $R_{ct}$  depends on  $J_0$ , it is interesting to compare the  $J_0$  value measured here with those reported in literature. The value reported by Kovacs for the oxygen reaction is  $4.5(10)^{-6} \text{ A}/\text{cm}^2$ , which was experimentally determined using a platinum electrode and aerated frog Ringer's solution ( $115 \text{ mM NaCl}$ ,  $2.0 \text{ mM KCl}$ ,  $1.8 \text{ mM CaCl}_2$ ) [7, 30].

Aeration of the electrolyte will increase the amount of  $O_2$  available for reaction, thereby increasing the equilibrium exchange current, which explains the deviation from the value reported here. The value reported by McAdams [19] for a platinum pacing electrode in physiological saline is  $6.41(10)^{-8}$  A/cm<sup>2</sup>, which is similar to our measured value of  $8.5(10)^{-8}$  A/cm<sup>2</sup>, albeit a direct comparison is invalid due to the 10% iridium content in the pacing electrode.

It has been the goal of this study to use the EIS results and model parameter values to develop an enhanced understanding of the effect of the physical processes on the interface impedance, with the expressed purpose of improving the interface design. For example, the impedance modulus of Pt black and TiN is two orders of magnitude smaller than for bright Pt, clearly demonstrating the effect of increased total surface area. This finding is expected and is well documented in previous studies [10], [29], [31]. A more interesting use of the results can be found in the effects of PLL and laminin on the interface impedance. Qualitatively there is little difference between the impedance modulus of PLL and laminin, however the phase results show that the phase decreases more rapidly for laminin than PLL, indicating a lower  $R_{ct}$  for laminin. Quantitatively this difference manifests itself in the modeled parameter results, where  $R_{ct}$  is 1.24 M $\Omega$  for PLL versus 0.25 M $\Omega$  for laminin. Although laminin is a thicker coating  $\sim 140$  nm compared to PLL  $\sim 10$  nm, it appears to facilitate charge transfer rather than to impede reactions. The effect of the protein coating thicknesses is apparent in the modeled parameter  $Q$ , which is approximately 1/3 of  $Q$  for bright Pt. Since  $Q$  is representative of the interface capacitance, which is inversely proportional to the ‘dielectric’ thickness (in this case the protein coating), it follows that the protein coatings would reduce  $Q$ . Such effects are important when considering an optimized interface design for the stimulation and recording of electrical activity from electrogenic cells, or when designing biosensors based on changes in the interface capacitance.

Additionally, the model has been used to quantify the effect of incubation time on the interface impedance. The relative change in the model parameter results over time show a sharp increase from day 1 to 7 followed by a plateau. Indeed, the impedance results themselves (not shown here) do not change significantly from day 7 to 35. This indicates that the electrodes have been encapsulated, most likely by proteins contained in the medium. For example, the value of  $n$  increases from 0.91 at day 1 to 0.95 at day 35, indicating that the interface has become more capacitive. Similarly,  $R_{ct}$  increases from 217 k $\Omega$  at day 1 to 556 k $\Omega$  at day 35, again demonstrating that the interface has become more capacitive, or less conducive to charge transfer. The same is true of  $Q$ , which increases from an initial value of  $6.5 \mu\text{s}/\Omega^{-1/n}$  to  $9.7 \mu\text{s}/\Omega^{-1/n}$  by day 35. These results are relevant to researchers who are performing electrophysiological measurements over extended periods of time. The changing electrode impedance of electrodes covered by cell cultures would additionally provide useful insights and shall be investigated in the future.

The ease in analyzing surface conditions using EIS and its widespread applicability gives merit to a short discussion on how this technique may be extended to other electrode-electrolyte systems and smaller electrode sizes. In order to use this technique with different systems, such as iridium oxide, gold, stainless steel and other biomedical metals with electrolytes of varying concentrations and compositions, the appropriate equivalent circuit, which is highly dependent on the equilibrium exchange current density, must be selected. For non-polarizable electrodes,

corresponding to a high equilibrium exchange current, the charge transfer resistance becomes low and a Warburg element, representing the effect of diffusion on the current-carrying ions, may be necessary to accurately model the interface conditions (the reader is referred to general references on EIS [25, 26, 32]). Due to the sensitivity of  $J_0$  to the interface conditions, as demonstrated in this work, the equilibrium exchange current varies significantly with electrode and electrolyte, and, hence care must be taken when using values from literature. It is therefore recommended that  $J_0$  be experimentally determined. Although values for  $J_0$  are reported in literature, for example Kovacs provides a table with various values [7], it is unlikely that the experimental conditions are exactly the same. Pourbaix diagrams may be used to determine the reactions giving rise to  $J_0$  and will provide a value for  $z$  that is required to determine  $R_{ct}$  using Eqn. 5. Many cases of EIS applied to different electrode-electrolyte systems can be found in literature, for example: Bates, et al., have analyzed a system of roughened Pt and aqueous  $H_2SO_4$  [33], Valoen, et al., have developed an impedance model for metal hydride electrodes in KOH [34], and Chou and colleagues have used EIS to investigate the effect of a self-assembled monolayer on a Au electrode inside a rat heart [35]. As a final extension to the model, it should be noted that while this theory may be applied to infinitely small electrodes, the experimental measurement becomes increasingly unstable with shrinking electrode dimensions because the current flowing across the interface becomes too small to be measured. Very small electrodes,  $\sim 100 \mu\text{m}^2$  must be measured at higher frequencies requiring special equipment.

## VI. CONCLUSIONS

A measurement technique with a corresponding equivalent circuit model has been established for the quantification of the electrode-electrolyte interface impedance using electrochemical impedance spectroscopy. Equations describing the macroscopic physical processes occurring at the interface are presented, and, for the case of bright Pt, yield results that are in good agreement with the fitted parameter values. The effect of various characteristics, such as total area, protein coating, and time on the EIS and fitted parameter results has been used to elucidate the processes occurring at the interface, thereby demonstrating the usefulness of the model in the impedance analysis of more complex, biomedically relevant situations.

## VII. ACKNOWLEDGMENTS

The authors would like to thank Professor Henry Baltes (on leave) for sharing laboratory resources and for his ongoing stimulating interest in their work.

## VIII. REFERENCES

- [1] J. Wegener, C. R. Keese, and I. Giaever, “Electric Cell-Substrate Impedance Sensing (ECIS) as a Noninvasive Means to Monitor the Kinetics of Cell Spreading to Artificial Surfaces,” *Experimental Cell Research*, vol. 259, pp. 158-166, 2000.
- [2] L. Yang, C. Ruan, and Y. Li, “Detection of viable Salmonella typhimurium by impedance measurement of electrode capacitance and medium resistance,” *Biosensors and Bioelectronics*, vol. 19(5), pp. 495-502, 2003.
- [3] C. A. Marquette, I. Lawrence, C. Polychronakos, and M. F. Lawrence, “Impedance based DNA chip for direct  $T_m$  measurement,” *Talanta*, vol. 56, pp. 763-768, 2002.
- [4] V. M. Mirsky, M. Riepl, and O. S. Wolfbeis, “Capacitive monitoring of protein immobilization and antigen-antibody reactions on

- monomolecular alkythiol films on gold electrodes," *Biosensors and Bioelectronics*, vol. 12, pp. 977-989, 1997.
- [5] C. Q. Huang, R. K. Shepherd, P. M. Center, P. M. Seligman, and B. Tabor, "Electrical stimulation of the auditory nerve: direct current measurement in vivo," *IEEE Trans. on Biomedical Engineering*, vol. 46, pp. 461-470, 1999.
- [6] M. Tykocinski, Y. Duan, B. Tabor, and R. S. Cowan, "Chronic electrical stimulation of the auditory nerve using high surface area (HiQ) platinum electrodes," *Hearing Research*, vol. 159, pp. 53-68, 2001.
- [7] G. T. A. Kovacs, "Introduction to the theory, design, and modeling of thin-film microelectrodes for neural interfaces," in *Enabling Technologies for Cultured Neural Networks*, D. A. Stenger and T. M. McKenna, Eds. London: Academic Press, 1994, pp. 121-165.
- [8] G. W. Gross, B. K. Rhoades, D. L. Reust, and F. U. Schwalm, "Stimulation of monolayer networks in culture through thin-film indium-tin oxide recording electrodes," *Journal of Neuroscience-Methods*, vol. 50, pp. 131-43, 1993.
- [9] P. Thiebaud, C. Beuret, M. Koudelka-Hep, M. Bove, S. Martinoia, M. Grattarola, H. Jahnsen, R. Rebaudo, M. Balestrino, J. Zimmer, and Y. Dupont, "An array of Pt-tip microelectrodes for extracellular monitoring of activity of brain slices," *Biosensors and Bioelectronics*, vol. 14, pp. 61-5, 1999.
- [10] M. O. Heuschkel, "Fabrication of multi-electrode array devices for electrophysiological monitoring of in vitro cell/tissue cultures," in *Series in Microsystems*, vol. 13, P. A. Besse, M. Gijs, R. S. Popovic, Ph. Renaud, Ed. Konstanz: Hartung-Gorre Verlag, 2001.
- [11] E. Warburg, "Ueber das Verhalten sogenannter unpolarisbarer Elektroden gegen Wechselstrom," *Annalen der Physik und Chemie*, vol. 67, pp. 493-499, 1899.
- [12] H. Fricke, "The theory of electrolytic polarization," *Philosophical Magazine*, vol. 7, pp. 310-318, 1932.
- [13] J. E. B. Randles, "Kinetics of Rapid Electrode Reactions," *Discussions of the Faraday Society*, vol. 1, pp. 11-19, 1947.
- [14] D. Jaron, H. P. Schwan, and D. B. Geselowitz, "A mathematical model for the polarization of cardiac pacemaker electrodes," *Medical and Biological Engineering*, vol. 6, pp. 579, 1968.
- [15] B. Onaral and H. P. Schwan, "Linear and nonlinear properties of platinum electrode polarisation. I. Frequency dependence at very low frequencies," *Medical and Biological Engineering and Computing*, vol. 20, pp. 299-306, 1982.
- [16] H. P. Schwan, "Electrode polarization impedance and measurements in biological materials," *Annals of the New York Academy of Sciences*, vol. 148, pp. 191-209, 1968.
- [17] H. P. Schwan, "Linear and nonlinear electrode polarization and biological materials," *Annals of Biomedical Engineering*, vol. 20, pp. 269-88, 1992.
- [18] E. McAdams, "Effect of surface topography on the electrode-electrolyte interface impedance," *Surface Topography*, vol 2, pp. 107-122, 1989.
- [19] E. T. McAdams and J. Jossinet, "Physical interpretation of Schwan's limit voltage of linearity," *Medical and Biological Engineering and Computing*, vol. 32, pp. 126-30, 1994.
- [20] E. T. McAdams, A. Lacknermeier, J. A. McLaughlin, D. Macken, and J. Jossinet, "The linear and non-linear electrical properties of the electrode-electrolyte interface," *Biosensors and Bioelectronics*, vol. 10, pp. 67-74, 1995.
- [21] M. Janders, U. Egert, M. Stelzle, and W. Nisch, "Novel thin film titanium nitride micro-electrodes with excellent charge transfer capability for cell stimulation and sensing applications," *Proc. IEEE Eng. in Medicine and Biology Society*, Amsterdam, Netherlands, 1997.
- [22] M. Pourbaix, *Atlas of Electrochemical Equilibria in Aqueous Solutions*, 2 ed. Brussels: National Association of Corrosion Engineers, 1974.
- [23] W. Franks, F. Heer, I. McKay, S. Taschini, R. Sunier, C. Hagleitner, A. Hierlemann, H. Baltes, "CMOS monolithic microelectrode array for stimulation and recording of natural neural networks," *Transducers '03*, Boston, 2003.
- [24] D. C. Grahame, "Mathematical theory of the faradaic admittance," *Journal of Electrochemical Society*, vol. 99, pp. 370C-385C, 1952.
- [25] A. J. Bard and L. R. Faulkner, *Electrochemical Methods*, New York: John Wiley and Sons, 2001.
- [26] J. O. M. Bockris and A. K. N. Reddy, *Modern Electrochemistry*, vol. 2. New York: Plenum Press, 1970.
- [27] E. Yeager, "Electrocatalysts for O<sub>2</sub> reduction," *Electrochimica Acta*, vol. 29, pp. 1527-1537, 1984.
- [28] F. Heer, W. Franks, A. Blau, S. Taschini, C. Ziegler, A. Hierlemann, H. Baltes, "CMOS microelectrode array for monitoring of electrogenic cells," *Biosensors and Bioelectronics*, vol. 20, pp. 358-366, 2004.
- [29] D. A. Borkholder, "Cell based biosensors using microelectrodes," PhD thesis in Electrical Engineering, Stanford University, 1998.
- [30] P. W. Davies, "The oxygen cathode," in *Physical techniques in biological research*, vol. IV, W. L. Nastuk, Ed. London: Academic Press, 1962, pp. 137-179.
- [31] J. D. Weiland, D. J. Anderson, M. S. Humayun, "In vitro electrical properties for iridium oxide versus titanium nitride stimulating electrode," *IEEE Transactions on Biomedical Engineering*, vol. 49, no. 12, pp. 1574 - 1579, Dec. 2002.
- [32] J. R. Macdonald, *Impedance Spectroscopy*, New York: John Wiley and Sons, 1987.
- [33] J. Bates, Y. Chu, "Electrode-electrolyte interface impedance: experiments and model," *Annals of Biomed Eng.*, vol. 20, pp. 349 - 363, 1992.
- [34] L. O. Valeon, S. Sunde, R. Tunold, "An impedance model for electrode processes in metal hydride electrode," *Journal of Alloys and Compounds*, vol. 253 - 254, pp. 656 - 659, May 20, 1997.
- [35] H. A. Chou, D. H. Zavitz, and M. Ovadia, "In vivo CH<sub>3</sub>(CH<sub>2</sub>)<sub>11</sub>SAU SAM electrodes in the beating heart: In situ analytical studies relevant to pacemakers and interstitial biosensors," vol. 18, pp. 11-21, 2003.



**Wendy Franks** received her B. Sc. in chemical engineering in 1998 and an M.Sc. in electrical engineering in 2000, both at the University of Waterloo, Canada. She is currently pursuing her PhD at the Swiss Federal Institute of Technology, Zurich (ETHZ) in the field of bioelectronics.



**Iwan Schenker** received his Diploma in physics from the Swiss Federal Institute of Technology (ETHZ), Zurich, Switzerland, in 2003. He is currently working towards his Ph.D. degree in the Nonmetallic Inorganic Materials Group, Department of Materials, ETHZ, Zurich, Switzerland. His current research interests include the relation between microstructure and macro-mechanical behavior of wet granular assemblies.



**Patrik Schmutz** is currently Head of Corrosion Research at the EMPA (National Laboratory for Material Science and Technology) and is a Lecturer at the Swiss Federal Institute of Technology in Zurich (ETHZ), Switzerland. His main research topic is investigation of localized physico-(electro)chemical processes on reactive metallic surfaces. He received an undergraduate degree in Solid-State Physics in 1991 from the University of Fribourg, Switzerland and a Ph.D degree in Science in 1996 from the Swiss Federal Institute of Technology in Lausanne (EPFL).



**Andreas Hierlemann** received his Diploma in chemistry in 1992 and the Ph.D. degree in physical chemistry in 1996 from the University of Tübingen, Germany. Having been a Postdoc at Texas A&M University, College Station, TX (1997), and Sandia National Laboratories, Albuquerque, NM (1998), he is currently professor at the Physical Electronics Laboratory at ETH Zurich in Switzerland. The focus of his research activities is on CMOS-based microsensors and interfacing CMOS electronics with electrogenic cells.

---

# APPENDIX B

## CMOS MICROELECTRODE ARRAY FOR THE MONITORING OF ELECTROGENIC CELLS

F. Heer, W. Franks, A. Blau<sup>\*</sup>, S. Taschini, C. Ziegler<sup>\*</sup>, A. Hierlemann, H. Baltes  
Physical Electronics Laboratory, ETH Zurich, 8093 Zurich, Switzerland

<sup>\*</sup>Department of Biophysics, University of Kaiserslautern, 67663 Kaiserslautern, Germany

Published in: Biosensors and Bioelectronics, v. 20, pp. 358 - 366, 2004.

# CMOS microelectrode array for the monitoring of electrogenic cells

F. Heer<sup>a,\*</sup>, W. Franks<sup>a</sup>, A. Blau<sup>b</sup>, S. Taschini<sup>a</sup>, C. Ziegler<sup>b</sup>, A. Hierlemann<sup>a</sup>, H. Baltes<sup>a</sup>

<sup>a</sup> *Physical Electronics Laboratory, ETH Zurich, 8093 Zurich, Switzerland*

<sup>b</sup> *Department of Biophysics, University of Kaiserslautern, 67663 Kaiserslautern, Germany*

Received 21 October 2003; received in revised form 4 February 2004; accepted 5 February 2004

Available online 19 March 2004

## Abstract

Signal degradation and an array size dictated by the number of available interconnects are the two main limitations inherent to standalone microelectrode arrays (MEAs). A new biochip consisting of an array of microelectrodes with fully-integrated analog and digital circuitry realized in an industrial CMOS process addresses these issues. The device is capable of on-chip signal filtering for improved signal-to-noise ratio (SNR), on-chip analog and digital conversion, and multiplexing, thereby facilitating simultaneous stimulation and recording of electrogenic cell activity. The designed electrode pitch of 250  $\mu\text{m}$  significantly limits the space available for circuitry: a repeated unit of circuitry associated with each electrode comprises a stimulation buffer and a bandpass filter for readout. The bandpass filter has corner frequencies of 100 Hz and 50 kHz, and a gain of 1000. Stimulation voltages are generated from an 8-bit digital signal and converted to an analog signal at a frequency of 120 kHz. Functionality of the read-out circuitry is demonstrated by the measurement of cardiomyocyte activity. The microelectrode is realized in a shifted design for flexibility and biocompatibility. Several microelectrode materials (platinum, platinum black and titanium nitride) have been electrically characterized. An equivalent circuit model, where each parameter represents a macroscopic physical quantity contributing to the interface impedance, has been successfully fitted to experimental results.

© 2004 Elsevier B.V. All rights reserved.

**Keywords:** Microelectrode array; CMOS; Electrogenic cells; Cardiomyocytes; Cell-based biosensor; Impedance

## 1. Introduction

Since its inception in the early 1970s (Wise, 1971; Thomas et al., 1972), the microelectrode array (MEA) has evolved into a tool capable of making significant contributions to the fields of neuroscience and biosensing (Rutten, 2002). The primary advantages of extracellular recordings over traditional methods (patch clamp, voltage-sensitive dyes) include non-invasiveness, multi-site measurement capabilities, and long measurement periods. However, despite concentrated research efforts widespread use has yet to be achieved as crucial design and development issues, such as low signal-to-noise ratio (SNR), flexible stimulation and readout capabilities, perfusion chambers with coupled microfluidics, and controlled growth techniques have yet to be satisfactorily addressed (Borkholder, 1998; Gross et al., 1995).

MEAs, with their ability to measure complex spatio-temporal neural activity, are poised to become a fundamental tool in neuroscience research.

In developing embryos, synchronized burst activity is thought to be important in fine tuning neuronal networks. MEAs have achieved a high degree of success in the study and characterization of this activity (Keefer, 2001a,b; Tschertter et al., 2001; Streit et al., 2001; Jimbo and Robinson, 2000). To study neurological phenomena such as Hebbian learning, the neural networks must be mapped; this could be achieved using neural tissue slices which exhibit significantly reduced cell mobility. Organotypic culturing of rat hippocampal and spinal cord tissue slices on MEAs (Egert et al., 1998; Thiebaud et al., 1999; Borkholder et al., 1997) demonstrate this potential. Other ways to create defined neural networks are to control the growth of processes with columnar structures (Zeck and Fromherz, 2001), with chemical cues (Prinz and Fromherz, 2000), or to trap the cells in cages (Maher et al., 1999). Shahaf and Marom have shown that learning in cortical neural networks occurs in vitro, thereby demonstrating the effectiveness of MEAs in the study of synaptic plasticity (Shahaf and Marom, 2001; Marom and Shahaf, 2002).

Cell-based biosensors are promising tools for the detection of chemical and biological toxins or for the screening of pharmacologically active compounds (the reader is directed

\* Corresponding author. Tel.: +41-1633-6577; fax: +41-1633-1054.  
E-mail address: [heer@iqe.phys.ethz.ch](mailto:heer@iqe.phys.ethz.ch) (F. Heer).



to numerous reviews: Kovacs, 2003; McFadden, 2002; Pancrazio et al., 1999; Gross et al., 1995). These systems employ highly evolved cellular pathways and have the advantage that no previous knowledge of the investigated compound is required. Field-portable systems using cardiomyocytes have been developed at the Stanford Transducers Lab and the Naval Research Laboratory (DeBusschere and Kovacs, 2001; Gilchrist et al., 2001; Pancrazio et al., 1998b). Neuronal network-based biosensors have been used to demonstrate that *in vitro* cultures retain tissue-specific properties, and moreover, findings corroborate well with whole animal *in vivo* studies (Morefield et al., 2000; Keefer, 2001a,b). It can be envisioned that cell-based biosensors will replace animals in toxicology studies (van der Schalie et al., 1999).

The accurate measurement of low extracellular bioelectric signals, ranging from microvolts for neurons to millivolts for cardiomyocytes, at multiple points within a culture are the two key requirements considered when designing an MEA and recording system. Typical system designs incorporate an MEA with an external, off-chip system controlling electrode selection, signal amplification and interfacing (Gross, 1979; Gross et al., 1993; Borkholder, 1998; Connolly et al., 1990; Bucher et al., 1999; Heuschkel et al., 2002; Multi Channel Systems, 2001; Jenkner et al., 2001). However, as the recorded signal travels to the amplification system, passing several electronic interfaces, it can be distorted by electromagnetic interference resulting in a reduced signal-to-noise ratio. A crucial design consideration for large arrays is multiplexing. If multiplexing circuitry is not included each electrode requires an associated bond pad thereby limiting the array size to the number of available bond pads. CMOS integration can overcome both of these technical challenges. First approaches include a two-chip solution, where a CMOS chip with instrumentation amplifiers and electrode selection circuitry is placed in close proximity to the MEA chip (Pancrazio et al., 1998a). Single-chip solutions with fully-integrated CMOS multiplexing and buffering circuitry have been presented, with on-chip (Bai and Wise, 2001) and off-chip (DeBusschere and Kovacs, 2001) signal amplification. More recently systems have emerged, such as a FET-based, 16,384 microelectrode CMOS biosensor array comprising on-chip amplification circuitry with readout multiplexers and buffers (Eversmann et al., 2003), or, similarly, an MEA with on-chip amplification, filtering and addressability (Berdonini et al., 2002). While these designs represent significant improvements in neurochip development and the use of multiplexers translates into almost unconstricted array sizes, they do not yet include flexible on-chip stimulation capabilities.

Here, we report on a new biochip comprising a microelectrode array and fully-integrated analog and digital CMOS circuitry for the stimulation and recording of activity from electrogenic cells. In contrast to the systems mentioned previously, this device is capable of on-chip signal filtering for improved SNR, on-chip analog and digital conversion to prevent signal degradation, multiplexing, and

simultaneous recording and stimulation. Each electrode has an associated circuitry unit including a stimulation buffer and switch, a bandpass filter and a readout buffer. The electrode and circuitry form a repeatable unit with a pre-defined 250  $\mu\text{m}$  pitch that significantly limits the area available for circuitry. To achieve the electrode pitch, only the components necessary to condition the small signals and to provide reliable, addressable stimulation signals have been assembled in a repeated circuitry unit. This repeatable unit can be multiplied to form a larger array. The stimulation buffer uses a class-AB output stage in order to deliver large currents to the electrode. Stimulation voltages are generated from an 8-bit digital signal converted to an analog signal at a frequency of 120 kHz. As a result, any stimulation waveform can be generated. The bandpass filter has corner frequencies of 100 Hz and 50 kHz and a gain of 1000. The microelectrode is realized in a shifted design for flexibility and biocompatibility purposes. Several biomedically relevant microelectrode materials, platinum, platinum black and titanium nitride, have been electrically characterized, and an equivalent circuit model of the impedance is presented.

## 2. Methods

### 2.1. System design

The 4.4 mm  $\times$  4.4 mm chip presented here consists of a 4  $\times$  4 electrode array with integrated reference electrode (Fig. 1) (Franks et al., 2003). Fabrication was performed using an industrial double-polysilicon, triple-metal, 0.6  $\mu\text{m}$  CMOS process at Austriamicrosystems AG (Austria). The electrodes are 40  $\mu\text{m}$   $\times$  40  $\mu\text{m}$  with a 250  $\mu\text{m}$  pitch. Space between the electrode array and bond pads has been intentionally left blank for the sealant that isolates the cells from the bond wires. A block diagram with the main circuitry components is given in Fig. 1. A unit of repeating circuitry comprising a buffer and switch for stimulation, a bandpass filter and buffer for readout, is provided with each electrode (inset, Fig. 1). Additionally, the system architecture incorporates four analog-to-digital converters (ADC, one per row of electrodes) and one digital-to-analog converter (DAC). On-chip multiplexing and A/D-conversion allow for a reduction in the number of bondpads, which facilitates the integration of a large array. A digital control unit scans the array during readout, provides individual electrode addressability for stimulation, and interfaces with the outside world. Simultaneous recording and stimulation at each electrode can be performed. For the purpose of monitoring the chip operation temperature and the culture temperature, a temperature sensor has been included.

### 2.2. Electrode design

Due to a limited selection of materials available in a commercial CMOS process, the electrode material as received

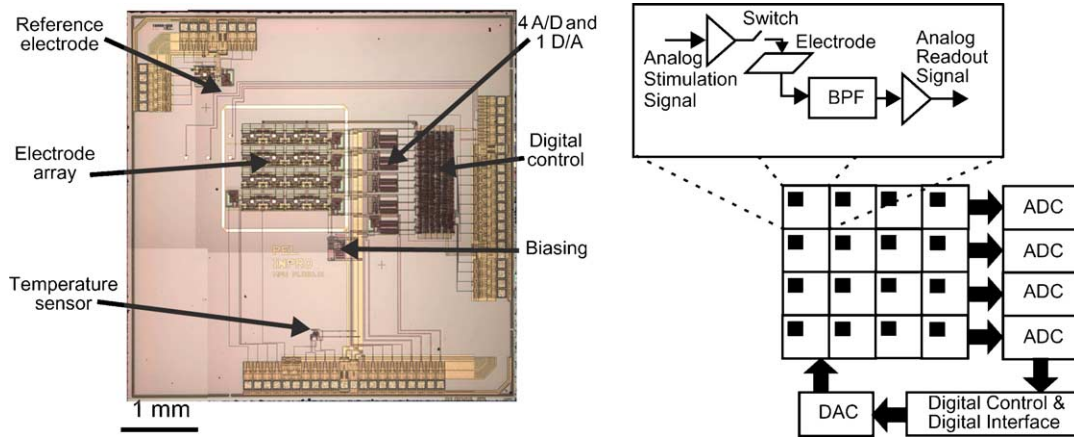


Fig. 1. Photograph of CMOS chip on the left. Block diagram of the system architecture on the right. Inset shows the contents of the repeated circuitry unit.

from the foundry is aluminum, a known neurotoxicant. A simple 2-mask post-processing procedure is employed to cover the Al electrodes with biocompatible platinum. During this processing the electrodes are shifted (Fig. 2), and the aluminum is sealed with the electrode metal and a passivation stack. It is necessary to seal the underlying Al to avoid both poisoning and undesirable electrochemistry that occurs when the Al comes into contact with the neuron medium. The electrode metal consists of 50 nm TiW, an adhesion promoter, and 270 nm of Pt. The metals are sputter-deposited and structured in a lift-off process. An alternating  $\text{Si}_3\text{N}_4/\text{SiO}_2$  passivation stack consisting of  $1\ \mu\text{m}$  of  $\text{Si}_3\text{N}_4$ , and two times 100 nm  $\text{SiO}_2$  and 200 nm  $\text{Si}_3\text{N}_4$  (total layer thickness of  $1.6\ \mu\text{m}$ ) is deposited using plasma-enhanced chemical vapor deposition (PECVD). A mixed frequency PECVD process was used to match the

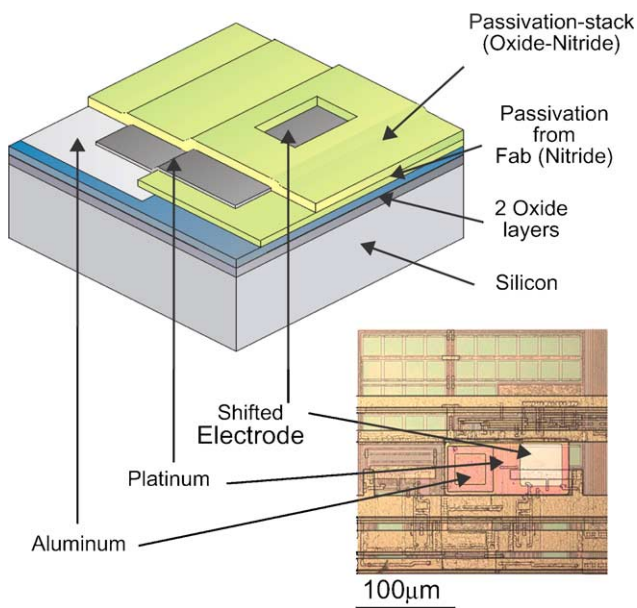


Fig. 2. Cross-section (left) and micrograph (right) of the shifted Pt-electrode. Micrograph shows one circuitry repeating unit.

stress with that of the underlying  $\text{Si}_3\text{N}_4$  deposited during the CMOS process. A simpler solution featuring a single  $1\ \mu\text{m}$   $\text{Si}_3\text{N}_4$  layer has been attempted, but proved to be ineffective in sealing the Al, resulting in the dissolution of the reference electrode during cell culturing. It is believed that the roughness of the underlying Al layer leads to pinholes in the  $\text{Si}_3\text{N}_4$  layer; however, when a stack of alternating oxide and nitride layers is deposited these pinholes are covered. Neurons have been cultured for 28 days on chips with the  $1.6\ \mu\text{m}$  passivation stack, and no degradation effects have been observed. A reactive-ion etch (RIE) is then used to open the nitride stack defining the size and shape of the electrodes. This increases design flexibility since the electrode dimensions are not defined by the CMOS process. The processed chips are bonded and packaged in a two-step process. An epoxy (Masterbond 42HT-T, Masterbond Inc., USA) is first used to stabilize the bonds on the chip and the package. Polydimethylsiloxane (PDMS) is then used to form a bath, isolating the bond wires from the cells. A glass O-ring, affixed to the chip with PDMS, forms a larger bath capable of containing a suitable amount of neuron medium (Fig. 3).

### 2.3. Electrode characterization and modeling

Extracellular signals are typically minute making a low electrode–electrolyte interface impedance imperative. To characterize the electrode–electrolyte interface electrochemical impedance spectroscopy (EIS) has been performed for bright Pt, Pt black and TiN. The EIS measurements have been used to model the interface with an equivalent circuit model where each parameter represents a macroscopic physical process contributing to the interface impedance. An enhanced understanding of the physical processes can be used to better understand the transduction principle and to design a lower-impedance electrode.

The measurements have been fitted to the equivalent circuit model (Fig. 4) comprising a constant phase angle impedance,  $Z_{\text{CPA}}$ , shunted by a charge transfer resistance,

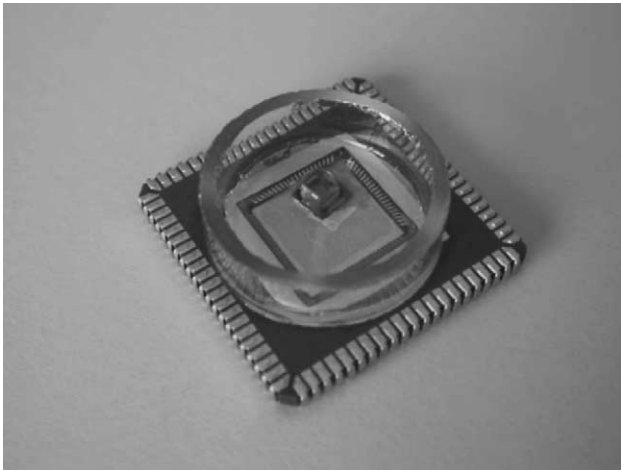


Fig. 3. Image of packaged chip.

$R_{ct}$ , together in series with the solution resistance,  $R_s$  (Grahame, 1952). The constant phase angle impedance first proposed by Fricke (1932) is a measure of the non-Faradaic impedance arising from the interface capacitance, or polarization capacitance, and is given by the empirical relation:

$$Z_{CPA}(\omega) = \frac{1}{(j\omega Q)^n}$$

where  $Q$  is a measure of the magnitude of  $Z_{CPA}$ ,  $n$  is a constant ( $0 \leq n \leq 1$ ) representing inhomogeneities in the surface and  $\omega = 2\pi f$ . In a Nyquist plot, the angle between the data and the abscissa axis gives  $n$  from  $n = (2\theta)/\pi$ . When  $n = 1$ ,  $Z_{CPA}$  represents a pure capacitive element corresponding to the interface capacitance. Faradaic charge transfer leads to  $R_{ct}$ , which in the case of Pt is believed to be due to the hydrolysis of  $H_2O$  and reduction of  $O_2$  according to  $2H_2O \leftrightarrow O_2 + 4H^+ + 4e^-$  where the equilibrium potential is  $0.987 - 0.059 \times \text{pH}$  with respect to the standard calomel electrode (SCE) (Yeager, 1984). Experiment findings support this assumption. When the open-circuit potential (OCP) is set to value higher or lower than the equilibrium value of  $\sim 0.6 \text{ V}$ , then the  $R_{ct}$  is lower than if the OCP were equal to the equilibrium value. The higher or lower potential shifts the reaction from equilibrium conditions, more Faradaic charge transfer occurs, and  $R_{ct}$  is reduced. For example, for an OCP of  $0.66 \text{ V}$  the change transfer resistance is  $1.0 \text{ M}\Omega$ . For an

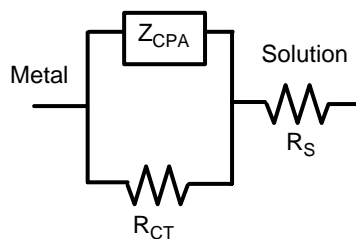


Fig. 4. Equivalent circuit model of electrode–electrolyte interface. Measured results are given in the table.

	Q [ $s\Omega^{-1/n}$ ]	n	$R_s$ [ $\Omega$ ]	$R_{CT}$ [ $10^5\Omega$ ]
Pt	$2.72(10)^{-5}$	0.92	28.0	4.48
Std. Dev.	$0.26(10)^{-5}$	0.01	2.81	0.88
Pt Black	$2.08(10)^{-3}$	0.91	30.7	0.51
Std. Dev.	$0.11(10)^{-3}$	0.03	7.85	0.28
TiN	$2.03(10)^{-3}$	0.91	42.3	3.00
Std. Dev.	$5.77(10)^{-5}$	0.00	3.70	3.20

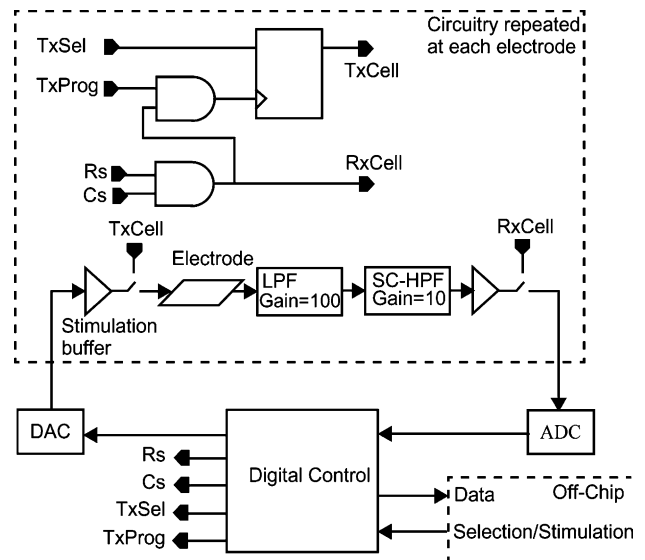


Fig. 5. Schematic of stimulation and readout circuitry.

OCP of  $0.39$  and  $0.92 \text{ V}$  the charge transfer resistance reduces to  $0.43$  and  $0.23 \text{ M}\Omega$ , respectively. However, it should be noted that the presence of any impurities at the interface will also lead to a reduced charge transfer resistance.

#### 2.4. Stimulation circuitry

The chip presented in this paper is capable of stimulating any subset of electrodes with any arbitrary waveform. When a stimulation phase is enabled, the on-chip digital control sets the selection by adjusting the switch between the stimulation-buffer and the electrode (Fig. 5). Since the impedance of the electrode varies significantly with electrode material, size, and electrolyte, a buffer with a class-AB output stage was used in order to be capable of delivering large currents (up to  $10 \text{ mA}$  if needed). The buffer (Fig. 6) comprises a differential input stage (M1, M2) with an active load (M3) and is connected in unity gain ( $V_{OUT}$  connected to gate of M2). The class-AB stage is formed by the transistors M5, M6, M9 and M10, where M5 and M6, both diode connected, bias the output transistors M9 and M10. If the input voltage ( $V_{IN}$ ) is increased, M9 forces the output voltage ( $V_{OUT}$ ) to follow. The load current is delivered by

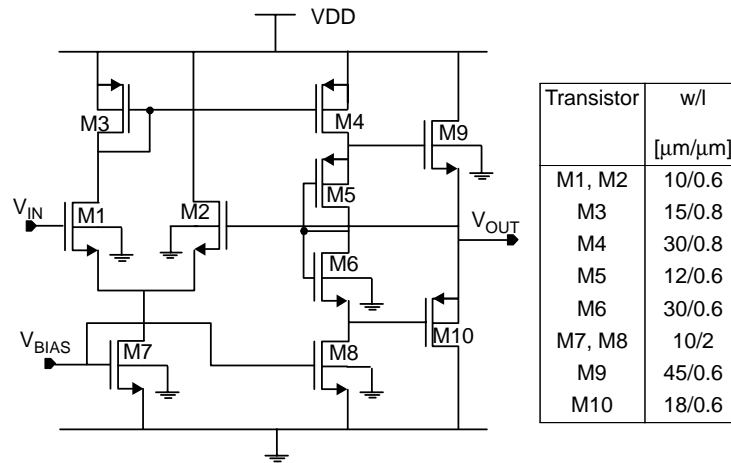


Fig. 6. Schematic of the class-AB stimulation buffer. Transistor sizes are summarized in the table.

M9, whose gate-source voltage ( $V_{GS}$ ) will increase slightly. Since a constant voltage is maintained between the gates of M9 and M10 the  $V_{GS}$  of M10 decreases by the same amount that the  $V_{GS}$  in M9 increases. M10 stays on, but conducts only a small current. When  $V_{IN}$  is lowered the situation is inverted, with M10 forcing  $V_{OUT}$  to follow and with the current through M9 decreasing. The power consumption is  $45 \mu\text{W}$  for vanishing input, given a current of  $2 \mu\text{A}$  through M7 and M8, and a supply voltage ( $V_{DD}$ ) of 5 V. However, when slewing, the amplifier can deliver up to 10 mA to the electrode. This corresponds to a maximum current density of  $60 \text{ A}/\text{cm}^2$ . The whole buffer occupies an area of  $42 \mu\text{m} \times 32 \mu\text{m}$  and has a bandwidth of  $\sim 10 \text{ MHz}$ .

The programming of the array is described as follows (Fig. 5). Transmission gates are used as switches for stimulation (TxCell) and readout (RxCell). Both are set by a small control unit consisting of a flip-flop and two AND gates. The row and column signals, RS and CS, are used for readout operation. When RxCell is high the signal is sampled by the ADC.

The programming of the array is done with two signals TxSel and TxProg. The on-chip digital control generates these signals based on the pattern information received from the PC. When RxCell goes high while TxProg is high the flip flop, which controls the stimulation switch, can be set with TxSel.

Subsequent to selection digital stimulation patterns are sent to the chip continuously until the stimulation phase is stopped. Stimulation voltages are in a range given by two reference voltages, which have a resolution of 8-bit and a cycling of 120 kHz. The time delay between enabling a stimulation phase and first stimulation voltage to reach the electrode is  $25 \mu\text{s}$ . The time required to go from one subset of electrodes to the next including deselection, selection and time required for a first stimulation voltage to reach the electrodes is  $50 \mu\text{s}$ . Stimulation phases can take place at any time throughout the measurement and are not limited in number. For deselection of the electrodes the signal TxProg is set high while TxSel is low.

## 2.5. Readout circuitry

Electrogenic cells induce small signals on the electrodes. The range is tens of microvolts for neural signals up to millivolts for heart cells. In order to prevent signal degradation signal conditioning should be implemented as close to the electrode as possible. For this reason, buffering and filtering circuits are adjacent to and repeated at each electrode (Figs. 1 and 5). The available space for the circuitry blocks is limited by the pitch between two electrodes, which is designed to be  $250 \mu\text{m}$ . It is possible that several cells produce signals on the same electrode. A 20 kHz sampling frequency is adopted so as to be able to resolve signal components originating from different cells.

When an action potential occurs in a cell above the electrode, ions flowing across the cell membrane inducing a charge redistribution on the electrode. The frequency of these signals is expected to be approximately 1 kHz. AC-coupling is mandatory for biological signals due to large drifts. Additionally, low pass filtering limits the noise bandwidth and provides anti-aliasing. Consequently, we implemented a bandpass filter with a center frequency around 1 kHz. The corner frequencies of the filter were chosen to be 100 Hz and 50 kHz. Similar specification can be found in literature (DeBusschere and Kovacs, 2001; Bai and Wise, 2001). The bandpass filter is divided into two stages. The first step is a low-pass filter, which buffers and amplifies the signals by a factor of 100. The electrode is directly connected to the non-inverting input of the amplifier, the gate of a MOSFET, which has a high input impedance in CMOS technology. This is similar to other systems, which have successfully acquired signals from electrogenic cells (Fromherz, 2002, DeBusschere and Kovacs, 2001). Signals in the range of tens of microvolts can be measured since the equivalent input noise of the amplifier is below  $10 \mu\text{V}_{\text{RMS}}$  over the band 100 Hz–100 kHz. Very little area ( $120 \mu\text{m} \times 70 \mu\text{m}$ ) is occupied by the amplifier. Furthermore, the amplifier uses an internally compensated OpAmp, which acts as a low-pass filter with a corner frequency of

~50 kHz. This corner can vary between 20 and 100 kHz due to process parameter variations. The low-pass transfer function in this first stage provides the anti-aliasing, that is mandatory for the switched-capacitor circuit in the following stage. The high-pass filter implemented in the second stage has a gain of 10 and a corner frequency at 100 Hz. A large time constant is needed in the high-pass filter, in order to achieve the low cut-off frequency of 100 Hz. Since the available space is limited, we used a switched capacitor solution. After the second filter, the signal is buffered and sent to the ADC via an analog multiplexer. As multiplexing takes place after signal amplification and filtering, the design is less sensitive to switching and electromagnetic interference. The ADC uses the successive-approximation technique and has a resolution of 8 bits. A positive and a negative reference voltage define the range. Digital values are finally sent to a PC through an 8-bit parallel bus.

### 3. Results

#### 3.1. Electrode impedance

Fig. 7 shows the measured (dashed markers) and modeled (solid line) results of the impedance modulus and phase as a function of frequency for three different materials: bright Pt ( $n = 4$ ), Pt black ( $n = 4$ ), and TiN ( $n = 3$ ). A large geometric surface area,  $1 \text{ cm}^2$ , was initially used to avoid complications arising from low current measurements typical of very small areas. Measurements were performed using a commercially available Autolab PGSTAT30 potentiostat system with Frequency Response Analysis software (version 4.8, Eco

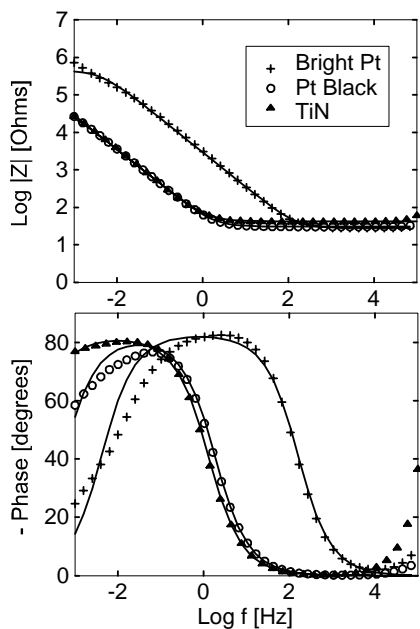


Fig. 7. Impedance modulus and phase as a function of frequency for  $1 \text{ cm}^2$  Pt, Pt-black and TiN electrode materials.

Chemie B.V., Netherlands). In this three electrode system a standard calomel electrode (SCE) is the reference electrode, the counter electrode is a large-area Pt-mesh, and the electrolyte is 0.9% NaCl. The perturbation potential was 10 mV and the scan range was  $10^{-3}$  to  $10^5$  Hz. The Pt electrodes were additionally treated by voltammetric cycling from  $-0.5$  to  $1.0$  V for typically six cycles, when the measurement stabilized. This procedure potentially results in the formation and reduction of Pt oxide and Pt dioxide layers, as indicated by the Pt–H<sub>2</sub>O Pourbaix diagram (Pourbaix, 1974). Before performing the impedance scan the open-circuit potential (OCP) was recorded. The OCP is a function of the chemical composition of the interface, and can be used for quality control of the initial interface conditions. Average OCP values for Pt, Pt black and TiN were  $0.318 \pm 0.037$ ,  $0.299 \pm 0.061$ , and  $0.046 \pm 0.034$  V, respectively.

#### 3.2. Equivalent circuit model parameter results

The derived values for the equivalent circuit model parameters, and standard deviation, are given in the table in Fig. 4. The various model parameters can be graphically interpreted from specific regions in the EIS measurements. At high frequencies the phase angle tends to zero and the modulus is solely due to  $R_s$ . Similarly, at low frequencies the phase once again tends to zero, and the modulus represents the sum of  $R_s$  and  $R_{ct}$ . In the mid-frequency range the phase tends to  $-90^\circ$ , representing a capacitive element, in this case the interface capacitance. The deviation of the model from experimental results at low frequencies can be attributed to the non-linear behavior of  $R_{ct}$  at low frequency (McAdams and Jossinet, 1994). As expected, the dendritically structured Pt black and TiN, with an increased total surface area, reduce the impedance modulus by approximately two orders of magnitude. The impedance of  $900 \mu\text{m}^2$  Pt black micro-electrodes was found to be  $4.84 \times 10^4 \Omega$  at 1 kHz.

Cyclic voltammetry was used to determine the equilibrium exchange current density of bright Pt. The following measurement parameters were used: 5 mV perturbation signal with respect to OCP, 0.5 mV/s scan rate, 0.15 mV step potential, averaged over 10 scans. From the slope of the current-versus-applied-potential plot the exchange current density is calculated to be  $8.5(10)^8 \text{ A/cm}^2$  and  $R_{ct}$  is  $3.0(10)^5 \text{ } \Omega$ . This finding results in the omission of a Warburg impedance element in the model over the measurement frequency range used here.

The presented model is similar to others that have been previously applied, however here the parameters are associated with macroscopic physical processes contributing to the interface impedance (De Boer and Van Oosterom, 1978; Onaral and Schwan, 1982). Models that do attribute physical processes to circuit elements include a Warburg impedance element for diffusion (McAdams et al., 1995; Kovacs, 1994). In the frequency range used here no experimental evidence for a diffusional impedance has been found and it has therefore been omitted. It is possible that a diffusional impedance

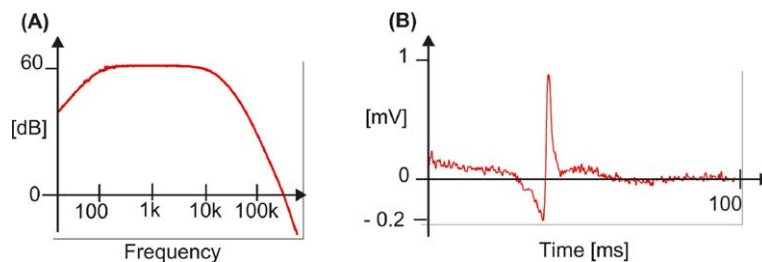


Fig. 8. Transfer function of the bandpass filter (A). Typical spike from embryonic chicken cardiomyocytes. High frequencies were cut-off at 3 kHz (B).

would reveal itself at lower frequencies, which will be the subject of future investigations. Additionally, it is interesting to note that  $n$ , often termed the frequency dispersion coefficient, does not vary with surface roughness, as has been historically assumed (De Levie, 1965). The effect of the surface roughness on impedance has been the focus of intense research efforts and has resulted in many models such as the well known pore model of de Levie, models based on surface inhomogeneities leading to a distribution of relaxation times (Brug et al., 1984), and more recently in fractal geometry-based models (Nyikos and Pajkossy, 1985; Bates and Chu, 1992). The authors concur with the work of Pajkossy, where in the frequency range investigated the capacitance dispersion is attributed to adsorption effects (Pajkossy, 1994).

### 3.3. Circuitry characterization

Stimulation circuitry operation is demonstrated by generating a square-wave stimulus on-chip. The resulting signal on a selected electrode was measured using a probe tip. The bandpass filter has been electrically characterized, using a gain-phase analyzer (HP-4194A), with results shown in Fig. 8A. Corner frequencies were measured at  $95 \pm 5$  Hz and  $72 \pm 10$  kHz. The large error in the upper corner frequency was expected because it is due to the dominant pole of the operational amplifier of the first stage. A gain of  $59.2 \pm 0.3$  dB was measured at 1 kHz. The equivalent input noise of the filter is below  $9 \text{ mV}_{\text{RMS}}$  (100 Hz–100 kHz), as was measured with a spectrum analyzer (HP-4195A).

The performance of the temperature sensor was also measured. The temperature was swept from 20 to 50 °C and a 2-point calibration was performed. The measured sensitivity is about  $210 \text{ mV}/^\circ\text{C}$  and the error is less than  $\pm 0.2^\circ\text{C}$ .

### 3.4. First biological measurements

First tests were performed with an in situ preparation of cardiomyocytes from fertilized chicken eggs at embryonic day 10. The hearts were extracted from the embryo, briefly rinsed with cold Dulbecco's PBS (Sigma D-8531,  $\text{Ca}^{2+}$  and  $\text{Mg}^{2+}$ -free) and directly transferred onto the electrodes of the chip. A typical spike is shown in Fig. 8B. DC-offsets at the electrodes were measured to be up to 1 V, which could cause saturation in the first amplification

stage. Since the time-constant of the electrochemistry at the electrode–electrolyte interface is on the order of seconds, we used the on-chip stimulation circuitry to set the electrode to a working point.

## 4. Conclusion

An extracellular monolithic recording system, with 16 platinum electrodes, fabricated in industrial CMOS-technology combined with post-CMOS processing has been presented. The circuitry architecture is structured in a modular design where a repeatable circuitry unit comprises the signal transducing electrode, a bandpass filter for immediate signal conditioning, and a buffer for stimulation. The systems incorporates data converters and a digital control unit that scans the array and provides a digital interface to the outside world. Functionality of the circuitry components according to initial specifications has been verified. We showed that the chip is able to measure signals from electrogenic cells using embryonic chicken cardiomyocytes. Electrochemical impedance spectroscopy has been used to experimentally verify an equivalent circuit model of the electrode–electrolyte interface. The representation of the macroscopic physical processes occurring during the impedance measurement by the model parameters aids in the understanding of signal transduction, and may lead to an optimized transducer design.

## Acknowledgements

The authors gratefully acknowledge funding from the Information Societies Technology (IST) European Union Future and Emerging Technologies program, contract number IST 2000-26045, and the Swiss Bundesamt fuer Bildung und Wissenschaft (BBW), contract number 00.0431.2. Iwan Schenker and Partick Schmutz provided invaluable help with impedance measurements and analysis.

## References

- Bai, Q., Wise, K.D., 2001. Single-unit neural recording with active microelectrode arrays. *Trans. Biomed. Eng.* 48 (8), 911–919.

- Bates, J.B., Chu, Y.T., 1992. Electrode–electrolyte interface impedance: experiments and model. *Ann. Biomed. Eng.* 20 (3), 349–362.
- Berdondini, L., Overstolz, T., de-Rooij, N.F., Koudelka-Hep, M., Martinoia, S., Seitz, P., Wany, M., Blanc, N., 2002. High resolution electrophysiological activity imaging of in-vitro neuronal networks. In: Proceedings of the Second Annual International IEEE-EMBS Special Topic Conference on Microtechnologies in Medicine and Biology, Madison, WI, USA, pp. 241–244.
- Borkholder, D.A., 1998. Cell based biosensors using microelectrodes. Stanford University.
- Borkholder, D.A., Bao, J., Maluf, N.I., Perl, E.R., Kovacs, G.A., 1997. Microelectrode arrays for stimulation of neural slice preparations. *J. Neurosci.* 17, 61–66.
- Brug, G.J., van den Eeden, A.L.G., Sluyters-Rehbach, M., Sluyters, J.H., 1984. The analysis of electrode impedances complicated by the presence of a constant phase element. *J. Electroanal. Chem.* 176, 275–295.
- Bucher, V., Graf, M., Steizle, M., Nisch, W., 1999. Low-impedance thin-film polycrystalline silicon microelectrodes for extracellular stimulation and recording. *Biosens. Bioelectron.* 14 (7), 639–649.
- Connolly, P., Clark, P., Curtis, A.S.G., Dow, J.A.T., Wilkinson, C.D.W., 1990. An extracellular microelectrode array for monitoring electrogenic cells in culture. *Biosens. Bioelectron.* 5, 223–234.
- De Boer, R.W., Van Oosterom, A., 1978. Electrical properties of platinum electrodes: impedance measurements and time-domain analysis. *Med. Biol. Eng. Comput.* 16 (1), 1–10.
- De Levie, R., 1965. The influence of surface roughness of solid electrode on electrochemical measurements. *Electrochim. Acta* 10, 113–130.
- DeBusschere, B.D., Kovacs, G.T.A., 2001. Portable cell-based biosensor system using integrated CMOS cell-cartridges. *Biosens. Bioelectron.* 16 (7-8), 543–556.
- Egert, U., Schlosshauer, B., Fennrich, S., Nisch, W., Fejtl, M., Knott, T., Muller, T., Hammerle, H., 1998. A novel organotypic long-term culture of the rat hippocampus on substrate-integrated multielectrode arrays. *Brain Res. Protoc.* 2 (4), 229–242.
- Eversmann, B., Jenkner, M., Paulus, C., Hofmann, F., Brederlow, R., Fromherz, P., Brenner, F., Schreiter, M., Gabl, R., Plehnert, K., Steinhäuser, M., Eckstein, G., Schmitt-Landsiedel, D., Thewes, R., 2003. A 128 × 128 CMOS bio-sensor array for extracellular recording of neural activity. 2003 IEEE Int. Solid State Circuits Conf., 222–223.
- Franks, W., Heer, F., McKay, I., Taschini, S., Sunier, R., Hagleitner, C., Hierlemann, A., Baltes, H., 2003. CMOS monolithic microelectrode array for stimulation and recording of natural neural networks. *Transducers 2003*, Boston, pp. 963–966.
- Fricke, H., 1932. The theory of electrolytic polarization. *Philos. Mag.* 7 (14), 310–318.
- Gilchrist, K.H., Barker, V.N., Fletcher, L.E., DeBusschere, B.D., Ghannouni, P., Giovangrandi, L., Kovacs, G.T.A., 2001. General purpose, field-portable cell-based biosensor platform. *Biosens. Bioelectron.* 16, 557–564.
- Grahame, D.C., 1952. Mathematical theory of the Faradaic admittance. *J. Electrochem. Soc.* 99 (12), 370C–385C.
- Gross, G.W., 1979. Simultaneous single unit recording in vitro with a photoetched laser deinsulated gold multimicroelectrode surface. *IEEE Trans. Biomed. Eng.* BME-26 (5), 273–279.
- Gross, G.W., Rhoades, B.K., Reust, D.L., Schwalm, F.U., 1993. Stimulation of monolayer networks in culture through thin-film indium-tin oxide recording electrodes. *J. Neurosci. Methods* 50 (2), 131–143.
- Gross, G., Rhoades, B.K., Azzazy, H.M.E., Ming Chi, W., 1995. The use of neuronal networks on multielectrode arrays as biosensors. *Biosens. Bioelectron.* 10 (6-7), 553–567.
- Heuschkel, M.O., Fejtl, M., Ragenbass, M., Bertrand, D., Renaud, P., 2002. A three-dimensional multi-electrode array for multi-site stimulation and recording in acute brain slices. *J. Neurosci. Methods* 114 (2), 135–148.
- Jenkner, M., Muller, B., Fromherz, P., 2001. Interfacing a silicon chip to pairs of snail neurons connected by electrical synapses. *Biol. Cybern.* 84 (4), 239–249.
- Jimbo, Y., Robinson, H.P., 2000. Propagation of spontaneous synchronized activity in cortical slice cultures recorded by planar electrode arrays. *Bioelectrochemistry* 51 (2), 107–115.
- Keefer, E.W., Gramowski, A., Gross, G.W., 2001a. nMDA receptor-dependent periodic oscillations in cultured spinal cord networks. *J. Neurophysiol.* 86, 3030–3042.
- Keefer, E.W., Gramowski, A., Stenger, D.A., Pancrazio, J.J., Gross, G.W., 2001b. Characterization of acute neurotoxic effects of trimethylolpropane phosphite via neuronal network biosensors. *Biosens. Bioelectron.* 16 (7-8), 513–525.
- Kovacs, G.T.A., 1994. Introduction to the theory, design, and modeling of thin-film microelectrodes for neural interfaces. In: Stenger, D.A., McKenna, T.M. (Eds.), *Enabling Technologies for Cultured Neural Networks*. Academic Press, London, pp. 121–165.
- Kovacs, G.T.A., 2003. Electronic sensors with living cellular components. *Proc. IEEE* 91 (6), 915–929.
- Maher, M.P., Pine, J., Wright, J., Yu Chong, T., 1999. The neurochip: a new multielectrode device for stimulating and recording from cultured neurons. *J. Neurosci. Methods* 87 (1), 45–56.
- Marom, S., Shahaf, G., 2002. Development, learning and memory in large random networks of cortical neurons: lessons beyond anatomy. *Q. Rev. Biophys.* 35 (1), 63–87.
- McAdams, E.T., Jossinet, J., 1994. Physical interpretation of Schwan's limit voltage of linearity. *Med. Biol. Eng. Comput.* 32 (2), 126–130.
- McAdams, E.T., Lackermeier, A., McLaughlin, J.A., Macken, D., Jossinet, J., 1995. The linear and non-linear electrical properties of the electrode–electrolyte interface. *Biosens. Bioelectron.* 10 (1-2), 67–74.
- McFadden, P., 2002. Broadband biodetection: Holmes on a chip. *Science* 297, 2075–2076.
- Morefield, S.I., Keefer, E.W., Chapman, K.D., Gross, G.W., 2000. Drug evaluations using neuronal networks cultured on microelectrode arrays. *Biosens. Bioelectron.* 15 (7-8), 383–396.
- Multi Channel Systems MCS, GmbH, Reutlingen, Germany.
- Nyikos, L., Pajkossy, T., 1985. Fractal dimension and fractional power frequency-dependent impedance of blocking electrodes. *Electrochim. Acta* 30 (11), 1533–1540.
- Onaral, B., Schwan, H.P., 1982. Linear and nonlinear properties of platinum electrode polarisation. I. Frequency dependence at very low frequencies. *Med. Biol. Eng. Comput.* 20 (3), 299–306.
- Pajkossy, T., 1994. Impedance of rough electrodes. *J. Electroanal. Chem.* 364, 111–125.
- Pancrazio, J.J., Bey Jr., P.P., Cuttino, D.S., Kusel, J.K., Borkholder, D.A., Shaffer, K.M., Kovacs, G.T.A., Stenger, D.A., 1998a. Portable cell-based biosensor system for toxin detection. *Sens. Actuators B Chem.* B53 (3), 179–185.
- Pancrazio, J.J., Bey Jr., R.P., Loloee, A., Manne, S., Chao, H.C., Howard, L.L., Milton-Gosney, W., Borkholder, D.A., Kovacs, G.T.A., Manos, P., Cuttino, D.S., Stenger, D.A., 1998b. Description and demonstration of a CMOS amplifier-based-system with measurement and stimulation capability for bioelectrical signal transduction. *Biosens. Bioelectron.* 13 (9), 971–979.
- Pancrazio, J.J., Whelan, J.P., Borkholder, D.A., Ma, W., Stenger, D.A., 1999. Development and application of cell-based biosensors. *Ann. Biomed. Eng.* 27, 687–711.
- Pourbaix, M., 1974. *Atlas of Electrochemical Equilibria in Aqueous Solutions*. National Association of Corrosion Engineers, Brussels.
- Prinz, A.A., Fromherz, P., 2000. Electrical synapses by guided growth of cultured neurons from the snail *Lymnaea stagnalis*. *Biol. Cybernet.* 82 (4), L1–L5.
- Shahaf, G., Marom, S., 2001. Learning in networks of cortical neurons. *J. Neurosci.* 21 (22), 8782–8788.
- Streit, J., Tschertner, A., Heuschkel, M.O., Renaud, P., 2001. The generation of rhythmic activity in dissociated cultures of rat spinal cord. *Eur. J. Neurosci.* 14 (2), 191–202.
- Thiebaud, P., Beuret, C., Koudelka-Hep, M., Bove, M., Martinoia, S., Grattarola, M., Jahnsen, H., Rebaudo, R., Balestrino, M., Zimmer, J.,

- Dupont, Y., 1999. An array of Pt-tip microelectrodes for extracellular monitoring of activity of brain slices. *Biosens. Bioelectron.* 14 (1), 61–65.
- Thomas, C.A., Springer, P.A., Loeb, G.E., Berwald-Netter, Y., Okun, L.M., 1972. A miniature microelectrode array to monitor the bioelectric activity of cultured cells. *Exp. Cell Res.* 74, 61–66.
- Tscherter, A., Heuschkel, M.O., Renaud, P., Streit, J., 2001. Spatiotemporal characterization of rhythmic activity in rat spinal cord slice cultures. *Eur. J. Neurosci.* 14 (2), 179–190.
- van der Schalie, W.H., Gardner, H.S., Bantle, J.A., de Rosa, C.T., Finch, R.A., Reif, J.S., Reuter, R.H., Backer, L.C., Burger, J., Folmar, L.C., Stokes, W.S., 1999. Animals as sentinels of human health hazards of environmental chemicals. *Environ. Health Perspect.* 107 (4), 309–315.
- Yeager, E., 1984. Electrocatalysts for O<sub>2</sub> reduction. *Electrochim. Acta* 29 (11), 1527–1537.
- Zeck, G., Fromherz, P., 2001. Noninvasive neuroelectronic interfacing with synaptically connected snail neurons immobilized on a semiconductor chip. *Proc. Natl. Acad. Sci. U.S.A.* 98 (18), 10457–10462.



---

# APPENDIX C

## **SELF- ASSEMBLED STRUCTURES FOR PATTERNED CELL ADHESION ON A CMOS CELL-BASED BIOSENSOR**

W. Franks, S. Tosatti\*, F. Heer, P. Seif, M. Textor\*, A. Hierlemann

Physical Electronics Laboratory, Swiss Federal Institute of Technology (ETH), Zurich, 8092, Zurich, Switzerland

\*BioInterfaces Group, Swiss Federal Institute of Technology (ETH), Zurich, 8092, Zurich, Switzerland

Prepared for: Biosensors and Bioelectronics

# Self-Assembled Structures for Patterned Cell Adhesion on a CMOS Cell-based Biosensor

W. Franks, S. Tosatti, F. Heer, P. Seif, M. Textor, A. Hierlemann

## Abstract

In this article we present a cell-based biosensor that combines CMOS circuitry with sophisticated surface patterning to guide cell adhesion. Motivating this work is the need to understand the propagation of electrical activity through a defined region of heart muscle cells to help elucidate the underlying mechanisms in arrhythmias and other cardiac phenomena. The CMOS biosensor comprises an array of electrodes with on-chip circuitry to stimulate and measure activity from electrogenic cardiomyocytes. To confine cell adhesion to specific locations over the electrode array, an engineered surface for high-contrast protein adsorption and, hence, cell attachment has been developed. Surface functionalization is based on site-selective molecular-assembly patterning. An amine-terminated self-assembled monolayer is used to define areas of cell adhesion. A protein-repellent grafted copolymer, poly(L-lysine)-*graft*-poly(ethylene glycol) (PLL-*g*-PEG), is used to render the surrounding silicon dioxide resistant to protein adsorption. X-ray photoelectron spectroscopy, scanning ellipsometry and fluorescence microscopy techniques were used to monitor the individual steps of the patterning process. Successful guided growth using these layers is demonstrated with primary neonatal rat cardiomyocytes, up to 4 days in vitro, and with the HL-1 cardiomyocyte cell line, up to 7 days in vitro. The advantage of these self-organized systems is that high-resolution, biomimetically engineered surfaces can be realized using a simple, cost-effective, dip-and-rinse process.

## Introduction

As advances in microelectronic fabrication reduced feature sizes to the same dimensions as biological entities, a new field of research combining biology and electronics was created. Within this field is a body of work dedicated to the engineering and application of cell-based biosensors, whose innate ability to take advantage of naturally evolved selectivity to analytes yielding a physiologically relevant response gives rise to a broad spectrum of applications ranging from environmental monitoring to drug discovery (Pancrazio et al., 1999). Furthermore, cell-based biosensors combined with cell-patterning capabilities to selectively guide cell adhesion to specific regions facilitate the design of in vitro models that may more accurately mimic the in vivo situation, potentially obviating the need for expensive and complicated whole animal experiments (van der Schalie et al., 1999, Thomas et al., 2000).

Strategies to guide cell adhesion include micro-contact printing (Kane et al., 1999, Branch et al., 2000, Scholl et al., 2000, Whitesides et al., 2001), ink-jet printing (Sanjana and Fuller, 2004), microfluidic channels (Griscom et al. 2002, Martinoia et al., 1999), perforated microelectrodes (Greve et al., 2003) and photolithography (Sorribas et al., 2002, Wyart et al., 2002, Rohr et al., 1991). While these systems offer advantages such as flexibility (ink-jet printing), inexpensive processing (micro-contact printing) and high resolution (photolithography, perforated metal microelectrodes), they are limited in terms of either alignment to the underlying biosensor electrodes, thickness of the chemical

adhesion layers or ease of processing. Selective molecular assembly patterning (SMAP) has the advantages that: (i) high-resolution structures are determined by the resolution of thin-film gold patterning, which, due to the thinness of the required gold film (~ 90nm), are easy to achieve in a lift-off process; (ii) the process requires no further alignment; (iii) molecularly thin chemical layers minimize the cell membrane-electrode gap reducing distortions to extracellularly recorded signals; (iv) the protein-resistant background negates the need for serum-free media; (v) and finally the dip-and-rinse processing is both simple and cost-effective (Michel et al., 2002).

To accurately follow signal propagation through the cell culture the biosensor ideally comprises a high-density electrode array with integrated circuitry. This can only be achieved using microelectronic circuitry technology, such as an industrial CMOS (complementary metal oxide semiconductor) process. On-chip circuitry offers the following features: multiplexing capabilities which translate into an array size that is not limited by the number of available interconnects; signal amplification and filtering can be performed as close to the signal source as possible, reducing electromagnetic noise distortions that are introduced as the signal travels through wires and interconnects, so that the recorded signal fidelity is improved; and analog to digital conversion results in a robust digital signal that is fed directly from the sensor to a PC (Heer et al., 2004).

The combination of guided cell adhesion and on-chip CMOS circuitry results in a device that finds a myriad of applications in the field of cardiology. For example, investigations concerning the electrical propagation of cardiac impulses have been performed with microelectrode arrays (MEAs, Kucera et al., 2000), and with chemically and mechanically patterned glass coverslips (Rohr et al., 1991, Bursac et al., 2002, Thomas et al., 2003, Rohr et al., 2003), which employ high-resolution optical mapping and voltage-sensitive florescent dyes to detect electrical events. Research with these tools has shown that in vitro models comprising monolayers of cardiomyocytes grown in controlled and reproducible anisotropic structures (i.e. longitudinally shaped cells aligned to a chemical or physical pattern) can help elucidate the poorly understood relationship between anatomic substrates and electrical signal propagation, an important mechanism in arrhythmias (Bursac et al., 2002, Thomas et al., 2000).

In this article we present the combination of both sophisticated surface patterning for high-contrast protein adsorption, and cell-attachment, with a cell-based biosensor realized in state-of-the-art CMOS technology. We have used the well-known gold-thiol system, specifically an amine-terminated alkane thiol self-assembled monolayer (SAM), to define areas of cell attachment. The amine-terminated SAM was selected because it mimics poly-L-lysine, a known cell-adhesion promoter with a terminal group (Freshney 2000). It has also been shown that amine groups promote neural adhesion and development (Stenger and McKenna, 1994, Kleinfeld et al., 1988). A protein-repellent grafted copolymer, poly(L-lysine)-*graft*-poly(ethylene glycol) (PLL-*g*-PEG) is used to render the surrounding silicon dioxide resistant to non-specific protein adsorption (Michel et al., 2002, Lussi et al., 2004), see Fig. 1. Although not yet completely understood, the protein resistance of PEG brush surfaces is frequently attributed to exclusion effects or steric stabilization (Harris 1992, Harris, 1997). In recent publications (Kenausis et al., 2000,

Huang et al., 2001, Huang et al., 2002, Pasche, et al., 2003), it has been shown that the polycationic PLL-g-PEG attaches strongly to negatively charged metal oxides by coulombic interactions via its positively charged poly-L-lysine backbone (pKa ~10.5), presenting a dense brush of PEG chains and thus reducing protein adsorption from full blood serum to values typically less than 5 ng/cm<sup>2</sup> (Tosatti, et al., 2003). X-ray photoelectron spectroscopy and scanning ellipsometry techniques were used to monitor the step-by-step self-assembly processes, thereby confirming successful depositions of the polymeric monolayers. Our results show that the chemical patterns define the location of adherent primary neonatal rat cardiomyocytes for up to 4 days in vitro (DIV), and HL-1 cardiomyocytes, a cell line, for up to 7 days in vitro.

## **Materials and Methods**

### *Fabrication of gold-patterned test chips*

For surface analysis purposes, test chips with various gold patterns were first fabricated on blank glass and silicon wafers before the process was applied to the CMOS biosensor. Due to the native oxide layer on silicon, the surfaces of the glass and silicon wafers are considered to be chemically equivalent. Two different designs were used: a 14 x 14 mm<sup>2</sup> chip half native SiO<sub>2</sub>, half gold (design 1, silicon starting material, see Fig. 2); and a 2 x 2 cm<sup>2</sup> chip with varying gold structures detailed below (design 2, glass starting material, see Fig. 3). Design 1 was used for surface analysis (large measurement areas were required for the scanning ellipsometry and XPS measurements) and design 2 was used to test the efficacy of cell patterning and to explore processing capabilities, as discussed below. As a means of process control, at least 2 chips of design 1 were simultaneously processed along side design 2 chips and analyzed using scanning ellipsometry.

Starting with a bare glass or silicon wafer, 8 nm of Cr followed by 80 nm of gold was deposited by evaporation and structured in a lift-off process. To protect the wafer from dust during the dicing process, a layer of photoresist was spun-coated on the wafer. The wafer was diced and the individual chips were cleaned with acetone, isopropanol and deionized water. The geometries of the gold pattern were designed to determine the minimum line width in which the cells would form a confluent strand, as well as the minimum gap, the electrically isolating spacing between the electrode and the gold paths (see Fig. 1), that the cells would grow over, thereby preserving electrical continuity through a defined strand of cells. Additionally, it was necessary to determine the minimum spacing between gold regions that could be achieved in the lift-off process. The widths of the gold paths ranged from 20 to 300 μm, and the gaps between gold regions ranged from 3 to 150 μm, see Fig. 3.

### *Selective molecular assembly patterning*

A brief description of the surface functionalization is given here (for a complete description of PLL-g-PEG synthesis and characterization the reader is referred to Pasche et al., 2003). To ensure that the substrate surface is free of organic residue, the chips were sonicated for 10 min. in isopropanol, dried in a nitrogen stream and exposed to UV radiation for 30 min. It was necessary to first functionalize the surface with the amine-

terminated SAM to block the PLL-*g*-PEG from adhering to the gold surface; however, unless precautions were taken the amine group of the SAM, with its positive charge at neutral pH due to protonation, would adhere to the negatively charged SiO<sub>2</sub>. As a result two strategies for the SAM deposition were initially pursued: the first was to choose an appropriate solvent, such as ammonia in methanol, that would prevent protonation of the amine group. The second was to use an aminoalkanethiol whose amine group is protected by a neutrally charged group, 9-fluorenylmethoxycarbonyl (Fmoc, commercially available from Dojindo Molecular Technologies, Japan), which can be later removed using piperidine in acetonitrile. Both these strategies were attempted and results showed that the unprotected SAM did not adsorb significantly on the SiO<sub>2</sub>, hence the strategy with the Fmoc aminoalkanethiol, with its extra processing step to remove the Fmoc group, was not further developed. For the unprotected SAM deposition, the chips were allowed to incubate for 48 hours at room temperature in a solution of 0.5 molar aminoundecanethiol (HS(CH<sub>2</sub>)<sub>11</sub>NH<sub>2</sub>•HCl, commercially available from Prochimia, Poland) in 0.5 molar ammonia in methanol. The chips were then rinsed with methanol and dried in a nitrogen stream. The chips were placed gold side down in a drop composed of 0.25mg/ml PLL(20)-[3.5]-PEG(2) in 10mM 4-(2-hydroxyethyl)piperazine-1-ethanesulfonic acid (HEPES) and 150 mM NaCl buffer solution (adjusted to pH 7.4 with a 6.0 M NaOH solution, total ionic strength 160 mM) for 45 min., rinsed with de-ionized water and dried with nitrogen. For sterilization in preparation for cell culturing, the chips were immersed in 70% ethanol for ~ 2 min. and dried with nitrogen in a sterile environment. Immediately following surface preparation the samples were analyzed and/or plated with cells.

For sensitive cells, which would not adhere and differentiate properly with only an amine group as the adhesion factor, a strategy involving an additional treatment with a protein adhesion promoter was pursued. Immediately following surface functionalization, samples were incubated in 0.02% gelatin in PBS for 30 min. The gelatin should adhere to the gold side only, presenting to the cells a suitable surface for adhesion and differentiation.

### *Surface Analysis*

The surfaces were characterized at each step of the molecular assembly patterning process using both scanning ellipsometry and X-ray photoelectron spectroscopy (XPS). All XPS spectra were recorded with a SAGE 100 system (Specs, Germany), with a non-monochromatized Al K $\alpha$  radiation source set to 320 W (13 kV) and a take-off angle of 90°. An electron-energy pass detector of 50 eV was used for low-resolution survey spectra, and 14 eV for high-resolution element surveys. The sensitivity factors of Scofield (Scofield, 1976) were used to determine the quantitative surface compositions. All peaks were referenced to the main hydrocarbon peak (C1s, C-C, C-H) binding energy of 285.0 eV.

Scanning ellipsometry was used to measure the thickness of the organic layers. Amplitude and phase change curves generated at incidence angles of 65, 70 and 75° were fitted using the Cauchy approximation with A = 1.45, B = 0.01 and C = 0.0 (Palik, 1985). For the SiO<sub>2</sub> surfaces the index of refraction was taken from literature (Palik, 1985), and

for gold it was determined by fitting the experimental results obtained from freshly cleaned substrates.

### *Cell Culturing*

Two different cardiomyocyte cell types were used to test the efficacy of the surface patterning: primary neonatal rat cardiomyocytes (NRC) and the HL-1 immortalized cell line. The NRC's were taken from 3 day old rats and harvested according to Auerbach et al., 1999. Cells were seeded in plating medium consisting of 68% DMEM (Amimed, Switzerland), 17% Medium M199 (Amimed), 10% horse serum (Life Technologies, USA), 5% fetal calf serum (Life Technologies), 4 mM glutamine (Amimed), and 1% penicillin-streptomycin (Amimed). After 24 h the plating medium was exchanged for maintenance medium, consisting of 78% DMEM (Amimed), 20% Medium M1999 (Amimed), 1% horse serum (Life Technologies), 1% penicillin-streptomycin (Amimed), and 4 mM glutamine, (Amimed).

The HL-1 cell line was kindly provided by Dr. W. Claycomb at the Louisiana State University Health Science Center (White et al., 2004). The cells are maintained in Claycomb Medium (JRH Biosciences, USA) supplemented with 10% fetal bovine serum (JRH Biosciences, USA), 100 units/ml penicillin (Sigma, USA), 100 µg/ml streptomycin (antibiotic/antimycotic solution, Invitrogen, USA), 0.1 mM norepinephrine (Sigma, U.S.A.) and 2.0 mM L-glutamine (Sigma, USA), which was changed approximately every 24 h. Standard incubation conditions of 37 °C, 5% CO<sub>2</sub>, 95% air and 95% relative humidity are used. Both cells types are spontaneously beating, which is confirmed by a visual inspection. Cells were seeded at a density of approximately 1.5(10)<sup>5</sup> cells/cm<sup>2</sup>.

The cells were fixed using 4% paraformaldehyde in phosphate buffered saline (PBS), the membrane was permeabilized with 0.2% Triton X-100 (AppliChem, Germany) and the nucleus and actin filaments were stained with 4', 6'-diamidine-2 phylindole dihydrochloride (DAPI, Sigma) and Alexa Fluor 488 phalloidin (Molecular Probes, U.S.A.), respectively.

## Results

### *Surface Analysis*

Scanning ellipsometry and XPS analyses were performed using design 1 samples immediately following cleaning as well as after each step in the surface functionalization process, see Fig. 2.

### XPS

C1s XPS spectra were used to determine whether the amine-terminated SAM and PLL-g-PEG organic layers were appropriately present at the sample surface. Figure 4 shows the C1s XPS spectra for the gold and SiO<sub>2</sub> sides of design 1, as measured immediately following SAM deposition (top curves) and following adsorption of PLL-g-PEG (bottom curves). Labeled on the figure are the C1s binding energies of C-C, C-N, C-O and C-S moieties. The noisy scan represents the experimental curve, the smooth lines the results of curve fitting, as indicated on the figure. Following the adsorption of PLL-g-PEG, the relative intensity of the C1s (C-C) peak on the gold side decreased, while the relative

intensity of the corresponding peak originating from C-N, C-O and C-S increased slightly. On the SiO<sub>2</sub> side, the relative intensity of the C1s (C-C) peak decreased following PLL-*g*-PEG adsorption, while that of the C-N, C-O, and C-S contributions increased significantly. Table 1 gives the elemental composition of both layers after the various processing steps, and of the SAM and PLL-*g*-PEG controls (without any preceding or subsequent processing steps).

### Scanning Ellipsometry

Ellipsometry results of the cleaned surface (design 1) were used to measure the thickness of the native oxide, found to be  $20.5 \pm 7.8 \text{ \AA}$  ( $n = 22$ ), and to determine the indices of refraction of the gold. Following the application of the amine-terminated thiol, the organic layer thickness was found to be  $18.9 \pm 4.1 \text{ \AA}$  ( $n = 6$ ) on gold, and  $5.3 \pm 1.1 \text{ \AA}$  ( $n = 6$ ) on SiO<sub>2</sub>, Fig. 2. After the adsorption of the PLL-*g*-PEG, the average organic layer thickness on the gold side increased slightly to  $20.0 \pm 6.0 \text{ \AA}$  ( $n = 6$ ), while that on the SiO<sub>2</sub> side was determined to be  $14.4 \pm 1.2 \text{ \AA}$  ( $n = 6$ ). A larger set of samples were analyzed only at the end of the process yielding an organic layer thickness of  $15.39 \pm 4.65 \text{ \AA}$  ( $n = 19$ ) for the SAM and  $13.0 \pm 1.8 \text{ \AA}$  ( $n = 19$ ) for the PLL-*g*-PEG.

The gelatin coating increased the organic layer thickness on the gold side by  $\sim 120\%$ , while the organic layer on the SiO<sub>2</sub> side increased by only 13%.

Scanning ellipsometry was also used to determine the effect of the sterilization procedure on the thickness of the organic layers. For the case of the gold side, no change was detected, while the PLL-*g*-PEG thickness increased slightly, by  $\sim 13\%$ .

### Guided Cell Growth

Guided cell growth was first demonstrated with the HL-1 cardiomyocytes and the design 1 chips, see Fig. 5(A). Initially the seed cells would cover the entire chip, however after 24 hours the cells on the PLL-*g*-PEG would slide off the chips when the culture dish was gently moved back and forth. These non-adhering cells would then be removed when the medium was changed (although no movement of the culture dish was necessary to ensure that these cells were removed). The instances of small groups of cells adhering to the PLL-*g*-PEG side was less than 20 over the entire area of  $\sim 2 \text{ cm}^2$ . Instances of isolated cells or cell debris attached to the SiO<sub>2</sub> side are indicated by the white arrows in Fig. 5(B). When chemically patterned chips were incubated in gelatin, no difference in cell adhesion from those that were not treated with gelatin, was observed.

Fluorescence microscopic images of the HL-1 cells and NRC's are shown in Figs. 6, 7, and 8. Fig. 6 shows areas of predominantly gold interrupted with an increasingly wide SiO<sub>2</sub> line. The purpose is to demonstrate that cells can grow over thin regions of PLL-*g*-PEG-coated SiO<sub>2</sub>, which are necessary for electrical isolation, as mentioned previously. In the case shown here, the cells can grow over SiO<sub>2</sub> lines of up to 10  $\mu\text{m}$  in width, while they are stopped by a 20  $\mu\text{m}$  wide SiO<sub>2</sub> line. Fig. 6 answers the question *what is the minimum gold line width required for a continuous strand of cells?* Gold line widths (black in the figure) ranging from 30 to 210  $\mu\text{m}$  are shown. In this case, the NRC monolayer (4 DIV) becomes continuous at 60  $\mu\text{m}$  wide lines. The white regions are SiO<sub>2</sub>.

Fig. 7 shows two gold lines (black) surrounded by SiO<sub>2</sub> (white) with areas that are electrically isolated by a 5 or 10 μm gap in the gold forming square electrodes. These electrodes are to be aligned with the electrodes on the CMOS chip. The white arrow indicates a 10 μm gap in the gold. Once again, the cells grow in clearly defined strands following the SAM-coated gold lines.

In the final phase of experimentation, the gold pattern was deposited onto the CMOS chip, which was subsequently functionalized and seeded with primary neonatal rat cardiomyocytes. Fig. 9 shows strands of the NRCs at 4 DIV following the gold lines. In this figure few spots of individual cells, or cell debris, are visible.

## Discussion

### *Surface Analysis*

An analysis of the carbon spectra for both sides of the design 1 indicates that the SAM has been assembled on the gold and that PLL-*g*-PEG has been adsorbed on the SiO<sub>2</sub>. The large C-C peak on the gold side following SAM deposition indicates the presence of the aminethiol. The small peak at a slightly higher binding energy may be attributed to the C-S bond in the mercapto group and the C-N bond in the amine group. Based on stoichiometry, the expected elemental concentration of N and S is 4.2 %, however only 1.2 and 1.3, respectively, was measured (Tab. 1). This deviation can be attributed to experimental errors due weak signal intensity. Following exposure to the PLL-*g*-PEG solution, the peak at 286.5 eV significantly increases. This is primarily attributed to the C-O bond in the glycol group, indicating that PLL-*g*-PEG has indeed adsorbed to the surface. On the gold side, the peak at 286.5 eV also increases following PLL-*g*-PEG adsorption, albeit less than on the SiO<sub>2</sub> side, which is likely a result of small amounts of PLL-*g*-PEG residue remaining on the SAM, as is corroborated by the ellipsometry results.

The elemental analysis is used to compare the composition between the SAM and PLL-*g*-PEG controls, i.e. without proceeding or subsequent processing, and the layers as processed in this work. A comparison between columns 1 and 3 of Tab. 1 shows that the composition of the layers is relatively constant regardless of other processing steps.

The organic layer thicknesses for the SAM and PLL-*g*-PEG of < 20 Å are the expected values for a monolayer. Some unspecific adsorption of the SAM onto the SiO<sub>2</sub> occurs, however it is believed that these molecules are subsequently replaced by the PLL-*g*-PEG (Huang, et al., 2001 have shown that PLL-*g*-PEG displaces contaminations). The relatively large variation in the ellipsometry results for the amino-terminated alkanethiol thickness is attributed to surface roughness, which is large relative to the SAM thickness leading to measurement error. The slight increase, 6 %, in organic film thickness on the gold side following PLL-*g*-PEG application is considered to be due to PLL-*g*-PEG residue and is seen in the C1s XPS spectra discussed above.

The large increase in organic layer thickness (120%) on the gold side, and the small increase on the SiO<sub>2</sub> side (13 %), following incubation in gelatin demonstrates that the PLL-*g*-PEG is capable of repelling gelatin protein adsorption. Using 70% ethanol to



sterilize the chemically patterned samples appears to have a negligible effect on the coatings composition and thickness.

### *Guided Cell Growth*

Design 2 was used to investigate the effect of various dimensions. The cells grow over frame widths of 5 – 10  $\mu\text{m}$ , a dimension that is easily achieved in our in-house processing facilities. Fig. 7 shows that the cells start to form continuous strands when the gold line width is 60  $\mu\text{m}$  or greater. The pattern was successfully transferred to the CMOS chip, where cell growth could be located at the measurement electrodes. It should be noted, that any conclusions drawn from this work regarding the effective line widths, etc. are only valid for the cell types and seeding densities investigated in this work. These dimensions are expected to vary with cell diameter and transmembrane proteins.

Another critical parameter is the effectiveness of the chemical patterns. In all cases the cells were plated on the samples as soon after their preparation as possible, typically within 24 hours, and when longer the samples were stored at 4 °C. It was noticed that the coatings would lose their efficaciousness with time, ie. after 2 weeks under ambient conditions. In terms of culture lifetime, the coatings guided cell adhesion up to 7 DIV, at which point the experiment was terminated. For NRCs this is ample time since the cells exhibit visible contractions 1 or 2 days after plating and begin to delaminate from the surface at 5 - 7 DIV. Once again the required length of time for pattern fidelity will vary with cell type.

It was observed that few islands of cells formed on the PLL-*g*-PEG regions. These can be attributed to small scratches or incongruities in the layer that occurred during processing, or they could be due to cell fragments that have been stained. In any case, these incidences are few and isolated, and would not affect electrophysiological measurements through the patterned strands of cells.

The observation that cell growth is selective even when the samples have been incubated in gelatin is expected, since the PLL-*g*-PEG should be resistant to the gelatin protein. This indicates that these coatings could be used to guide the attachment of cells that are more sensitive to the surface, such as neurons. For example, the functionalized surface could be first treated with Matrigel or laminin to promote neural adhesion at the desired locations, followed by a selective wash to remove the adhesion promoter in the PEGylated areas.

### Conclusions and Outlook

We have demonstrated that the chemical patterning presented here can be used to guide the adhesion of HL-1 cardiomyocytes and neonatal rat cardiomyocytes. The coatings were able to guide the attachment of the NRCs and HL-1 cells for up to 4 and 7 DIV, respectively, at which point the experiments were terminated. Visible contractions of the NRCs indicate that normal cell function is conserved when the cells are cultured on the SAM-treated gold. Both of these cell types can bridge across 10  $\mu\text{m}$  wide lines of PLL-*g*-PEG-functionalized  $\text{SiO}_2$ . The gold pattern was applied to a CMOS chip, to create gold

pathways defining continuous strands of cells with electrode areas that were aligned to the CMOS electrodes, yet electrically isolated from the bulk of the gold pathway.

The next phase of this work will be to use this system to extracellularly measure the signal propagation velocity through a defined strand of cells. Also of interest will be to test adhesion patterning with other cell types such as neurons. Initial results show that this type of surface patterning can guide the adhesion of glia cells, which are typically present in neural cultures, for at least 3 weeks in vitro. The effectiveness of the coatings with neuron adhesion promoters such as Matrigel and laminin shall also be investigated.

#### Acknowledgements

The authors would like to thank Professor Henry Baltes for sharing laboratory resources and for his ongoing, stimulating interest in our work. The authors are grateful to Stéphanie Pasche, ETH Zurich, for providing the PLL-*g*-PEG, Dr. William Claycomb, Louisiana State University Medical Center, for supplying the HL-1 cardiomyocyte cell line, Evelyne Perriard, ETH Zurich, for expertise with NRC culturing and Heike Hall, ETH Zurich, for general advise on cell culturing. Funding has been generously provided by the Information Societies Technology (IST) European Union Future and Emerging Technologies program, contract number IST 2000-26045, and the Swiss Bundesamt für Bildung und Wissenschaft (BBW), contract number 00.0431.2.

#### References

- Alberts, B., Bray, D., Lewis, J., Raff, M., Roberts, K., Watson, J., 1994. *The Cell*, Garland Publishing.
- Auerbach, D., Bantle, S., Keller, S., Hinderling, V., Leu, M., Ehler, E., Perriard, J. C., 1999. Different domains of the M-band protein myomesin are involved in myosin binding and M-band targeting. *Mol. Biol. Cell* 10(5), 1297-1308.
- Branch, D. W., Wheeler, B. C., Brewer, G. J., Leckband, D. E., 2000. Long-term maintenance of patterns of hippocampal pyramidal cells on substrates of polyethylene glycol and microstamped polylysine. *IEEE Transactions on Biomedical Engineering* 47(3), 290-300.
- Bursac, N., Parker, K. K., Iravanian, S., Tung, L., 2002. Cardiomyocyte cultures with controlled macroscopic anisotropy: a model for functional electrophysiological studies of cardiac muscle. *Circ. Res.* 91(12), e45-54.
- Cheek, E. R., Fast, V. G., 2004. Nonlinear changes of transmembrane potential during electrical shocks: role of membrane electroporation. *Circ. Res.* 94(2), 208-214.
- Freshney, R. I., 2000. *Culture of Animal Cells*, Wiley-Liss, Weinheim.
- Greve, F., Lichtenberg, J., Hall, H., Hierlemann, A. Baltes, H., 2003. Physical immobilization and polymeric microchannel networks to achieve defined neuronal networks structures. *Micro Total Analysis Systems*, California, USA, 327-330.
- Griscom, L., Degenaar, P., LePioufle, B., Tamiya, E., Fujita, H., 2002. Techniques for patterning and guidance of primary culture neurons on micro-electrode arrays. *Sensors and Actuators B (Chemical)* 83(1-3), 15 – 21.
- Heer, F., Franks, W., Blau, A., Taschini, S., Ziegler, C., Hierlemann, A., and Baltes, H. (2004). "CMOS microelectrode array for the monitoring of electrogenic cells."

- Biosensors and Bioelectronics, 20(2), 358-366.
- Huang, N., Voros, J., DePaul, S., Textor, M., Spencer, N., 2002. Biotin-derivatized poly(L-lysine)-g-poly(ethylene glycol): A novel polymeric interface for bioaffinity sensing. *Langmuir* 18(1), 220-230.
- Huang, N. P., Michel, R., Voros, J., Textor, M., Hofer, R., Rossi, A., Elbert, D., Hubbell, J., Spencer, N., 2001. Poly(L-lysine)-g-poly(ethylene glycol) layers on metal oxide surfaces: Surface-analytical characterization and resistance to serum and fibrinogen adsorption. *Langmuir* 17(2), 489-498.
- Kane, R. S., Takayama, S., Ostuni, E., Ingber, D. E., Whitesides, G. M., 1999. Patterning proteins and cells using soft lithography. *Biomaterials* 20(23-24), 2363-2376.
- Kenausis, G., Voros, J., Elbert, D., Huang, N., Hofer, R., Ruiz-Taylor, L., Textor, M., Hubbell, J., Spencer, N., 2002. Poly(L-lysine)-g-poly(ethylene glycol) layers on metal oxide surfaces: Attachment mechanism and effects of polymer architecture on resistance to protein adsorption. *Journal of Physical Chemistry B* 104(14), 3298-3309.
- Kleinfeld, D., Kahler, K., and Hockberger, P. (1988). "Controlled outgrowth of dissociated neurons on patterned substrates." *J. Neurosci.*, 8(11), 4098-4120.
- Kucera, J. P., Heuschkel, M. O., Renaud, P., Rohr, S., 2000. Power-law behavior of beat-rate variability in monolayer cultures of neonatal rat ventricular myocytes. *Circ Res* 86(11), 1140-1145.
- Lussi, J. W., Michel, R., Reviakine, I., Falconnet, D., Goessl, A., Csucs, G., Hubbell, J. A., Textor, M., 2004. A novel generic platform for chemical patterning of surfaces. *Progress in Surface Science* 76(3-5), 55-69.
- Martinoia, S., Bove, M., Tedesco, M., Margesin, B., Grattarola, M., 1999. A simple microfluidic system for patterning populations of neurons on silicon micromachined substrates. *Journal of Neuroscience Methods* 87(1), 35-44.
- Michel, R., Lussi, J., Csucs, G., Reviakine, I., Danuser, G., Ketterer, B., Hubbell, J., Textor, M., Spencer, N., 2002. Selective molecular assembly patterning: A new approach to micro- and nanochemical patterning of surfaces for biological applications. *Langmuir* 18(8), 3281-3287.
- Palik, E. D., 1985. *Handbook of Optical Constants of Solids*. Academic Press.
- Pancrazio, J. J., Whelan, J. P., Borkholder, D. A., Ma, W., Stenger, D. A., 1999. Development and application of cell-based biosensors. *Annals of Biomedical Engineering* 27, 687-711.
- Pasche, S., De Paul, S., Vörös, J., Spencer, N., Textor, M., 2003. Poly(L-lysine)-graft-poly(ethylene glycol) assembled monolayers on niobium oxide surfaces: A quantitative study of the influence of polymer interfacial architecture on resistance to protein adsorption by ToF-SIMS and in situ OWLS. *Langmuir* 19(22), 9216-9225.
- Rohr, S., Fluckiger-Labrada, R., Kucera, J. P., 2003. Photolithographically defined deposition of attachment factors as a versatile method for patterning the growth of different cell types in culture. *European Journal of Physiology* 446(1), 125-132.
- Rohr, S., Scholly, D. M., Kleber, A. G., 1991. Patterned growth of neonatal rat heart cells in culture. Morphological and electrophysiological characterization. *Circ. Res.* 68(1), 114-130.
- Sanjana, N., Fuller, S., 2004. A fast flexible ink-jet printing method for patterning

- dissociated neurons in culture. *Journal of Neuroscience Methods* 136(2), 151-163.
- Scholl, M., Sprossler, C., Denyer, M., Krause, M., Nakajima, K., Maelicke, A., Knoll, W., Offenhausser, A., 2000. Ordered networks of rat hippocampal neurons attached to silicon oxide surfaces. *Journal of Neuroscience Methods* 104(1), 65-75.
- Scofield, J. H., 1976. Hartree-Slater subshell photoionization cross-sections at 1254 and 1487 eV. *Journal of Electron Spectroscopy and Related Phenomena* 8(2), 129-137.
- Sen, A., Dunnmon, P., Henderson, S. A., Gerard, R. D., Chien, K. R., 1988. Terminally differentiated neonatal rat myocardial cells proliferate and maintain specific differentiated functions following expression of SV40 large T antigen. *Journal of Biological Chemistry* 263(35), 19132-19136.
- Sorribas, H., Padeste, C., Tiefenauer, L., 2002. Photolithographic generation of protein micropatterns for neuron culture applications. *Biomaterials* 23(3), 893-900.
- Stenger, D. A., McKenna, T. M. (1994). *Enabling Technologies for Cultured Neural Networks*, Academic Press, London.
- Thomas, S. P., Bircher-Lehmann, L., Thomas, S. A., Zhuang, J., Saffitz, J. E., and Kleber, A. G., 2000. Synthetic strands of neonatal mouse cardiac myocytes: structural and electrophysiological properties. *Circ. Res.* 87(6), 467-473.
- Thomas, S. P., Kucera, J. P., Bircher-Lehmann, L., Rudy, Y., Saffitz, J. E., Kleber, A. G., 2003. Impulse propagation in synthetic strands of neonatal cardiac myocytes with genetically reduced levels of connexin43. *Circ. Res.* 92, 1209-1216.
- Tosatti, S., Paul, S. M. D., Askendal, A., VandeVondele, S., Hubbell, J. A., Tengvall, P., Textor, M., 2003. Peptide functionalized poly(-lysine)-g-poly(ethylene glycol) on titanium: resistance to protein adsorption in full heparinized human blood plasma. *Biomaterials* 24(27), 4949-4958.
- van der Schalie, W. H., Gardner, H. S., Bantle, J. A., de Rosa, C. T., Finch, R. A., Reif, J. S., Reuter, R. H., Backer, L. C., Burger, J., Folmar, L. C., Stokes, W. S., 1999. Animals as sentinels of human health hazards of environmental chemicals. *Environmental Health Perspectives* 107(4), 309-315.
- White, S. M., Constantin, P. E., Claycomb, W. C., 2004. Cardiac physiology at the cellular level: use of cultured HL-1 cardiomyocytes for studies of cardiac muscle cell structure and function. *American Journal of Physiology, Heart Circulation Physiology* 286(3), H823-829.
- Whitesides, G. M., Ostuni, E., Shuichi, T., Jiang, X., and Ingber, D. E., 2001. Soft lithography in biology and biochemistry. *Annual Reviews Biomedical Engineering* 2001 3, 335-373.
- Wyart, C., Ybert, C., Bourdieu, L., Herr, C., Prinz, C., Chatenay, D., 2002. Constrained synaptic connectivity in functional mammalian neuronal networks grown on patterned surfaces. *Journal of Neuroscience Methods* 117(2), 123-131.

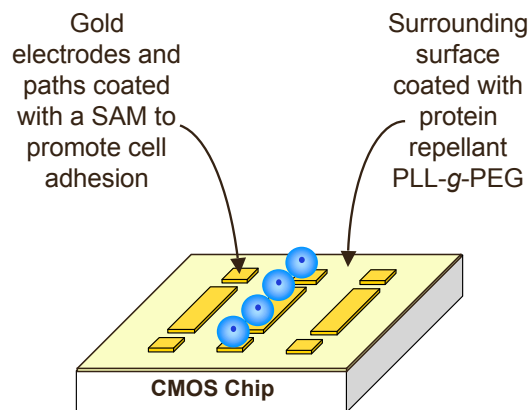


Fig 1: Gold electrodes and paths are used to define regions of cell adhesion on the CMOS cell-based biosensor.

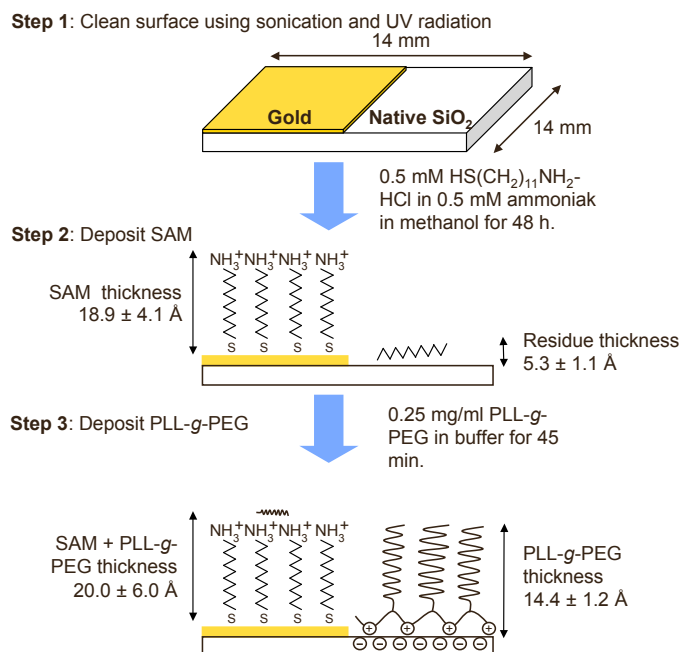


Fig 2: Schematic of surface preparation including process parameters and organic layer thickness as determined by scanning ellipsometry.

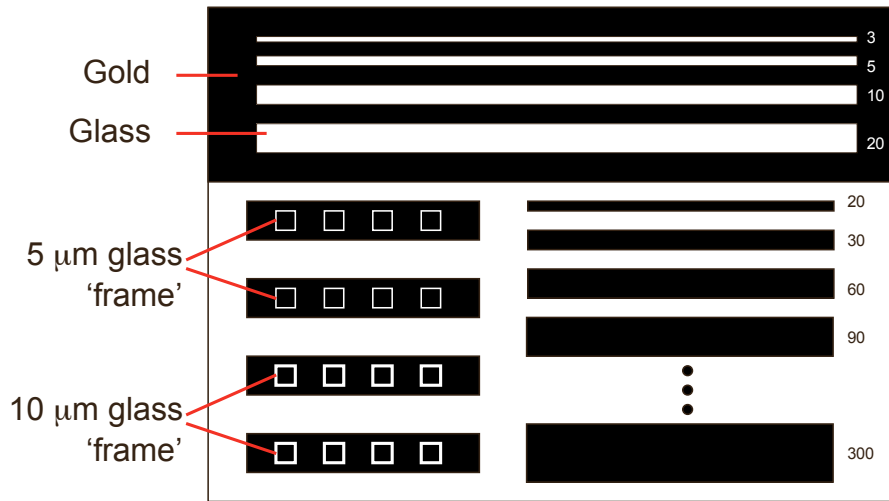


Fig 3: Schematic of design 2 test chip showing gold lines (black) of increasing width (20, 30, 60, 90, ... 300 μm) and a gold region with SiO<sub>2</sub> gaps (white) of increasing width (3, 5, 10, 20 μm). Also included are gold lines with electrically isolated square electrodes demarcated by 5 and 10 μm thick SiO<sub>2</sub> frames. The purpose of these structures is to determine: the minimum features that can be achieved using our in-house lift-off process, the minimum line width in which cells form a continuous strand and the width of SiO<sub>2</sub> lines that the cells overgrow.

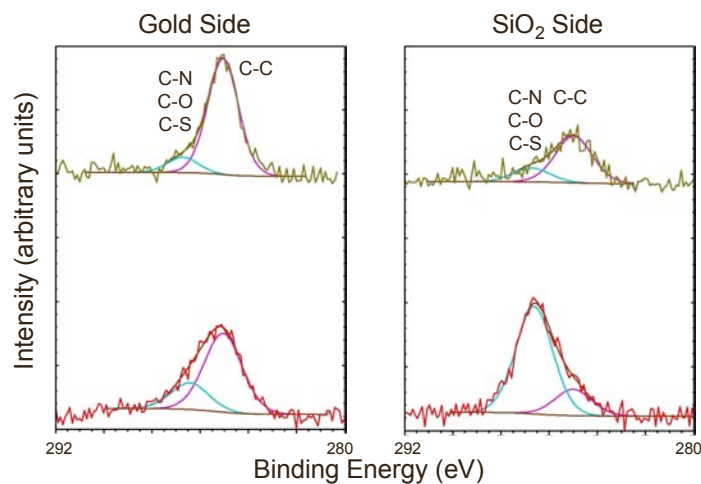


Fig 4: X-ray photoelectron C1s spectra after SAM deposition (top scan) and PLL-g-PEG deposition (bottom scan). The measured spectra are the noisy lines, while the modeled results are the smooth lines.

Element	Assignment	Atomic %		
		SAM only	After SAM	After PLL-g-PEG
<b>Gold Side</b>				
C(1s)	<u>C</u> H <sub>2</sub> , <u>C</u> H <sub>3</sub> , Contamination (*1) <u>C</u> -N, <u>C</u> -S, <u>C</u> -O (*2)	46.3	46.5	47.2
O(1s)	<u>C</u> - <u>O</u> , <u>C</u> - <u>O</u> OH Contamination	3.4	9.9	8.7
Au(3d)	<u>Au</u>	47.5	41.4	41.6
N(1s)	<u>C</u> - <u>N</u> H <sub>2</sub>	1.7	1.2	1.2
S(2p)	<u>C</u> - <u>S</u>	1.1	1.3	1.3
<b>SiO<sub>2</sub> Side</b>				
<b>PLL-g-PEG only</b>				
C(1s)	<u>C</u> -C Contamination <u>C</u> -N, <u>C</u> -S, <u>C</u> -O	18.6	6.7	17.6
O(1s)	<u>SiO</u> <sub>2</sub> <u>C</u> - <u>O</u>	27.4	45.0	37.4
Si(sp)	<u>SiO</u> <sub>2</sub>	54.0	48.3	45.0

(\*1) C-C Binding energy: 285.0 eV  
(\*2) C-X Binding energy: 286.5 – 286.8 eV

Table 1: XPS elemental compositions as calculated using the sensitivity factors from Scofield.

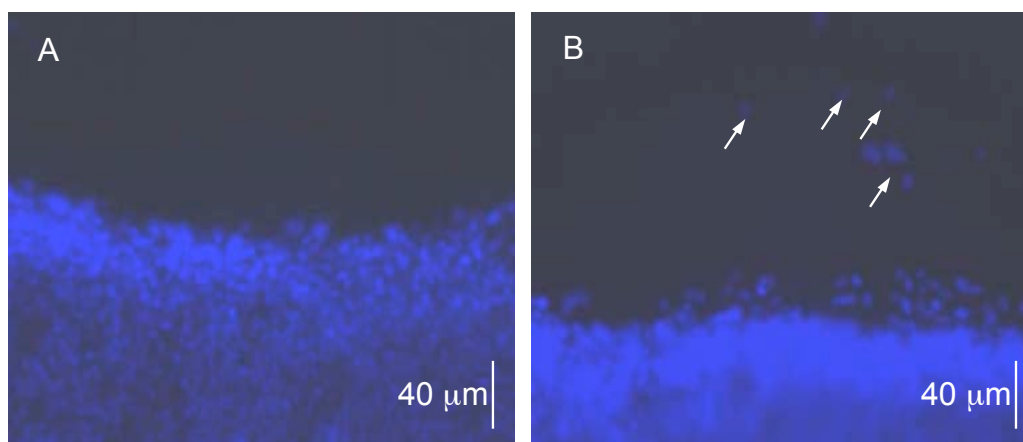


Fig 5: HL-1 cardiomyocytes with DAPI-stained nuclei growing only on the gold side of Design 1 chip. In image B some islands of cells, or cell debris, adhere to the PLL-g-PEG, as indicated by white arrows. These islands of cells are not expected to influence biosensing measurements since they are few and isolated. Images taken at 7 days in vitro.

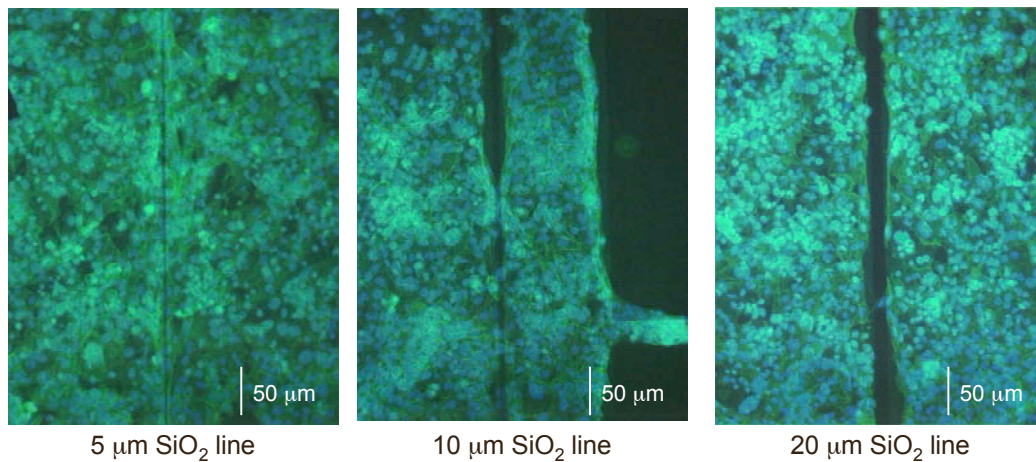


Fig 6: HL-1 cardiomyocytes growing on Design 2 chip at 2 DIV. The nucleus has been stained with DAPI and the actin fibers with Phalloidin. The cells bridge over 5 and 10  $\mu\text{m}$  lines of SiO<sub>2</sub> coated with PLL-g-PEG, but do not bridge a 20  $\mu\text{m}$  SiO<sub>2</sub> line.

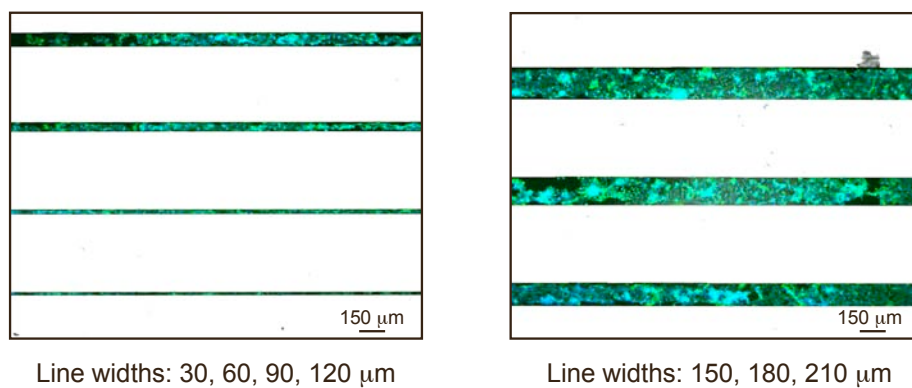


Fig 7: Neonatal rat cardiomyocytes at 4 DIV growing on gold lines with widths of 30, 60, 90, 120, 150, 180 and 210  $\mu\text{m}$ . The nucleus has been stained with DAPI and the actin fibers with Phalloidin. The cells form a continuous strand at a gold line width of at least 60  $\mu\text{m}$ . With few exceptions, the cells are confined to the SAM-functionalized gold surface.



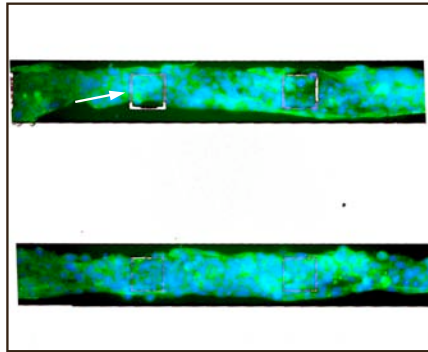


Fig 8: HL-1 cardiomyocytes at 2 DIV growing on structured gold with a line width of 100  $\mu\text{m}$  and a 5 and 10  $\mu\text{m}$  wide  $\text{SiO}_2$  frame between electrode and surrounding gold line (see arrow). The nucleus has been stained with DAPI and the actin fibers with Phalloidin. The cells form a continuous strand and overgrow the frames of PLL-*g*-PEG-functionalized  $\text{SiO}_2$ .

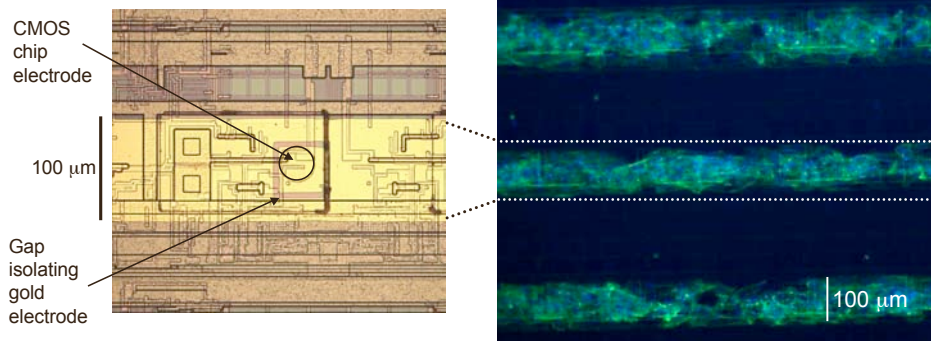


Fig 9: Fluorescence microscopy image (right) of neonatal rat cardiomyocytes at 4 DIV growing on structured gold with a line width of 100  $\mu\text{m}$  that had been deposited on the CMOS chip. The gold electrode patches have been aligned to the underlying electrodes of the CMOS chip (left). The nucleus has been stained with DAPI and the actin fibers with Phalloidin. The cells form a continuous strand and overgrow the regions of PLL-*g*-PEG-functionalized  $\text{SiO}_2$ .

---

# APPENDIX D

## HIPPOCAMPAL NEURON PREPARATION AND CULTURE PROTOCOL

Below is the preparation and culture protocol for the hippocampal neurons developed by Elisabetta Ruaro at the Scuola Superiore di Studi Avanzati (SISSA), Trieste, Italy [Ruaro et al., 2005]. All reagents are from Sigma-Aldrich Co., U.S.A., unless otherwise specified.

### D.1 Preparation

The hippocampus from three-day-old Wistar rats was dissected in ice-cold dissection medium. Slices were cut with a razor blade, transferred into a 15-ml centrifuge tube and washed twice with the dissection medium (see below). Slices were then treated with 5 mg/ml trypsin (Invitrogen Corp., U.S.A.) and 0.75 mg/ml DNaseI in digestion medium for 5 min. at room temperature to perform enzymatic dissociation. Trypsin was then neutralized by 1 mg/ml trypsin inhibitor in dissection medium for 15 min. on ice. After three washes with the dissection medium, mechanical dissociation was performed by 10 passages through a P1000 blue tip. The cell suspension was then centrifuged at 100 g for 5 min., and the pellet was re-suspended in culture medium.

### D.2 Medium Components

**Dissection Medium:** Hanks' modified  $\text{Ca}^{2+}/\text{Mg}^{2+}$ -free solution supplemented with 4.2 mM  $\text{NaHCO}_3$ , 12 mM HEPES, 33 mM D-glucose, 200 mM kynurenic acid, 25 mM DL-2-amino-5-phosphonovaleric acid (APV), 5 mg/ml gentamycin, 0.3 % BSA.

**Digestion Medium:** 137mM NaCl, 5mM KCl, 7mM  $\text{Na}_2\text{HPO}_4$ , 25mM HEPES, 4.2mM  $\text{NaHCO}_3$ , 200mM kynurenic acid, 25mM APV.

**Culture Medium:** Minimal Essential Medium with Earle's salts (Invitrogen) supplemented with 5 % fetal calf serum, 0.5% D-glucose, 14 mM HEPES, 0.1 mg/

---

ml apo-transferrin, 30 mg/ml insulin, 0.1 mg/ml d-biotin, 1 mM vitamin B12 and 2 mg/ml gentamycin.

### **D.3 Cell Plating**

The chip surface was plated with  $\sim 8 \times 10^5$  cells/cm<sup>2</sup>. Cells were allowed to settle on the surface of the chip at room temperature for 20 min., then culture medium was added and the culture dish was incubated. After 48 hours, 5 mM cytosine-b-D-arabinofuranoside (Ara-C) was added to the culture medium, in order to block glial cell proliferation, and the culture dish was re-incubated with gentle rocking.

### **D.4 Maintenance**

Neuronal cultures were kept in an incubator set to 5 % CO<sub>2</sub>, 37 °C and 95 % relative humidity. Half the medium was replaced bi-weekly.

### **D.5 References**

Ruaro, M. E., Bonifazi, P., Torre, V. (2005). "Towards the neurocomputer: image processing and pattern recognition with neuronal cultures." IEEE Transactions on Biomedical Engineering.

---

# APPENDIX E

## STAINING PROTOCOL

Below is the staining protocol used to visualize the sarcomeric structures of the neonatal rat cardiomyocytes.

1. Remove culture medium and rinse 3 x 5 min. with PBS.
2. Fix cells with 4% PFA in PBS for 10 min. at room temperature.
3. Replace PFA/PBS with 0.1 M Glycin in PBS.
4. Permeabilize membrane with 0.2% Triton X-100 in PBS for 10 min.
5. Attach first antibody: cardiac myosin-binding protein C using a polyclonal rabbit antibody (polyclonal rabbit, pR anti MyBP-C, COC1, courtesy of M. Gautel)
  - i 1:100 in 1 mg/ml BSA/PBS
  - ii Overnight at 4 °C or 60 min. at room temperature
  - iii Rinse 3 x 5 min. with PBS.
6. Attach 2<sup>nd</sup> antibody:
  - i Goat-anti-rabbit (GaR) IgG cy3, 1:500
  - ii Phalloidin: 1: 40
  - iii DAPI: 1:1000
7. Rinse 3 x 5 min. with PBS.
8. Cover sample with Lisbeths Medium (50% glycerol in PBS plus 1 mg/ml n-propyl gallate)
9. Perform microscopy

To stain the  $\alpha$ -actinin protein, the first antibody was Sigma Clone EA53 (1:500) and the 2<sup>nd</sup> antibody was goat-anti-mouse (GaM) IgG cy3 (1:500).

---

---

# PUBLICATION LIST

Franks, W., Heer, F., McKay, I., Taschini S., Sunier, R., Hagleitner, C., Hierlemann, A., Baltes, H. "CMOS monolithic microelectrode array for stimulation and recording of natural neural networks." *Transducers '03*, Boston, 963-966.

Prandtl, D., Franks, W., Mondon, M., Blau, A., Ziegler, C. "SFM - A versatile tool for characterizing electrodes and coatings on microelectrode arrays (MEA)." *Proceedings of Scanning Probe Microscopies and Organic Materials 2003*, Mainz, Germany.

Heer, F., Franks, W., McKay, I., Taschini S., Hierlemann, A., Baltes, H. "CMOS microelectrode array for extracellular stimulation and recording of electrogenic cells." *Proceedings of ISCAS '04*, Vancouver.

Heer, F., Franks, W., Blau, A., Taschini, S., Ziegler, C., Hierlemann, A., and Baltes, H. (2004). "CMOS microelectrode array for the monitoring of electrogenic cells." *Biosensors and Bioelectronics*, 20(2), 358-366.

Franks, W., Tosatti, S., Heer, F., Hierlemann, A., Textor, M., Baltes, H. "Biomimetic self-assembled surfaces for highly selective guided cell growth on cell-based biosensors." *Proceedings of The Eighth World Conference on Biosensors 2004*, Granada, Spain.

Franks, W., Schenker, I., Schmutz, P., Hierlemann, A. (2005). "Impedance Characterization and Modeling of Electrodes for Biomedical Applications." *Transactions on Biomedical Engineering* (in print).

Franks, W., Heer, F., Hafizovic, S., Seif, P., Textor, M., Hierlemann, A. "CMOS Biosensor with Guided Cell Growth." *Proceedings of IEEE Sensors 2004*, Vienna, Austria.

Franks, W., Tosatti, S., Heer, F., Seif, P., Textor, M., Hierlemann, A. (2005). "Self-Assembled Structures for Patterned Cell Adhesion on a CMOS Cell-based Biosensor." *Biosensors & Bioelectronics* (in preparation).

Kraus, T., Verpoorte, E., Linder, V., Franks, W., Hierlemann, A., Fujii, T., de Rooij, N., Koster, S. (2005). "Microfluidic dispensing system for localized stimulation of cellular networks." *Lab on a Chip* (submitted).

---

# CURRICULUM VITAE

Date of Birth: September 4, 1974

Nationality: Canadian

Address: Dufourstrasse, 91, 8008, Zurich

## EDUCATION

2000 – present	Doctoral work in the field of biosensor devices Department of Physics, ETH Zurich
2003 - 2004	Entrepreneur Course, Create Switzerland, ETH Zurich
1998 – 2000	Master of Applied Science, electrical engineering University of Waterloo, Canada and DALSA Corp.
1993 – 1998	Bachelor of Applied Science, chemical engineering University of Waterloo, Canada

## PROFESSIONAL EXPERIENCE

Business experience	<p>Co-developed of a business plan to commercialize a new ion-channel assay technology; performed market research and presented the concept to the head of external affairs and the global head of functional validation at Novartis, thereby establishing an informal relationship with Novartis to further develop the technology.</p> <p>Co-founder of Zurich Start-up Platform, a spin-off from Create Switzerland intended to bring entrepreneurial skills to the local technical community</p>
Doctoral thesis	<p>Developed a cell-based biosensor for drug verification and neuroscience applications. Cell-based biosensor consists of a CMOS chip which can stimulate and record activity of electrically active cells (heart muscle cell, neurons). Supervised three Master's level students. Participated in Venture 2004 business competition (sponsored by McKinsey and ETH).</p> <p><b>Areas of expertise:</b> surface science, silicon chip fabrication, cell culturing</p>
Master's Thesis	<p>Development of an inorganic phosphor coating for digital image sensors in deep UV applications. Master's research was performed at and for DALSA Inc., designers and manufacturers of digital image sensors, Waterloo, Canada.</p>

## LANGUAGES

German	Con conversationally fluent
--------	-----------------------------



---